Design of Novel Titanium Dioxide-Based Multifunctional Electrochemical Cells

by

Gregory Lui

A thesis

presented to the University of Waterloo

in fulfillment of the

thesis requirement for the degree of

Doctor of Philosophy

in

Chemical Engineering (Nanotechnology)

Waterloo, Ontario, Canada, 2018

Examining Committee Membership

The following served on the Examining Committee for this thesis. The decision of the Examining Committee is by majority vote.

External Examiner	**NAME:** Paul Charpentier **Title:** Professor Department of Chemical and Biochemical Engineering
Supervisor(s)	**NAME:** Aiping Yu **Title:** Associate Professor Department of Chemical Engineering, University of Waterloo **NAME:** Michael Fowler **Title:** Professor Department of Chemical Engineering, University of Waterloo
Internal Member(s)	**NAME:** William Anderson **Title:** Professor Department of Chemical Engineering, University of Waterloo **NAME:** Michael Pope **Title:** Assistant Professor Department of Chemical Engineering, University of Waterloo
Internal-external Member	**NAME:** Siva Sivoththaman **Title:** Professor Department of Electrical and Computer Engineering, University of Waterloo
Other Member(s)	n/a

Author's Declaration

This thesis consists of material all of which I authored or co-authored: see Statement of Contributions included in the thesis. This is a true copy of the thesis, including any required final revisions, as accepted by my examiners.

I understand that my thesis may be made electronically available to the public.

Statement of Contribution

The body of this thesis is based on a combination of published work. Various sections are adapted from the following list of publications.

Chapter 4

Lui, G.; Li, G.; Wang, X.; Jiang, G.; Lin, E.; Fowler, M.; Yu, A.; Chen, Z., Flexible, three-dimensional ordered macroporous TiO_2 electrode with enhanced electrode–electrolyte interaction in high-power Li-ion batteries. *Nano Energy* **2016,** *24*, 72-77.

- I performed all synthesis experiments with the help of E. Lin.
- G. Li helped with battery fabrication and testing.
- X. Wang and G. Jiang helped analyze the data and review the manuscript.

Chapter 5

Lui, G.; Jiang, G.; Lenos, J.; Lin, E.; Fowler, M.; Yu, A.; Chen, Z., Advanced Biowaste-Based Flexible Photocatalytic Fuel Cell as a Green Wearable Power Generator. *Advanced Materials Technologies* **2017,** *2* (3).

- I performed all synthesis and characterization experiments with the help of E. Lin.
- G. Jiang helped analyze the data and review the manuscript.
- J. Lenos helped with device testing.

Chapter 6

Lui, G.; Jiang, G.; Fowler, M.; Yu, A.; Chen, Z., A High Performance Waste water-Fed Flow-Photocatalytic Fuel Cell. (submitted to *Journal of Power Sources*).

- I performed all synthesis and characterization experiments.
- G. Jiang provided significant contribution to project direction, helped analyze the data, and reviewed the manuscript.

Abstract

Increasing energy demands as well as the depletion of traditional resources has led to the development and improvement of energy conversion and storage technologies. Today, two major concerns are development of renewable sources of energy and establishing reliable sources of potable water to the meet continually growing demands of our society. One technology that has the potential to address both of these issues is the photocatalyst: a material that is able to use natural light irradiation to drive useful chemical reactions and create electrical power. Photocatalytic materials have already been commercially demonstrated to purify waste water and air pollution under ultraviolet irradiation. However, in a photoelectrochemical cell, photocatalytic applications extended beyond waste water remediation to the production of electricity and alternative fuels such as hydrogen gas.

This thesis aims to explore the potential multifunctionality of TiO_2 materials and point to applications that extend beyond traditional photocatalysis. Specifically, this work covers the study and design of titanium oxide (TiO_2)-based multifunctional electrochemical cells that can simultaneously purify waste water and provide energy in the form of electrical power.

First, this thesis explored potential applications for three-dimensional macroporous (3DOM) TiO_2 morphologies for electrochemical applications. Although the material was a suitable photocatalyst it was found to be an effective freestanding TiO_2 anode on carbon cloth for Li-ion battery applications. The 3DOM TiO_2-based anode provided a flexible, free-standing, binder-free, active material with superior power density when compared to other electrode materials in a similar configuration. This work also provided the first instance of the successful application of 3DOM materials on non-planar surfaces.

Commercial TiO_2 (P25) was also employed as a photoanode in a flexible photocatalytic fuel cell as a proof-of-concept device that generates electrical power from the photo-degradation of waste sources such as human sweat (as a wearable device) and dye waste (as a flexible water treatment device). This work established the potential application of photocatalysis in wearable technologies and in flexible photocatalytic devices in general.

Finally, a burr-like Ag-TiO_2 photocatalyst was developed as a photoanode material in a flow-photocatalytic fuel cell for the continuous power generation and photo-degradation of brewery effluent under solar-simulated light. This work explored the effect of Ag loading on photoelectrochemical performance, and demonstrated unprecedented power density of a flow-photocatalytic fuel cell in a continuous flow configuration.

Acknowledgements

I would like to thank my supervisors, Prof. Aiping Yu and Prof. Michael Fowler, for supporting and guiding me throughout my studies, and giving me the freedom to explore and pursue different scientific interests. I would also like to thank Prof. Zhongwei Chen for providing research guidance and lab space throughout my tenure. I would like to acknowledge Dr. Gaopeng Jiang for all of his collaborative efforts and invaluable advice during my research. I would like to thank everyone at the Applied Carbon Nanotechnology Laboratory and Applied Nanomaterials & Clean Energy Laboratory for making the machine work without oil.

Thank you Stephanie Lu for being my personal assistant, biggest fan, and best friend, and for doing most of the worrying on my behalf. Thank you to my family – Yvonne, Geoff Ryan, Genny, and Kurt – for taking care of me and keeping me relatively sane for the past *n* years. Thank you for everything, Dad.

Soli Deo gloria.

Table of Contents

Table of Figures

Table of Tables

1.0 Introduction

As the world faces growing issues regarding the environment and energy security, the scientific community is looking for cleaner solutions to existing problems. In the face of the depletion of fossil fuel resources, energy production and storage industries are under pressure to provide technologies that are clean and renewable. At the same time, waste remediation and pollution control technologies are in high demand in order to address the increasing requirement for emission treatment and potable water needs of a growing world population. Although Canada is continually working towards lowering its greenhouse gas emissions (GHG), its oil and gas and transportation sectors continue to be one of the largest contributor growing greenhouse gas emissions.[1]

Photocatalysts are a recently discovered class of materials that are a potential solution to many of the energy concerns described above. Fujishima showed in 1972 that photocatalytic materials such as titanium dioxide (TiO_2) could use natural sunlight to split water into oxygen and hydrogen gas.[2] This discovery was significant because the work implied that a completely passive and renewable mechanism could be used to produce energy in the form of hydrogen fuel. Since then, photocatalysts have been used in various applications, including waste water treatment, sterilization, cancer therapy,[3] dye-sensitized solar cells,[4] and hydrocarbon cracking.[5] Two significant applications of photocatalytic materials are in the areas of waste water remediation and energy production. In more recent years, photocatalysts have been used to simultaneously decompose organics in waste water and generate energy in the form of electricity or hydrogen fuel in a photoelectrochemical cell.[6]

The reason TiO_2 is able to act as a photocatalyst is because of it has many desirable optical and electrochemical properties. The photo-redox chemistry of TiO_2 is such that it is highly reactive with many other compounds. At the same time, TiO_2 is very chemically stable, even under light irradiation, making it a strong candidate for photocatalysis. Even with these properties, TiO_2 photocatalysis remains a relatively underdeveloped field with applications that do not extend beyond traditional photocatalysis. There are several reasons for the lack of commercial development for photocatalysis. First, the recombination rate of charge-carriers in conventional TiO_2 particles is high, leading to low efficiencies and low photocatalytic activities. Second, TiO_2 only absorbs light within the ultraviolet (UV) spectrum, limiting it to less than 5% of the solar spectrum.[7] Lastly, certain applications for TiO_2-based photocatalysis have yet to be explored.

Based on the aforementioned reasons, research on improved photocatalytic systems is required and continuing to grow.[8,9] TiO_2 photocatalytic activity can be improved by controlling its morphology, introducing dopants, and heterostructuring TiO_2 with other materials.[10] The morphology of a catalyst can greatly affect its physical and chemical properties, and therefore catalytic performance. Three-dimensional ordered mesoporous (3DOM) structures have the unique property of using its periodic porous structure to manipulate its optical band gap and improve absorbance of light.[11] In addition to this property, 3DOM materials have high porosity with highly accessibly surface sites.[12]

Unfortunately, these optical enhancements only allow a material to more efficiently capture light within its optical band gap and do not actually extend the light absorption spectrum. In order to improve the light absorption and charge separation properties of TiO_2, techniques such as doping and heterostructuring are required. Plasmonic materials have recently been gaining in popularity

as a cocatalyst that can enhance photocatalytic efficiency, and provide photocatalytic activity under visible light irradiation.[13] Plasmonic materials consist of noble metals which perform two functions: 1) form Schottky junctions with semiconductor photocatalysts to encourage charge separation; and 2) create active charge carriers under visible light via a phenomenon called localized surface plasmonic resonance (LSPR). These properties allow plasmonic materials to act as sensitizers for photocatalysts while leaving the large redox potential of the photocatalyst unaffected.

This thesis discusses the design and application of TiO_2-based electrochemical cells in the application of multifunctional photoelectrochemical devices that can generate electrical power from the photo-degradation of organic compounds from various water sources. First, an alternative application for three-dimensional macroporous TiO_2 is found in Li-ion batteries. Then, both commercial and novel TiO_2 materials are implemented into photocatalytic fuel cell devices that have applications in power generation in wearable technologies and waste water treatment.

1.1 Objectives

The objective of this work is to: (i) explore different multifunctional electrochemical systems using TiO_2-based photocatalysis; and (ii) design and optimize TiO_2-based photocatalysts for sunlight-activated waste water remediation as well as a means of creating meaningful and scalable energy output. This two-fold objective can be broken down into the following steps:

1) Test the photocatalytic performance of 3DOM TiO_2 and demonstrate the transferability of nanomaterials to an energy storage context.

a. Demonstrate an electrochemical application of 3DOM materials on non-planar surfaces.

b. Evaluate the electrochemical performance of 3DOM TiO_2 as a free-standing, flexible, binder free anode material in Li-ion batteries.

2) Design and fabricate a TiO_2-based photocatalytic fuel cell as a proof-of-concept device using commercial TiO_2 (P25).

a. Evaluate device power output as a methanol-based photocatalytic fuel cell, and under bending conditions.

b. Evaluate device power output using human sweat and textile dye as a form of simultaneous waste removal and current generation.

3) Design and fabricate a burr-like Ag-TiO_2 photocatalyst as a photoanode in a flow-photocatalytic fuel cell.

a. Evaluate device power output in a methanol-based photocatalytic fuel cell.

b. Determine the optical and electronic properties of the Ag-TiO_2 photocatalyst that improve the performance of the photocatalytic fuel cell.

c. Evaluate device power output using brewery effluent in a flow configuration.

1.2 Thesis Organization

This work is organized in the following manner:

Chapter 1 is an introduction to the work and its motivations and objectives.

Chapter 2 provides a brief overview of the operating principles of photocatalysts, highlighting the properties of a strong photocatalytic material. TiO_2 is then presented as the photocatalytic

material of interest. The synthesis and use of TiO_2 in literature as a photocatalyst and photoanode in photocatalytic fuel cells is discusses in greater detail. A short discussion is also given on the application of TiO_2 in applications such as photocatalytic fuel cell systems for photocatalysis and energy production, and Li-ion batteries.

Chapter 3 provides a brief explanation of the characterization and experimental techniques used in this work.

Chapter 4 presents work done on 3DOM TiO_2 as a photocatalytic material and ultimate application into Li-ion batteries as a high power anode material.

Chapter 5 presents work done on implementing commercial TiO_2 (P25) into a flexible photocatalytic fuel cell that produces electrical power from the photo-degradation of human sweat and textile dye.

Chapter 6 presents work done on synthesizing a burr-like Ag-TiO_2 photocatalytic material that has improve visible-light activity and produces electrical power from the photo-degradation of brewery effluent in a continuous flow configuration.

Chapter 7 outlines the main conclusions, contributions, recommendations, and future work based on this thesis.

2.0 Literature Review

2.1 Semiconductor Theory

Photocatalysis involves the acceleration of a chemical reaction via a light-activated catalyst. Photocatalysts use photo-generated electron-hole pairs to generate free radical species that can undergo useful secondary reactions. Because of the nature of photo-generation, photocatalysts are based on semiconductor materials.

Semiconductors are materials that have an energy band gap (E_g) between its valence band and conduction band.[14] Semiconductors therefore require energy input equal to or greater than this band gap in order to produce a current and are otherwise non-conducting. When adequate energy is added to the system, an electron is excited from the valence band to the conduction band leaving behind a 'hole', an imaginary particle that holds a positive charge. Therefore, the movement or transition of an electron in one direction is also considered the movement or transition of a hole in the opposite direction. This excitation process is known as electron-hole pair (EHP) generation.

If the EHP is unable to separate from each other after photo-generation, it is possible that the electron can relax back down to the valence band and recombine with the hole in a process aptly called recombination. Recombination can result in the emission of photons and/or phonons, and is undesirable in photocatalysis because the process relies on the energy gained from electron excitation.

The amount of electrons or holes in a semiconductor is described by the Fermi level, E_F, where E_g is the band gap, k is the Boltzmann constant, T is the temperature, and m_p^* and m_n^* are the

effective mass of holes and electrons, respectively (Equation 1-1). The Fermi level is defined as the energy level at which there is a 50% probability of being occupied by an electron. For intrinsic semiconductor materials, Fermi levels are found within the band gap. If additional electrons are added to the system, the Fermi level will increase as more energy levels are occupied with electrons. In the same way, if additional holes are added to the system (i.e. more electrons are removed), the Fermi level will decrease. This type of electronic modification is typically done by a process called doping.

$$E_F = \frac{1}{2}E_g + \frac{3}{4}kTln\left(\frac{m_p^*}{m_n^*}\right) \quad (1\text{-}1)$$

2.1.1 Doping

Doping is the intentional introduction of impurities into a semiconductor material in order to add more electrons or holes to a system. If the impurity atom replacing the original atom has more electrons in its valence shell, the semiconductor as a whole will contain more electrons. These impurities will in turn create donor sites near the conduction band, making the material an n-type semiconductor. If the impurity atom has less electrons than the original atom, the semiconductor will contain more holes, and these impurities will create acceptor sites near the valence band (forming a p-type semiconductor). In both cases, doping has the ability to increase the conductivity of a semiconductor by adding more charge carriers, and decrease its band gap by introducing additional donor or acceptor energy levels within the band gap. The Fermi level changes due to doping are given by Equations 1-2 and 1-3, where n_i is the intrinsic carrier concentration, and N_D and N_A are donor and acceptor atom concentrations, respectively.

Silicon is a commonly used semiconductor that can be either n-doped or p-doped. As a group IV element, Si atoms can be either replaced by group V atoms (such as P, As, Sb) or group III atoms (such as B, Ga, In) in order to introduce excess electrons and holes, respectively. Using a relevant example, TiO_2 is naturally an n-type semiconductor due to oxygen vacancies in its lattice created during synthesis.

$$E_{Fn} = E_F + kTln\left(\frac{N_D}{n_i}\right) \quad (1\text{-}2)$$

$$E_{Fn} = E_F - kTln\left(\frac{N_A}{n_i}\right) \quad (1\text{-}3)$$

2.1.2 Semiconductors in Heterogeneous Systems

When a semiconductor is placed in a heterogeneous system with two or more materials, its energy bands do not necessarily remain constant. If there exists a difference in Fermi level between the semiconductor and the secondary material, then electron exchange will occur until an equilibrium Fermi level is achieved.[15] For example, when TiO_2 is immersed in water, there is a net electron transfer from Ti^{4+} to adsorbed –OH groups. (This is only possible if the Fermi level of the semiconductor is higher than that of the lowest unoccupied molecule orbital (LUMO) of the adsorbed molecule.) This hydroxylation process is driven thermodynamically by the desire for the Fermi level of semiconductor to be in equilibrium with the LUMO of the adsorbed molecule. For this reason, the Fermi level is often referred to as an electrochemical potential. Once the electron transfer takes place, a Helmholtz double layer forms at the interface, causing electron repulsion near the surface of the semiconductor. The region near the semiconductor therefore undergoes band bending and is called the space charge layer.

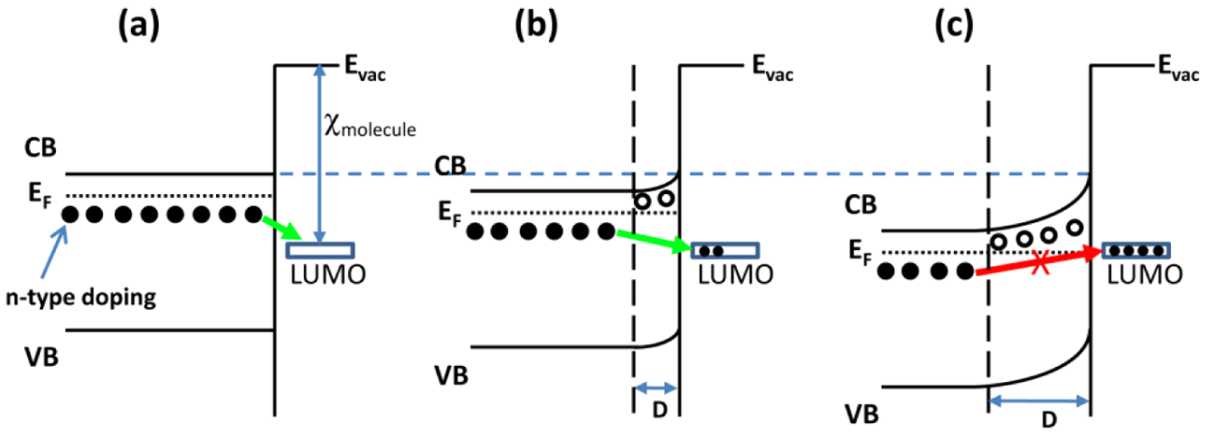

Figure 1-1. Illustration of the basic photocatalytic mechanism.[16]

Band bending behavior is an important phenomenon because it governs how charge transport occurs when semiconductors interact with other media. Band bending is responsible for separating EHPs, indicating the preferred flow of charge carriers, and determining plausible surface redox reactions.

For example, if TiO_2 is heterostructured with Si and placed in electrolyte solution (**Figure 1-2**), then the band bending in both semiconductors is affected by how Si is doped (assuming TiO_2 is naturally n-type). If a composite is made with n-Si, then electrons naturally transfer into the bulk material while holes accumulate at the TiO_2 surface. This encourages charge separation, increases the overall generated (anodic) current, and promotes oxidation at the TiO_2-electrolyte interface. If a composite is made with p-Si, then electrons can easily be trapped within bulk TiO_2 while holes can move toward bulk p-Si or the TiO_2 surface. This reduces the overall (anodic) current, while accumulating electron charge within the TiO_2 bulk instead of the surface (where a reduction reaction could take place).

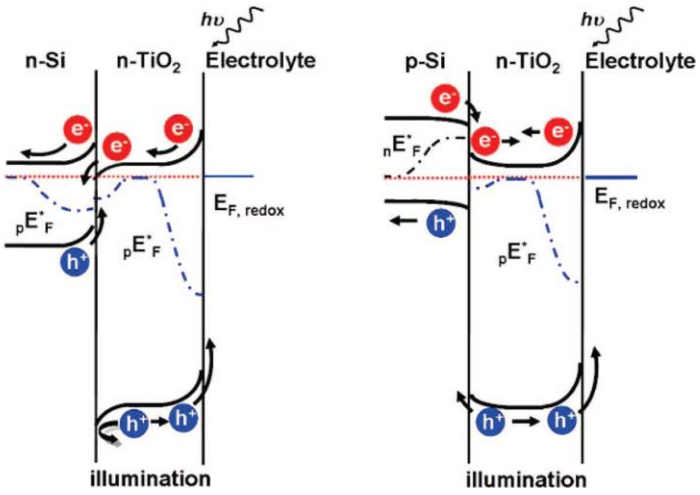

Figure 1-2. Band diagram of Si-TiO_2 depending on the doping of Si.[17]

2.2 Titanium Dioxide (TiO_2) as a Photocatalytic Material

TiO_2 is a naturally occurring metal oxide that is typically found in the form of ilmenite ore. TiO_2 exists in three main mineral forms: anatase, rutile, and brookite. Both anatase and brookite are metastable states, and convert to rutile upon heating.[18] The photocatalytic activity of TiO_2 was first discovered by Fujishima in 1967 and published by Fujishima and Honda in 1972.[2] It was found that TiO_2 could use light irradiation to perform hydrolysis (the breaking of water molecules into hydrogen and oxygen gas).

Since the discovery of this effect, called the Honda-Fujishima effect, TiO_2 has been used as a photocatalytic material in applications ranging from dye-sensitized solar cells[19] to antibacterial systems[20] to air pollution control.[21] Even today, TiO_2 has remained at the forefront of photocatalytic research because of its low cost, chemical stability, and large redox potential.[22,23]

Subsequent work revealed that TiO_2 could be modified in many different ways in order to improve its photocatalytic activity.[24] In addition to changing its mineral phase, impurities could be introduced to modify its absorption spectrum; the morphology of the material could be changed to improve surface area and conductivity; and, TiO_2 could be heterostructured with other co-catalysts to improve overall performance.

The following sections will focus on: 1) the properties of TiO_2 that make it a strong photocatalytic material; ii) the various methods for synthesizing TiO_2; and, iii) the synthesis of specific TiO_2 morphologies and composites for high performing catalysts.

2.2.1 TiO_2 Properties

The properties of TiO_2 relevant to photocatalysis have been widely studied.[25] The most photoactive active form of TiO_2 is thought to be anatase due to its higher adsorption of organic compounds and high hole trapping rate.[26,27] The rutile and brookite phases have also been shown to be photoactive.[28] In fact, TiO_2 containing multiple phases have been shown to improve photocatalytic activity and reduce recombination of charge-carriers.[29,30] Because anatase and rutile TiO_2 are the most relevant and widely studied phases, this section will focus on these phases only.

The most thermally stable crystal face of anatase is (101).[25] The (101) anatase surface is corrugated and consists of alternating rows of 5-coordinated Ti atoms. The lowest energy crystal face of rutile is (110), which consists of 6-coordinated Ti atoms with bridging oxygens. Both anatase and rutile have tetragonal crystal structures, and the transformation of anatase into rutile is possible by annealing anatase at temperatures greater than 400°C.[31]

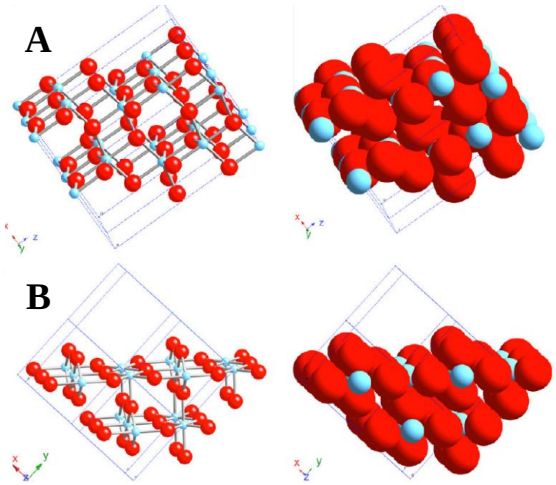

Figure 1-3. The most thermodynamically stable crystal faces of anatase TiO_2(a) and rutile TiO_2 (b). Red spheres = O; blue spheres = Ti.[25]

TiO_2 is an intrinsic wide band gap semiconductor, with optical absorption gaps of 3.2 eV and 3.0 eV for anatase and rutile, respectively.[32] However, anatase and rutile can also be considered n-type semiconductors due to the natural oxygen vacancies within the lattice which reduces Ti^{4+} to Ti^{3+}.[25] These band gaps effectively place the absorption spectrum of pure TiO_2 within the ultraviolet range ($\lambda \approx 10 - 400$ nm).

Mixed-phase TiO_2 containing anatase and rutile consists of a 0.4 eV band alignment, with anatase having a work function 0.2 eV larger than that of rutile (**Figure 1-4**).[29] This confirmation provides a strong theoretical basis for the use of mixed-phase TiO_2 to effectively separate EHPs, reducing charge recombination and increasing photocatalytic efficiency. TiO_2 can have a wide range of conductivities depending on its crystal structure and morphology. As a nanoporous film, TiO_2 has been shown to have conductivities as high as $3.7 \times 10^{-3}\ \Omega^{-1}\cdot cm^{-1}$.[33]

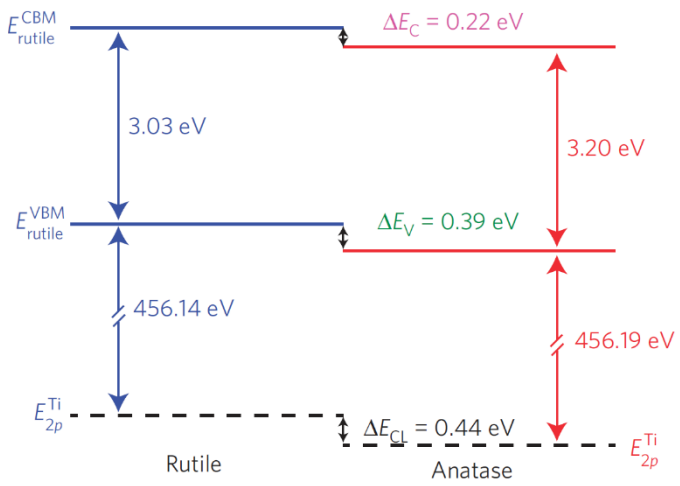

Figure 1-4. Band gap mismatch between anatase and rutile in mixed-phase TiO_2.[29]

At neutral pH, the conduction band of anatase has a potential of approximately -0.5 eV vs. SHE (**Figure 1-5**).[34] The conduction band of anatase is negative enough to reduce O_2 to $O_2^{\bullet -}$ (-0.3 eV vs. SHE). The valence band is also sufficiently positive to oxidize H_2O and other hydroxide species to form their respective radicals. When placed relative to the redox potential of organic functional groups such as aromatics, phenols, amines, and sulfur bands, TiO_2 is very capable of inducing redox reactions.

Apart from photocatalytic applications, TiO_2 is used extensively as a pigment in paints and coatings, as a UV-blocker in sunscreens, and as a food additive.[35] TiO_2 is useful as a white pigment due to its high refractive index and, therefore, high brightness.[36] Its high refractive index means that light is easily bent and redirected off of the surface, even for very thin layers of TiO_2. With the addition of strong UV absorption, this also makes TiO_2 a useful additive in sunscreens. In foodstuffs, TiO_2 is commonly used as both a whitening agent and as an anti-bacterial additive for increasing product shelf-life.

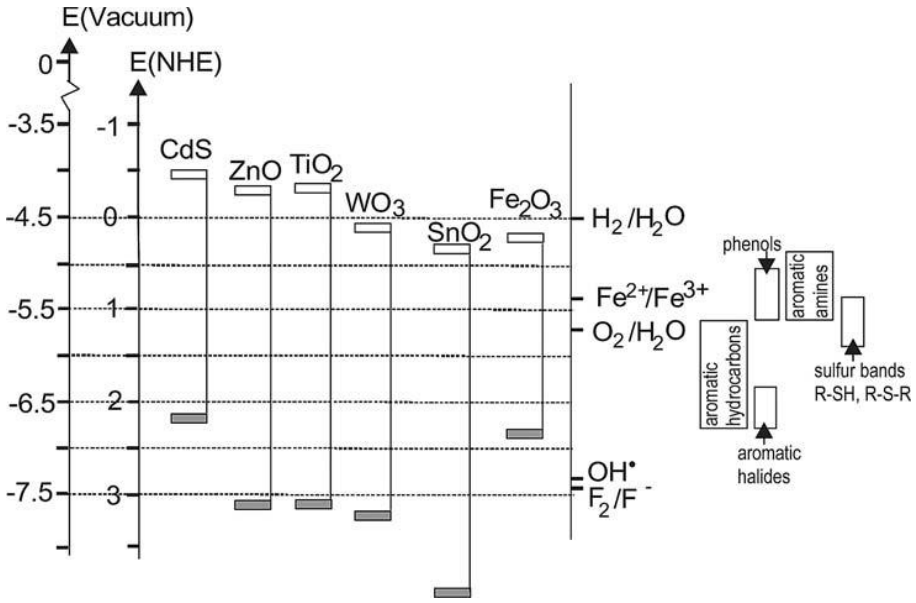

Figure 1-5. Band positions of various semiconductors including TiO_2.Relative redox potentials of various organic functional groups.[24]

Unfortunately, the toxicity of nanoscale TiO_2 particles used in these applications have yet to be thoroughly studied. Although bulk TiO_2 is found to be inert and relatively non-toxic towards humans, existing toxicity studies performed on sub-micron TiO_2 particles has led the International Agency for Research on Cancer to label TiO_2 as an IARC Group 2B carcinogen, meaning that it is *possibly carcinogenic* to humans.[35] This evaluation is based on several studies. One of the largest epidemiological cohort studies performed in TiO_2 production industries in six European countries, as well as three other studies in the USA and Canada showed inadequate evidence for TiO_2 carcinogenicity in humans.[35,37] However, ultrafine TiO_2 particles tested in rats, mice, and hamsters have shown sufficient evidence in animals for its carcinogenicity. For these reasons, TiO_2 is currently classified as possibly carcinogenic to human beings.

2.2.2 TiO_2 Synthesis

The synthesis of photocatalytic materials can be divided into three main approaches: morphology control, doping, and heterostructuring.[38] By controlling and fine-tuning the morphology of a photocatalyst, one can control the physical and electronic properties of the material. Doping, as mentioned previously, can be used to introduce intermediate energy states, increase the conductivity of the semiconductor, and lower the effective band gap of the material. Lastly, heterostructuring combines two different materials in order to take advantage the properties of each material and improve charge-carrier separation.

TiO_2 Morphology Control

TiO_2 can be synthesized using a wide array techniques and processes which have been extensively recorded in literature.[24,38,39] These include precipitation, sol-gel, emulsion, solvothermal and hydrothermal, electrochemical, chemical and physical vapour deposition (CVD and PVD), and microwave methods. Precipitation, sol-gel, and emulsion methods are often employed to create TiO_2 nanoparticles that can be used as films, membranes, or powders. These methods rely on the hydrolysis of TiO_2 precursors such as titanium oxysulfates, titanium chlorides and titanium alkoxides. These methods can also be used with templating compounds such as surfactants, block co-polymers, and other ordered structures to produce specific ordered membranes. Solvothermal and hydrothermal methods are high temperature, high pressure processes that use organic or aqueous solvents as media, respectively. These methods often begin with sol-gel solutions, and so use similar precursors. Solvothermal and hydrothermal reactions are favoured when specific complex morphologies are desired. CVD and PVD processes can be

used to produce thin TiO_2 films. Lastly, microwave methods use high-frequency electromagnetic waves to induce hydrolysis of TiO_2 suspensions to form larger ordered structures.

Sol-gel synthesis of TiO_2 is one of the simplest and popular means of growing TiO_2 nanomaterials.[24,40] Sol-gel methods can be used to produce high purity TiO_2, and processing parameters can be modified to change structure, introduce dopants, and form composites.[24] In sol-gel synthesis, TiO_2 is formed through the hydrolysis and condensation of a titanium alkoxide. Titanium salts can also be used, however this requires the removal of the anion after synthesis.

TiO_2 can take various forms depending on the synthesis method,[39] including nanoparticles,[41] nanotubes,[42] nanosheets,[43] nanobelts,[44] nanorods,[45], nanowires,[46] nanowire arrays,[47] and aerogels.[48] Three-dimensional ordered mesoporous (3DOM) structures have been growing in popularity in the research environment due to their relatively high surface areas, high porosity, high periodicity, and tunable optical properties.[11,49,50] The optical properties of 3DOM materials are perhaps the most interesting, and are described by two main effects: photonic stop band reflection and slow photons.

Photonic stop band reflection occurs when the light incident on the 3DOM material is within the same length scale as the periodicity of the porous structure. Bragg diffraction laws forbids these wavelengths from propagating through the periodic structure, and they are instead reflected. The range of wavelengths that are included in the stop band depend on the periodicity and dielectric contrast within the material. Chen et al. performed a study on 3DOM TiO_2 structures synthesized from templates of varying size (**Figure 1-6**).[11] The results understandably showed that increasing the template size led to an increase in the photon stop band.

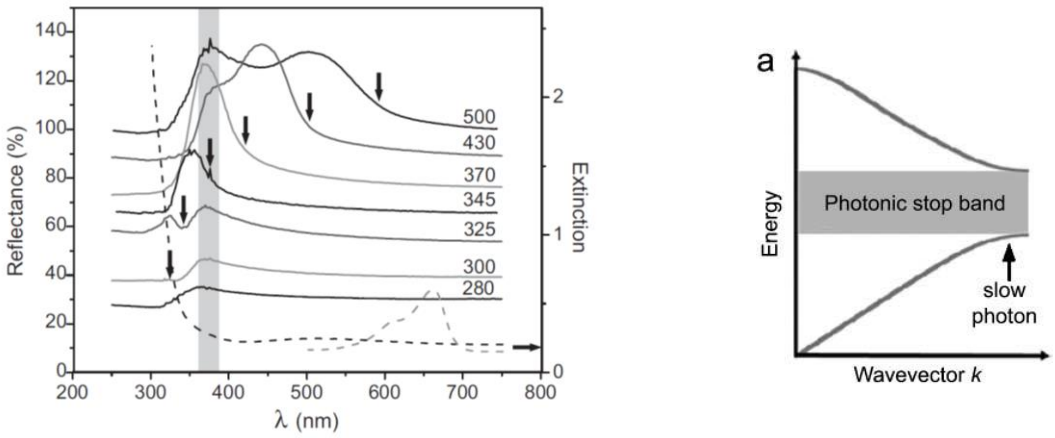

Figure 1-6. Photonic stop bands of 3DOM TiO_2 materials with varying template sizes(Stop band maximums of 280, 300, 325, 345, 370, 430, and 500 nm correspond to template sizes of 130, 150, 180, 210, 240, 300, and 380 nm, respectively (a).[11] E-k diagram for photon group velocity (b).[51]

Research has shown that light with wavelengths near the edges of the photonic stop bands experience a reduction in their group velocity. Much like electron waves in semiconductors (*E-k* diagrams), the group velocity of photons corresponds to $\frac{\delta w}{\delta k}$ and can be reduced to zero near the photonic stop band (**Figure 1-6**b). A slower group velocity increases the effective path length of photons, which can in turn increase the interaction of light with the medium. Therefore, if a 3DOM material can be synthesized that has photonic stop band edges within the same range as the light source being used, the absorption of this light can be enhanced through slow photon effects. For this reason, 3DOM materials have been used in various applications including waveguides,[52] photonic sensors,[53] catalysis,[54,55] and energy storage devices.[56]

3DOM materials are commonly synthesized using a colloidal crystal templating (CCT) method.[12,49] A CCT is prepared and infiltrated with the desired 3DOM material. The template

can then be removed via selective dissolution or calcining in order to form the final 3DOM structure.

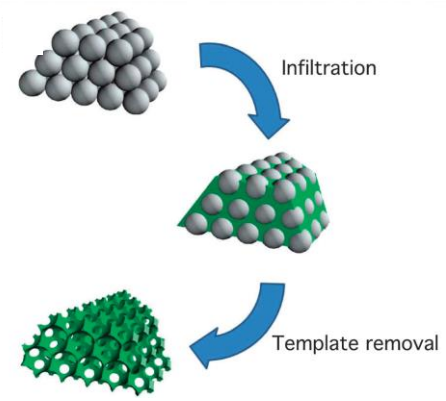

Figure 1-7. Basic process for synthesizing 3DOM structures from a colloidal crystal template.[12]

Various materials have been synthesized in 3DOM form, including metal oxides (TiO_2, SiO_2, ZnO, Fe_2O_3, MnO_2, Nb_2O_5, Ta_2O_5, ZrO_2,),[55,57-60] metals (Pt, W, Ta, Mo),[54,61] and carbon.[62] Some examples of 3DOM metal oxides are shown below in **Figure 1-8**.

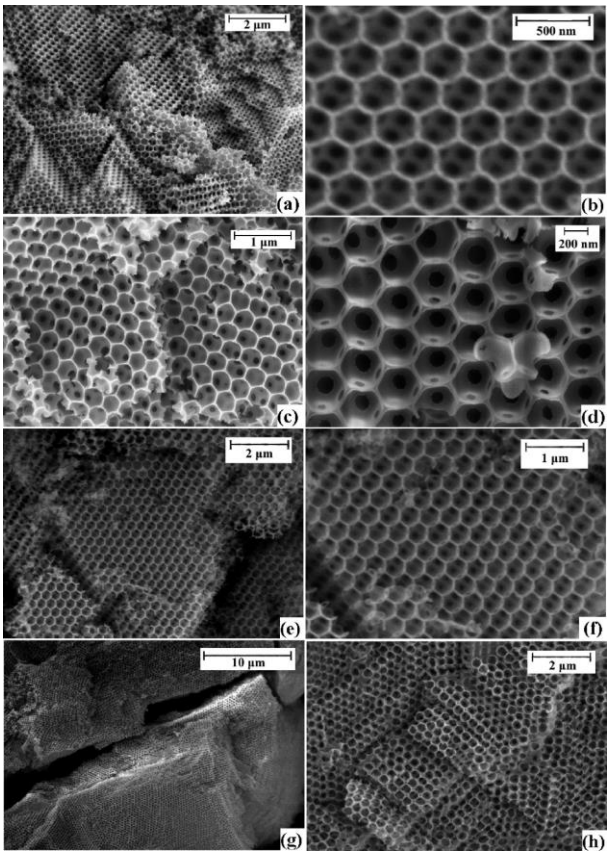

Figure 1-8. SEM images of 3DOM metal oxides: (a, b),TiO_2; (c, d),Nb_2O_5; (e, f), Ta_2O_5; (g, h), ZrO_2.[60]

TiO_2 Doping

TiO_2, and photocatalytic materials in general, can also be doped in order to change the band structure of the semiconductor material. The doping of TiO_2 has been explored extensively by research groups, including both metal ions (Fe, Mo, Ru, Os, Re, V, Rh, Co, Al, Ag, Pd, Pt, Zn, Zr, Cr, Mg, La, Ce, Er, Pr, Gd, Nd, Sm)[63-66] and non-metal ions (C,[67] N,[68] S,[69] F,[70] Cl/Br[30]). Dopants introduce energy bands within the band gap of semiconductors. These energy bands, although very close to either the valence band or conduction band (depending on their contribution to the band structure), causes a shift in the Fermi level and ultimately a reduction in the average band gap of the material. Doping is commonly used with TiO_2 to cause a red shift in

its absorption spectrum and induce visible light photoactivity. In general, *p*-doping is more desirable than *n*-doping, since TiO_2 is intrinsically more oxidative than reductive of water molecular and other organic compounds. This means that the introduction of excess holes, unlike electrons, is more favourable for reducing band gap because their influence over the reduction potential of TiO_2 is less problematic.[10]

TiO_2 Heterostructuring

The final means for improving photocatalytic activity is introducing a second, distinct material that improves absorption of light, acts as a charge-carrier acceptor or donor, or both. The advantage of creating a heterogeneous photocatalyst like this is that the crystal structure and redox characteristics of TiO_2 are preserved, while additional properties can be provided by a secondary material. There are many types of heterogeneous mechanisms, but the most widely studied are charge-carrier transfer, direct and indirect Z-scheme, sensitization, and co-catalyst coupling.[10]

Charge-carrier transfer requires the pairing of TiO_2 with another semiconductor that produces a staggered band-alignment like that shown in **Figure 1-4**. In this configuration, electrons preferentially transfer to one semiconductor, while holes preferentially transfer to the second semiconductor. Examples of semiconductors paired with TiO_2 include CdS,[71] Bi_2O_3,[72] and PbS.[73] Charge-carrier transfer has the advantage of reducing recombination but also the disadvantage of ultimately lowering the redox potential of both charge-carriers.

This disadvantage can be solved by using Z-scheme processes, which separate the two semiconductors and place a mediator in between electrons from one semiconductor and holes from the other. This keeps reduction and oxidation reactions on separate semiconductors, while

maintaining the reaction potential of all charge-carriers. Direct Z-scheme systems include TiO_2-Si,[74] TiO_2-C_3N_4,[75] and TiO_2-Ag-Cu_2O.[76] Indirect Z-scheme systems employ a redox couple in between two separate electrodes to accomplish the same effect. An example of a TiO_2-based indirect Z-scheme is an anatase-rutile TiO_2 system using an IO^{3-}/I^- redox mediator.[77]

Sensitization improves the photocatalytic performance of TiO_2 by providing visible-NIR sensitivity in the form of a narrow band gap secondary material such as an organic dye like N719,[78] or semiconductor such as Cu_2O[79] or CdSe[80]. This heterostructure makes it possible to absorb light within both UV and visible spectrums, while maintaining the large redox potential of TiO_2.

Plasmonic Catalysts

Lastly, co-catalysts can be coupled with TiO_2 to either improve reactivity, improve absorbance, or act as electron acceptors. Both metals (Au, Pt, Ir, Ag, Pd, Ru, Rh)[81-83] and other semiconductors such as NiO and RuO_2[83] have been used as co-catalysts. Carbonaceous nanomaterials are also considered co-catalytic in these systems.[8]

Noble metals such as Ag and Au are especially interesting due to a phenomenon called localized surface plasmon resonance (LSPR). LSPR occurs when the frequency of incident photons matches that of the surface electrons of a metal particle. Although the frequency of incoming light is often predetermined, the resonance wavelength of plasmonic nanoparticles can be tailored based on size, shape, and the surrounding media.

If LSPR occurs, the electrons in the plasmonic particle are excited to a higher energy level, which can allow the transfer of electrons to the conduction band of a neighbouring semiconductor (**Figure 1-9a**). Before full dissipation of this effect (**Figure 1-9c**), electrons in the metal form a

new Fermi-Dirac distribution at a new Fermi level (**Figure 1-9b**) and continue to donate electrons to the semiconductor. If the surface plasmon has an energy larger than the band gap of the semiconductor, it is possible for electron collisions themselves to excite electrons to the conduction band of the semiconductor (**Figure 1-9d**). This is called an LSPR-induced band gap breaking effect.

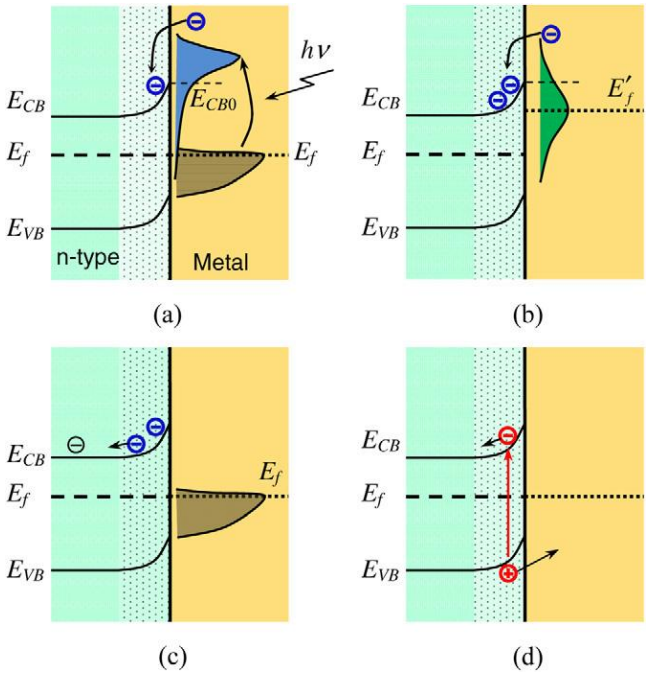

Figure 1-9. Mechanism for LSPR sensitization of a semiconductor.[13]

In addition to LSPR effects, plasmonic materials also create a Schottky junction with the semiconductor. This metal-semiconductor junction can create band-bending phenomenon and a built-in electric field that encourages the separation of generated EHPs. For example, this improved charge separation is possible if the Fermi level of the semiconductor is higher than that of the plasmonic metal such as the configuration found in **Figure 1-9d**. This creates an upward

band bending in the semiconductor, driving electrons into the semiconductor bulk and holes toward the metal bulk.

A summary of these effects can be found in **Figure 1-10** below. In this example, n-TiO_2 absorbs UV light while Au is responsible for absorbing visible light via the LSPR effects. The Schottky junction between the two materials causes electrons to accumulate on TiO_2 and holes on Au due to the built-in electric field of the space charge layer. Therefore, in this system, reduction occurs on TiO_2 while oxidation occurs on Au.

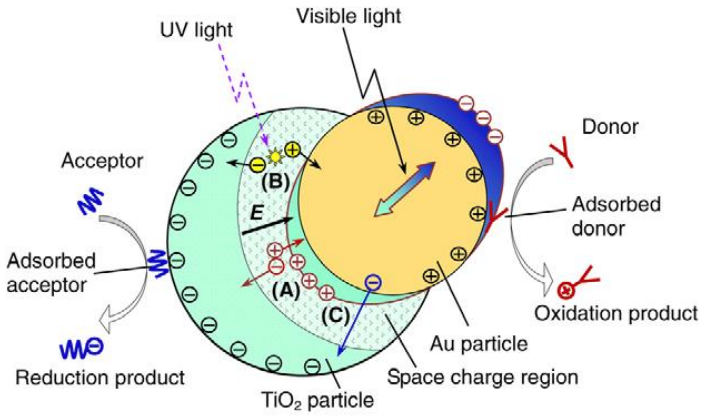

Figure 1-10. Major processes for a composite consisting of n-type TiO_2 and plasmonic Au.[13]

2.3 Photocatalytic Systems

This section will cover photocatalytic systems as an application of materials like TiO_2. First, the basic photocatalytic mechanisms will be described in aqueous conditions. Then, two types of photocatalytic systems will be discussed in greater detail: particulate systems and photocatalytic fuel cells.

2.3.1 Photocatalytic Mechanism

Using the theory and processes described above, the photocatalytic mechanism can be described as follows (**Figure 1-11**): (i) an incident photon with sufficient energy strikes the photocatalyst, photo-generating an EHP; (ii) the EHP is either separated and reaches an active site on the surface of the photocatalyst (a), or they recombine, prematurely ending the photocatalytic process (b); and, (iii) successfully separated electrons and holes undergo reduction and oxidation reactions with adsorbed species, respectively. In an aqueous solution, photocatalysts can react with water or other organic compounds to form radical species. These species are highly reactive and are 'resolved' through various redox reactions, eventually leading to products such as CO_2 and H_2O (Equations (1-4 to (1-13).[84]

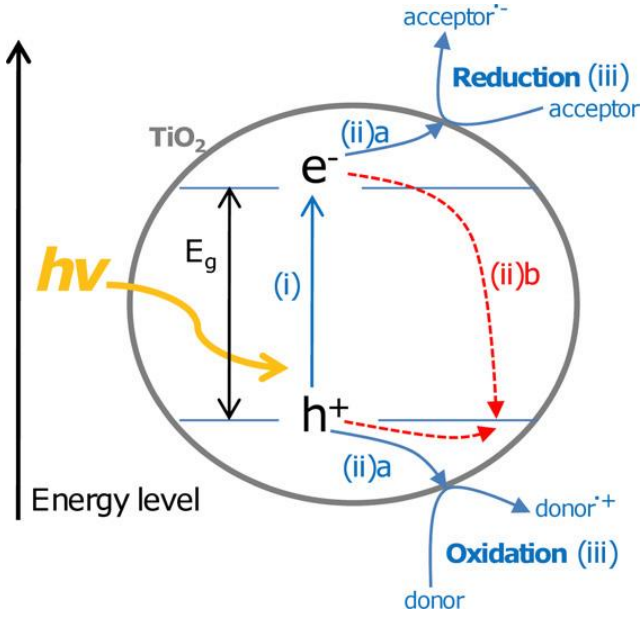

Figure 1-11. Illustration of the basic photocatalytic mechanism.[8]

$$TiO_2 + h\nu \rightarrow e^- + h^+ \quad (1\text{-}4)$$

$$e^- + O_2 \rightarrow O_2 \cdot^- \quad (1\text{-}5)$$

$$O_2 \cdot^- + H^+ \rightarrow HO_2 \quad (1\text{-}6)$$

$$HO_2 + e^- + H^+ \rightarrow H_2O_2 \quad (1\text{-}7)$$

$$H_2O_2 + e^- \rightarrow \cdot OH + OH^- \quad (1\text{-}8)$$

$$H_2O_2 + O_2 \cdot^- \rightarrow \cdot OH + OH^- + O_2 \quad (1\text{-}9)$$

$$2O_2 \cdot^- + H_2O \rightarrow O_2 + HO_2 \cdot^- + OH^- \quad (1\text{-}10)$$

$$h^+ + TiOH/OH^-/H_2O \rightarrow R/R \cdot / \cdot ROH \quad (1\text{-}11)$$

$$\rightarrow O_2 \cdot^-, HOO \cdot, HOOH, HOO^-, HO \cdot, OH^-, H_2O \quad (1\text{-}12)$$

$$\rightarrow H_2O + CO_2 \quad (1\text{-}13)$$

Based on this reaction mechanism, there are four main requirements for a strong photocatalytic material: (i) chemical stability; (ii) absorbance over a wide light spectrum; (iii) high electron conductivity; and (iv) high specific surface area. These four requirements will be described in greater detail below:

Chemical Stability

Chemical stability and photo-corrosion resistance is an important property of photocatalysts for three reasons: First, a catalyst by definition is not consumed during a chemical reaction; second, the decomposition of a catalyst means that it can no longer be used and must be replaced with new catalyst; and third, the decomposition of a catalyst can produce harmful or dangerous products.[85]

One example of a good photocatalytic material lacking photo-corrosion resistance is cadmium sulfide (CdS). CdS has a band gap of 520 nm (2.39 eV), making it a candidate material for visible-light photocatalysis.[86] However, one issue with CdS, along with many other metal sulfides, is that it can easily undergo photo-corrosion via the oxidation of S^{2-} (Equations 1-14 to 1-16). Not only does this destroy the photocatalyst and lower overall activity, but this decomposition also introduces toxic dissolved Cd^{2+} into solution, which is extremely detrimental to health and quality of life.

$$CdS + h\nu \rightarrow e^- + h^+ \quad (1\text{-}14)$$

$$CdS + 2h^+ \rightarrow Cd^{2+} + S(s) \quad (1\text{-}15)$$

$$CdS + 2O_2 \rightarrow Cd^{2+} + 2SO_4^{2-} \quad (1\text{-}16)$$

For this reason, unstable catalysts such as CdS require either a hole-scavenging species to reduce the rate of self-oxidation (such as a S^{2-}/SO_3^{2-} system),[86] or another co-catalyst that can accept holes from CdS, thus preventing oxidation of S^{2-}.[87]

Absorption Spectrum

The absorption requirements for a photocatalytic material appear obvious at first. The smaller the band gap the wider the range of light that can be absorbed. For example, the anatase phase of titanium dioxide (TiO_2) has a band gap of 3.2 eV and can only absorb light within the ultraviolet (UV) range.[2] As shown previously, CdS has a band gap of 2.39 eV, and can therefore absorb UV light as well as part of the visible-light spectrum.

However, it is important to understand the redox potentials and band gap positions in materials, as these potentials determine the movement of charge-carriers. For example, in the case of photocatalytic water splitting, the semiconductor must straddle both the H^+/H_2 reduction potential (0 eV vs. SHE) and the H_2O/O_2 oxidation potential (1.23 eV vs. SHE).[88] Based on **Figure 1-12** below, the band gaps of the semiconductors on the left are large (UV-active only) but are able to induce photocatalytic water splitting. The semiconductors in the middle are unstable because they are susceptible to redox reactions and decomposition. Lastly, the semiconductors on the right have unsuitable band edge positions. This means that the conduction band or valence band are too positive or negative to induce a reduction or oxidation reaction with water, respectively.

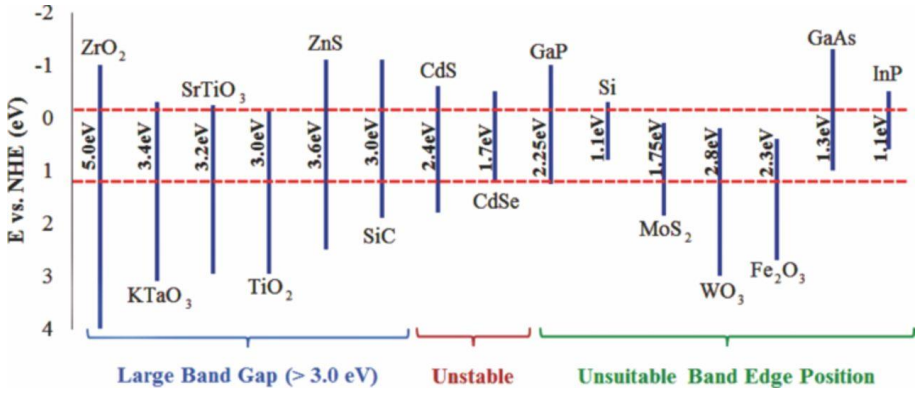

Figure 1-12. Redox potentials of various materials in evaluating suitability for water splitting. Reprinted with permission from publisher.[88]

Therefore, although smaller band gaps are desired for their absorption of higher wavelengths, one must guarantee that the band edge positions are suitable for the desired redox reaction. At the same time, if the desire redox reactions are known, then it is possible to find or tailor the best material with the most appropriate redox potentials to drive the reactions forward.

The absorption spectrum can therefore be increased by: (i) finding or synthesizing a material with a small band gap that perfectly straddles the desired redox reaction; (ii) doping a large band gap material to create intermediate states, effectively lowering the band gap; or, (iii) heterostructuring a large band gap material with a small band gap material to create a wider absorption spectrum.

Electron Conductivity

A material's electrical conductivity is defined as its ability to allow the flow of electric current.[89] The higher the conductivity, the more easily electrons can move. Photocatalytic materials are by nature semiconductors and therefore have no energy levels near their Fermi levels. This means that photocatalysts intrinsically have low conductivities. However, it is possible to improve the conductivity of photocatalysts by creating a composite with a conductive material such as a carbonaceous material. The crystal structure of the catalyst can also be improved to reduce the amount of defects and increase grain boundary size that can act as traps for charge-carriers.[90]

Surface Area

The surface area of a photocatalyst is important because an increased amount of active surface sites allows for more active oxygen species and adsorbing target species for decomposition.[91,92] Because active sites are only found at the interface between the catalyst and the target medium, a high specific surface area ($m^2\ g^{-1}$) is generally desired for all photocatalytic applications.

Given the criteria mentioned above, different photocatalytic materials have been proposed and are currently being researched.[93,94] Relevant classes of materials include metal oxides, metal sulfides, and nitrides. Metal oxides are represented mainly by TiO_2,[2 24] ZnO,[95,96] α-Fe_2O_3,[97,98]

and WO_3,[99,100] though other binary metal oxide photocatalysis exist.[93] Ternary metal oxides such as $SrTiO_3$[101,102] and $BiVO_4$[103,104] have also been gaining attention as potential visible-light photocatalysts. Still, various other metal oxide combinations have been tested for their photocatalytic activity.[105,106] Potential metal sulfide photocatalysts include CdS,[107,108] ZnS,[109,110] and more recently MoS_2 and WS_2.[111] Lastly, nitrides such as graphitic-C_3N_4 have been gaining attention for its simple and inexpensive synthesis and visible light activity.[112,113] For the sake of brevity, this thesis focuses mainly on photocatalytic TiO_2 and its various forms.

2.3.2 Particulate Systems

Particulate systems are one of the simplest methods for evaluating the photocatalytic activity of a material.[114,115] These systems benefit from maximizing the available surface sites on the catalyst, and particle suspensions remove mass transport issues associated with immobilized catalysts. Particulate systems may be in the form of batch or continuous flow reactors. An example of a batch reactor is proposed by the United States Department of Energy (DOE) for the production of hydrogen gas (**Figure 1-13a**).[115] A popular configuration for continuous flow reactions with both particulate suspensions and immobilized catalysts are compound parabolic collecting reactors (**Figure 1-13b**). Particulate systems are normally associated with solution-based photocatalysis, which involved waste water treatment, water electrolysis, and hydrocarbon cracking.

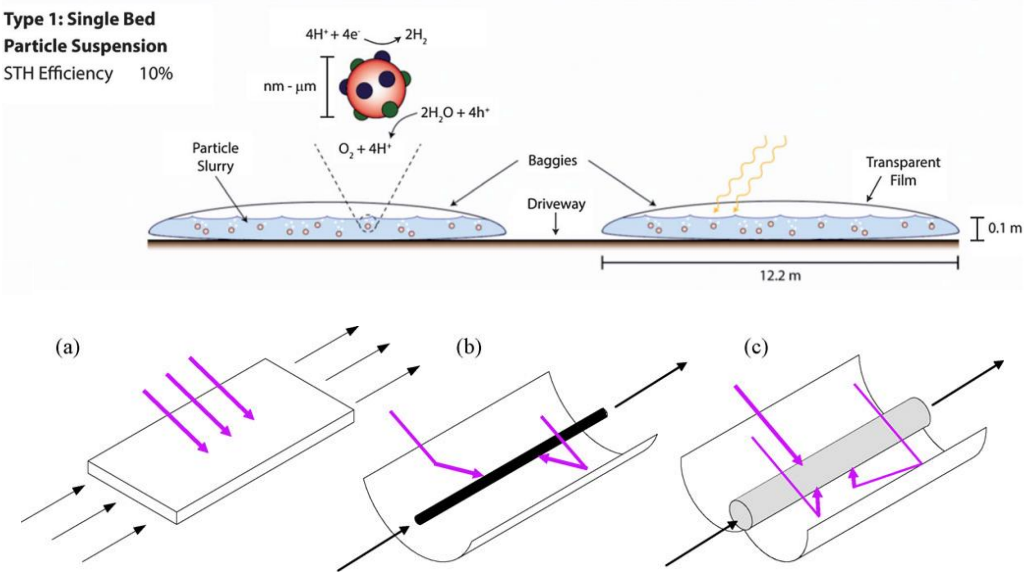

Figure 1-13. (a) Examples of a batch reactor proposed by the DOE for hydrogen production, and (b) continuous flow reactors, culminating in the well-known compound parabolic collecting reactor.

In solution-based photocatalysis, many different target species are tested at the lab-scale including the degradation of pharmaceuticals and organic compounds, and the reduction of heavy metal ions.[116-119] At the same time, model compounds are used to provide a standard by which different research groups can compare results. One such model compound is $C_{16}H_{18}N_3SCl$, or methylene blue (MB), a textile dye that is considered toxic in high concentrations and a pollutant in textile effluents.[120] MB is a heterocyclic aromatic compound that easily dissolves in H_2O to form a positively charged molecule.[121] The adsorption of MB on TiO_2 and carbonaceous materials follows a monolayer Langmuir type isotherm.[122,123] This means that MB will not form multiple layers on these surfaces, and that an equilibrium adsorption concentration of MB exists in solutions containing excess MB. Finally, as a dye the decolouration of MB provides a visual means of determining photocatalytic activity.

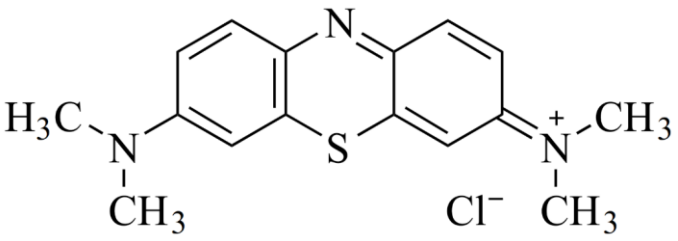

Figure 1-14. Chemical structure of methylene blue.

2.3.3 Photocatalytic Fuel Cells

Photocatalytic fuel cells are a type of photoelectrochemical cell that have been gaining popularity in recent years. Understandably, a photocatalytic fuel cell is the combination of fuel cell and photocatalyst technologies.

Fuel cells are electrochemical devices that use a fuel (chemical energy) to generated electrical power with virtually zero emissions when hydrogen is used as the fuel. Unlike a battery, fuel cells are energy conversion devices rather than energy storage devices and require a continuous source of fuel. In a conventional hydrogen fuel cell, hydrogen gas is fed to the anode and oxidized to protons (H^+), releasing electrons. Electrons run through an external circuit, providing power, while protons transfer to the cathode through the polymer electrolyte membrane (PEM) and undergo reduction to form water as the reaction product.

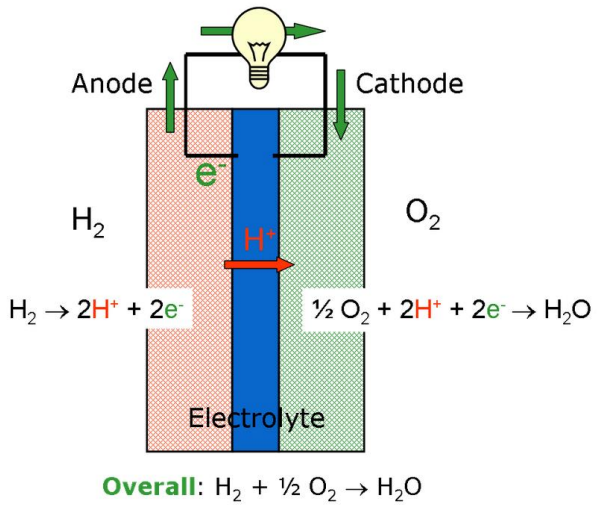

Figure 1-15. Basic operating mechanism for a polymer electrolyte membrane fuel cell.[124]

Like a fuel cell, photocatalytic fuel cells use fuel consumed at the anode in order to generate electrons and ions that are consumed at the cathode in an oxygen reduction reaction (**Figure 1-16**). Like a photocatalyst, photocatalytic fuel cells rely on photocatalytic materials in the anode (or photoanode) to generate holes (h^+) that can catalyze the fuel oxidation reaction. Because the anode is photoactive, the current collector for the anode is typically transparent, utilizing a transparent conducting oxide such as fluorine-doped tin oxide (FTO) on a glass substrate.

Although the fundamental concepts behind this technology have been well-studied in literature in photoelectrochemical cells,[6,19,125] photocatalytic fuel cells as the specific application of photoelectrochemical cells have only appeared more recently in the past five years.[126-128] In a typical photocatalytic fuel cell, oxidation of the fuel via holes occurs at the photoanode under light irradiation, leaving behind electrons and forming protons as products. Protons diffuse across the electrolyte, while electrons travel through the external circuit creating a current. At the cathode, protons and electrons combine with oxygen to form water.

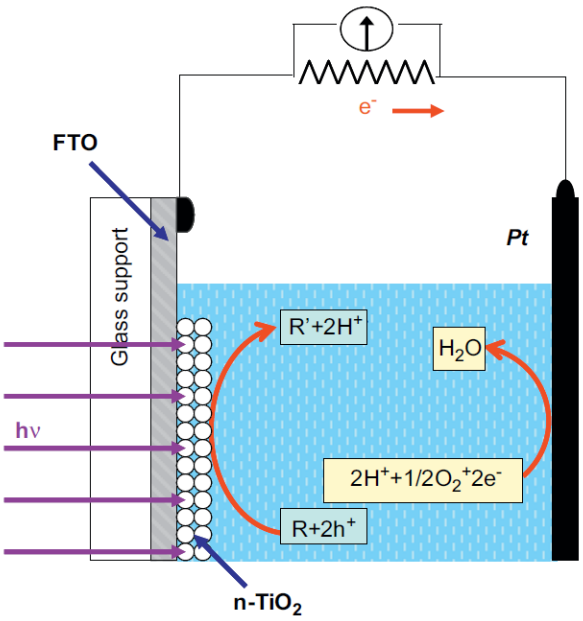

Figure 1-16. Example of a photocatalytic fuel cell using TiO_2 photoanode, Pt cathode, and organic fuel.[129]

Based on this technology, a variety of fuels can be used as long as they are readily oxidized by the photocatalyst on the photoanode. Many fuels have been tested, including many alcohols, ethylene glycol, glycerin, sugars, simple acids, phenols, pure waste water, and even Coca Cola™.[127,128]

Methanol oxidation is a relevant example for photocatalytic fuel cell devices. Methanol is a simple alcohol that is easily oxidized and is a popular model for organic oxidation. The redox potential of $HCHO/CH_3OH$ is found to be lower than that of O_2/H_2O. Therefore, in this system methanol will act as the reducing agent, donating electrons to oxygen gas, which acts as the oxidizing agent.

$$HCHO + 2H^+ + 2e^- \leftrightarrow CH_3OH \qquad E^0 = +0.13\,V\ vs.SHE \qquad (1\text{-}17)$$

$$O_2 + 4H^+ + 4e^- \leftrightarrow 2H_2O \qquad E^0 = +1.23\,V\ vs.SHE \qquad (1\text{-}18)$$

Using a photocatalyst in acid/neutral media, this reaction can be accomplished in a similar fashion. Under anaerobic conditions, it is also possible to accomplish hydrogen reduction at the cathode:

$$2H^+ + 2e^- \rightarrow H_2 \qquad E^0 = 0\,V\ vs.SHE \qquad (1\text{-}19)$$

The efficiency of a photocatalytic fuel cell can be calculated in a couple of ways. The efficiency of a photovoltaic device can be determined by the ratio of the output power and the input power. The external quantum efficiency (EQE) of a device is the ratio of the number of charge carriers produced by a cell to the number of photons incident on the cell, and is given by (Equation 1-20):[6]

$$\eta = \frac{(E - V_{app}) \times I}{P} \qquad (1\text{-}20)$$

Where *E* is the potential of the reaction, V_{app} is the applied voltage (if applicable), *I* is the current, and *P* is the incident irradiance. Proper care must be taken with using this equation to calculate efficiency, as the nature of the reaction must be clear in order to provide a potential, and the current value corresponds to photocurrent only.

The internal quantum efficiency (IQE) is the ratio of the number of charge carriers produced by the cell to the effective number of photons absorbed by the cell (Equation 1-21).[6] IQE values are

more difficult to obtain because they require a proper calculation of the effective number of absorbed photons per unit of time, N_{eff}. In this calculation, N_m corresponds to the number of molecules decomposed per unit of time, and n corresponds to the number of electrons involved in the decomposition.

$$\eta = \frac{N_m \times n}{N_{eff}} \tag{1-21}$$

2.3.4 Photocatalytic Fuel Cell Technologies for Waste water Treatment

As mentioned previously, various fuels can be used in photocatalytic fuel cell as long as they are readily oxidized by the photoanode. This implies that organic compounds commonly found in waste water streams could also be used in a similar system to generate electricity. In fact, these systems are already being designed with limited success.[130-132]

For example, Li et al., used textile waste water as a fuel source in a photocatalytic fuel cell to generate 0.0113 mW cm^{-2} under UV light at a removal rate of 8.4 mg L^{-1} h^{-1} of oxidizable organic material.[130] Zhang et al. used effluent from a waste water treatment plant to generate 0.018 mW cm^{-2} under visible light at a removal rate of 3.1 mg L^{-1} h^{-1}.[131] Wang et al. used municipal waste water to produce an impressive transient power density of ~ 3 mW cm^{-2} (**Figure 1-17a**).[132] Using this waste water, H_2 gas could also be produced at the cathode once all other more favourable fuel sources were consumed (i.e. Cu^{2+}/Cu, O_2/H_2O). Unfortunately, this system suffers from instability due to the use of a dye sensitizer (N719) that leaches into water over time (**Figure 1-17b**). The instability of such a dye can drastically decrease the overall performance of a photocatalytic fuel cell.

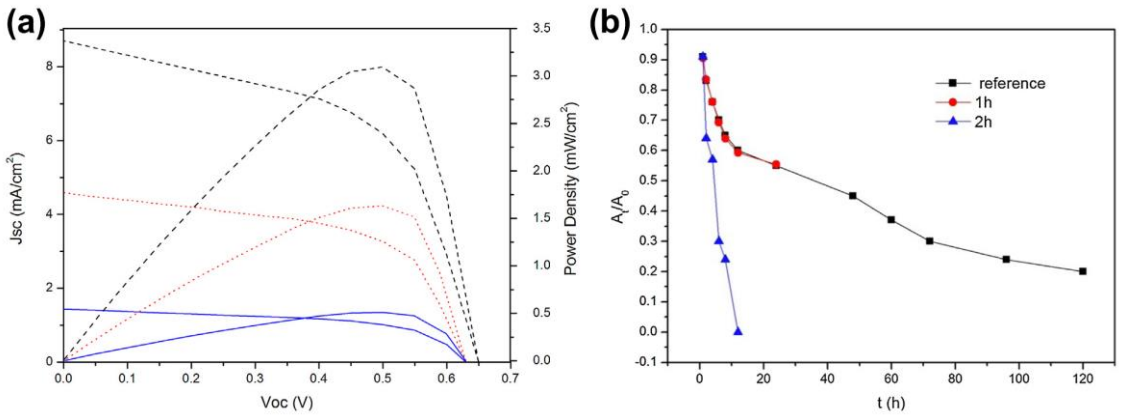

Figure 1-17. (a) IV and power curves of PFC using municipal waste water over a 70 min period.(b) Relative absorbance of dye molecule (at 510 nm) as a function of time and waste water replacement frequency.[132]

There has yet to be a demonstration of a photocatalytic fuel cell that can treat waste water effluents of higher concentrations over extended periods of time. A possible reason for this is the general drop in coulombic efficiency with increasing organic waste concentration.[133]

2.4 TiO_2 in Li-Ion Batteries

Like many other nanomaterials, TiO_2 has been used in various applications apart from photocatalysis. With regard to Li-ion battery technologies, TiO_2 has been successfully implemented as an anode material with high stability and power capabilities.[134] Li-ion batteries are a type of electrochemical storage device that uses the movement of Li^+ to store and discharge energy. The general operating mechanism of a Li-ion battery is shown in **Figure 1-18**. A typical battery consists of an anode (typically graphite), a cathode (typically a transition metal oxide like $LiCoO_2$), and an ionically conductive electrolyte.[135] During charging, Li^+ delithiates from the cathode and moves to the anode. During discharge, the reverse reaction naturally takes place due to the difference in binding energy between the two electrodes.

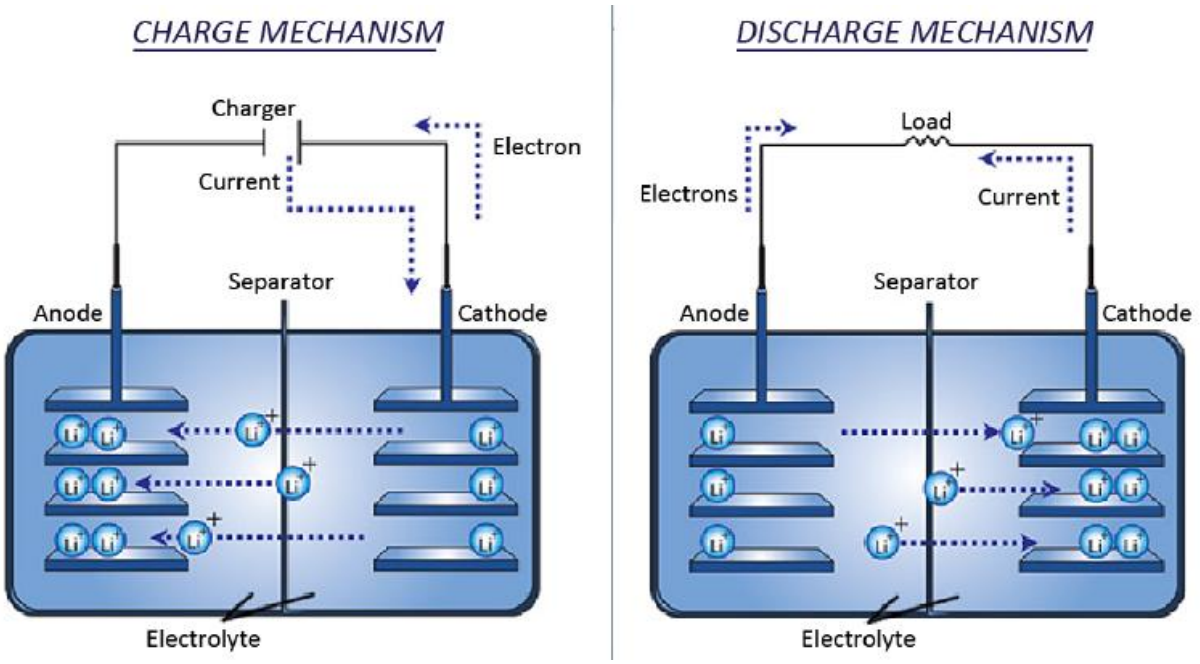

Figure 1-18. General operating mechanism for Li-ion batteries.[136]

TiO_2 provides alternative electrochemical properties to conventional graphite anodes because they have a greater potential vs. Li/Li^+ (1.7 V vs. Li/Li^+ versus 0.2V vs. Li/Li+ for graphite).[137] This property allows TiO_2 to avoid parasitic reactions (such as SEI formation and Li plating) that take place at lower potentials and can cause safety issues for battery operation. In addition to this property, TiO_2 also undergoes very little (~4%) volume change during lithiation, which greatly improves the stability of the material during operation.

In order to be effective for Li-ion batteries, TiO_2 materials should have appropriate electrochemical properties such as short ion diffusion paths and highly accessible surface area. Short ion diffusion paths ensure that complete lithiation of TiO_2 can occur and the capacity of the electrode can be maximized. Highly accessible surface area ensures that the entirety of TiO_2 is accessible to electrolyte regardless of electrode thickness. This property requires electrode

materials to have regular porosity. Certain TiO_2 materials, such as 3DOM morphologies discussed in *Section 2.2.2*, have the potential to be highly effective anode materials for Li-ion batteries because they satisfy these requirements. 3DOM structures have minimal wall thickness that allows for complete lithiation of the material, and its long-range ordered porosity allows for electrolyte to access the inner surfaces of the material regardless of electrode thickness.

2.5 Summary

This section has covered the fundamentals of semiconductor theory and the operating principles of photocatalysis. Background regarding TiO_2 as a photocatalytic material was given in greater detail, highlighting its crystal structure, large redox potential, and stability. The synthesis of TiO_2 is explained, detailing the various possible TiO_2 structures found in literature, including differences in morphology, doping, and heterostructuring. 3DOM structures and plasmonic co-catalysts were highlighted as potential solutions for improving the photocatalytic activity of TiO_2.

Basic attributes of a good photocatalyst were also given: chemical stability, high absorbance, high conductivity, and high specific surface area. A brief overview of photocatalytic particulate systems was also discussed, as well as the use of methylene blue as a model for the photodegradation of organic compounds. Photocatalytic fuel cells were also described as an application of photocatalysis. Finally, the use of TiO_2 materials in Li-ion batteries was discussed as an alternative application to photocatalysis.

3.0 Experimental Methods

Materials can be characterized and evaluated using a wide variety of techniques and instrumentation. For the purpose of this thesis, only the most fundamental and relevant characterization techniques will be discussed. Characterization can be separated into three types: physical, electrochemical, and performance (**Table 3-1**). Performance characterization includes specific experiments used to evaluated performance in **Chapters 4 to 6**. Each technique in **Table 3-1** will be described in further detail below.

Table 3-1. Characterization techniques used in this proposal.

Evaluation	Characteristic	Type of Test
Physical characterization	Morphology	SEM, TEM
	Crystal phase	TEM (SAED), XRD
	Composition	EDX, XPS, Raman
	Optical band gap	DRS
	Surface area and porosity	BET
Electrochemical characterization	Photocurrent Response	Potentiostat
	Open Circuit Voltage	
	Polarization Curve	
	Impedance	
Experimental methods for catalyst testing	Solution Photocatalysis	UV-Vis
	Photocatalytic Fuel Cell Testing	
	COD Testing	
	Li-ion Battery Testing	

3.1 Physical characterization

3.1.1 Morphology

Scanning electron microscopy (SEM) is perhaps the most popular characterization technique for obtaining the topographical and morphological features of a material. This type of microscopy benefits from the use of electrons as opposed to conventional photons in optical microscopy which are limited to wavelengths within the visible-light spectrum. Based on the de Broglie relation (Equation (3-1), SEMs are typically able to resolve features down to 1 nm in size. If an even greater resolution is required, transmission electron microscopy (TEM) can be used. TEMs employ even higher acceleration voltages, which produce electrons of even smaller wavelengths than SEMs. It should be noted that TEMs operate based on transmission, therefore samples must be thin enough for electrons to pass through.

$$\lambda_{DB} = \frac{h}{p} = \frac{h}{\sqrt{2m_e E_b}} \tag{3-1}$$

In this work, SEM and TEM techniques were used to obtain the morphology and general structure of synthesized photocatalysts before performing further characterization. Morphology can also inform other properties of the material such as composition and electronic properties.

3.1.2 Crystal phase

TEMs can also be used to ascertain the crystal structure of a material using Selected Area Electron Diffraction (SAED). This is done by moving the focal plane of the electron beam from the imaging plane to a fluorescent screen. This generates a diffraction pattern which can provide information about the crystal structure and orientation of the sample.

X-ray Diffraction (XRD) also characterizes a material based on its diffraction pattern using the Bragg model (Equation (3-2). This model says that, given a crystal structure consisting of evenly-spaced crystal sheets (of lattice spacing *d*), incident light that diffracts off of each of these sheets will interfere constructively when the angle θ between the plane and the incident light results in a path-length difference equal to an integer multiple (n) of the wavelength of light (λ).

$$2dsin\theta = n\lambda \tag{3-2}$$

When the signal intensity of this constructive interference is plotted as a function of 2θ, an XRD spectrum can be obtained and compared against a database to determine its composition and crystal structure.

In this work, XRD was used to determine the crystal structure and phase of all synthesized materials.

3.1.3 Composition

The elemental composition of materials can be ascertained through various characterization methods, including XRD, SEM and TEM. Particularly, energy dispersive X-ray spectroscopy (EDX) analysis can be used in conjunction with SEM and TEM techniques to get more information regarding the elemental composition of materials. EDX analysis is done by hitting a sample with an excitation source such as an electron or X-ray beam. When this beam strikes an atom, it can excite an electron out of its ground state, leaving behind a vacancy. When an electron at a higher energy level relaxes to fill this vacancy, the atom emits an X-ray that corresponds to the difference in the two energy levels which is characteristic of the element itself.

This phenomenon allows EDX to analyze the elements within a material, and to an extent, the composition of elements within a material. In addition, because EDX is typically paired with SEM and TEM techniques, EDX analysis can be performed as a function of area and give spatial composition.

X-ray photoelectron spectroscopy (XPS) is another elemental analysis technique that is similar to EDX. XPS utilizes an X-ray beam to knock out core electrons of atoms, and then measure the binding energy of the released electrons based on its resulting kinetic energy.

$$\mathrm{E_{binding}} = E_{photon} - E_{kinetic} \tag{3-3}$$

XPS provides much more detailed information about the surface of a material than EDX because XPS can provide additional information, including electronic states and chemical interactions.

In this work, EDX was used to estimate the elemental composition of synthesized materials, and XPS was used to confirm the presence of Ag in **Chapter 6**.

Raman spectroscopy is another characterization technique that can provide the crystal phase and composition of a material. Raman spectroscopy measures light irradiation that undergoes inelastic scattering when interacting with molecular bonds due to the change in polarizability of the molecule during vibration. Raman is specifically useful for analyzing polyaromatic hydrocarbons due to their characteristic peaks at 1360 cm^{-1} (D band) and 1560 cm^{-1} (G band). The G band is due to bond stretching of sp^2 atoms in rings and chains, and the D band is due to the breathing modes of sp^3 and sp atoms in rings.[138] Therefore, the ratio between the intensity of these two bands (I_D/I_G) is commonly used evaluate the defect quantity within graphitic materials.

In this work, Raman was used to evaluate the change in I_D/I_G ratio in the carbonaceous materials used in **Chapter 4**.

3.1.4 Optical band gap

The optical band gap of a material can be estimated using a technique called diffuse reflectance spectroscopy (DRS). DRS is a specific type of UV-Vis spectroscopy that uses light irradiation to obtain not the change in transmittance of a sample but rather the change in reflectance.[139] Diffuse reflectance data can be manipulated into a Tauc plot using the Kubelka-Munk transformation, given by:[140]

$$[h\nu \cdot F(R\infty)]^{1/n} = A(h\nu - E_g) \quad (3\text{-}4)$$

where h is the Planck constant, ν is the frequency of the light source, $F(R\infty)$ is a value proportional to the absorbance, A is a proportional constant, E_g is the band gap, and n signifies the nature of the electron transition. For anatase TiO_2, n = 2, denoting an allowed indirect transition. Once $[h\nu \cdot F(R\infty)]^{1/2}$ is plotted against $h\nu$, the linear region of the resulting graph can be extrapolated to the x-axis to estimate the band gap (expressed in $h\nu$) of the material.

In this work, DRS was used to determine the absorbance spectra and estimate the band gap of synthesized materials.

3.1.5 Surface area and porosity

BET is not so much a characterization technique as it is a theory used to analyze surface area and pore analysis data.[141] BET theory builds upon the foundational Langmuir adsorption theory,

which provides a model for monolayer molecular adsorption, and extends this theory to multilayer adsorption using three assumptions:

1. Gas molecules can adsorb on a solid surface in an infinite number of layers;
2. Individual adsorption layers do not interact with one another; and
3. Langmuir theory can be applied to each individual adsorption layer.

These three assumptions form the basis of BET theory. Surface area measurements are performed by adsorbing N_2 gas onto a material surface and measuring the volume of gas lost and gained during adsorption and desorption at different N_2 partial pressures. Using BET analysis, the total specific surface can be derived based on the monolayer volume of adsorbed gas, the cross-sectional area of the adsorbate species, and the mass of the sample used for characterization.

In this work, BET analysis was used to determine the surface area of synthesized materials.

3.2 Electrochemical Characterization

3.2.1 Photocurrent Response

The photocurrent response of a photocatalyst is determined by measuring the current flow of a photo-electrode with and without light irradiation. Photocurrent response can be used to determine the amount of current that can be produced using a photo-electrode of a specific area and mass loading, and under a specific irradiance. This value is also useful for calculating the amount of fuel being consumed in the photocatalytic fuel cell. Lastly, the behaviour of the photocurrent response can be used to reveal whether the observed current is anode, cathodic, or

mixed. (Current direction is informed by the extrinsic character of the semiconductor, i.e. n-type or p-type.)

3.2.2 Polarization (I-V) Curve

Much like polarization curves are produced for fuel cell and photovoltaic characterization, similar I-V curves can be produced for photocatalytic fuel cells. These curves give information regarding the short-circuit current and open circuit voltage, as well as the relationship between operating current and voltage. I-V curves can give information about the maximum operating power density of a cell, the efficiency of the cell, and the nature of the inefficiencies in a cell.

3.2.3 Electrochemical Impedance Spectroscopy

Electrochemical impedance spectroscopy (EIS), sometimes called dielectric spectroscopy, is a measure of a material's dielectric properties as a function of frequency. This technique is performed by applying an alternating voltage to an electrode interface and measuring the response for a range of frequencies.[142] When displayed as a Nyquist plot, plotting imaginary impedance *Z[Im](Ω)* vs. real impedance *Z[Re](Ω)*, EIS data can reveal information about the impedance and electrochemical behaviour of materials.

In order to extract more quantitative results from EIS data, software was used to model the experimental data against equivalent circuits in order to estimate impedance values. This data was used to confirm the differences in impedance and diffusion resistance between all photocatalytic materials. In typical experiments, samples are scanned from 0.5 MHz to 10 mHz at an alternating signal of 5 mV.

3.3 Experimental Methods for Catalyst Testing

3.3.1 Solution Photocatalysis

The solution-based photocatalytic decomposition of an optically active material can easily be measured using UV-Vis spectroscopy. UV-Vis spectroscopy is a type of absorption spectroscopy that uses electron transitions within transition metal ions, conjugated organic molecules, and biological macromolecules to characterize their nature and abundance.[143]

Using Beer-Lambert's law (Equation (3-5), a material's absorbance can be related to its concentration in a solution given a constant path length, L, and molar extinction coefficient, ε.

$$A = \epsilon c L \tag{3-5}$$

This property is extremely useful for measuring how the concentration of a compound in solution may vary with time. Concentration values from UV-Vis can then be used to calculate the reaction rate of the chemical reaction. Based on a general reaction, A + B → C + D, a general formula can be given (Equation (3-6):

$$r = k[A]^n[B]^m \tag{3-6}$$

where r is the reaction rate, k is the rate constant, $[A]$ and $[B]$ are the concentration of reactants, and n and m are the order of reactions for reactants A and B. For the simple photodegradation of a single compound, only the target compound and the catalyst are taken into account. However, because the concentration of the catalyst should not change during the reaction, the reaction can

be considered a (pseudo) first-order reaction that depends only on the concentration of the target compound (Equation (3-7). From this equation, the rate constant of the reaction can be found as a measure of the activity of a photocatalyst (Equation (3-8):

$$r = \frac{-d[A]}{dt} = k[A] \tag{3-7}$$

$$-\ln\frac{[A]}{[A]_0} = kt \tag{3-8}$$

where $-ln[A]/[A]_0$ is plotted as a function of t and k is the slope of the curve. In photocatalytic degradation, UV-Vis spectroscopy was used to determine the rate of decomposition (or decrease in concentration) of a target species during light irradiation.

3.3.2 Photocatalytic Fuel Cell Testing

In a typical photocatalytic fuel cell experiment, the photocatalyst is deposited onto a transparent and conducting current collector such as indium-doped tin oxide (ITO) on either quartz glass or thin-film polyethylene terephthalate (PET). The electrode is then used as a photoanode in a two-electrode system consisting of a Pt-based counter electrode and waste fuel as the electrolyte. In a batch system, electrolyte is added directly into the system as a one-compartment photoelectrochemical cell. In a continuous flow system, electrolyte is pumped into the one-compartment cell via a peristaltic pump. The basic configuration for such a cell is shown in **Figure 3-1**.

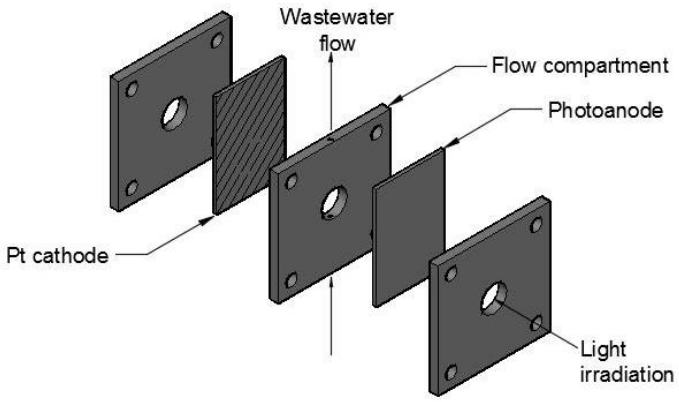

Figure 3-1. Configuration for a simple one-compartment flow-photocatalytic fuel cell.

Photoelectrochemical testing was performed using two light sources under continuous irradiation: 1) a single-wavelength 1 W 365 nm LED, and 2) a solar simulator (AM 1.5G, 100 mW cm^{-2}). The irradiance of the UV LED was estimated and controlled based on the emission pattern of the LED and its distance from the photocatalyst surface.

The photoelectrochemical properties of the fabricated cell could be determined by obtaining information such as photocurrent response, polarization curves, and EIS spectra under different conditions. Photocatalytic fuel testing was used evaluate the performance of photocatalytic materials and devices in **Chapters 5 and 6**.

3.3.3 COD Testing

Chemical oxygen demand (COD) is a measure of oxygen in a solution that can be consumed in a reaction, typically given in mg O_2 L^{-1}. Measuring COD is a means of determining the amount of organics in solution, and is a popular method for determining the amount of oxidizable pollutants in waste water. The first step in obtaining COD is forcing complete oxidation of

organic compounds using a strong oxidizing agent in acidic condition through digestion at high temperatures. The total amount of reduced oxidizing agent is then measured using a photospectrometer. This value corresponds to the amount of O_2 consumed by the organic matter.

This work employs Hach Method 8000 for determining the COD of waste water solutions. This method uses a reagent consisting of potassium dichromate in sulfuric acid solution. The COD reagent is added to the waste water sample and digested at 150°C for 2 h in order to fully oxidize the sample. During this process, the chromate ion ($Cr_2O_7^{2-}$) is reduced to a chromium ion (Cr^{3+}) which has a characteristic absorbance peak at 620 nm.

This method was used to measure the change in COD of brewery effluent in **Chapter 6**.

3.3.4 Li-ion Battery Testing

In a typical Li-ion battery experiment, the synthesized material is used as the anode active material in a half cell using a CR2032-type coin cell. In this cell, Li metal was used as the counter electrode, Celgard 2500 as the separator, and 7:3 (v/v) ethylene carbonate and dimethyl carbonate electrolyte solution containing 1 M $LiPF_6$ as the electrolyte. Typically, binder and conductive additive is mixed with active material to improve adhesion and conductivity. In this work, no binder, additive, or current collector was required, as the synthesized material on carbon cloth acted as a free-standing electrode with a built-in current collector. Coin cells were assembled in an Ar-filled glove box with O_2 and H_2O concentrations maintained below 0.5 ppm to prevent oxidation of battery components. The assembly of the CR2032 coin half-cell is illustrated in **Figure 3-2**.

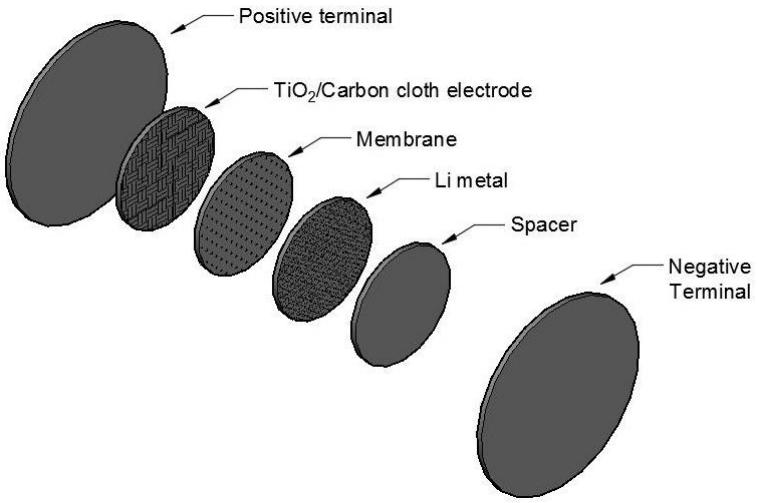

Figure 3-2. Assembly of a sample CR2030 half-cell using a carbon cloth electrode.

Batteries were tested by continuously charging and discharging in order to simulate regular use and evaluate electrochemical performance. This was accomplished by performing two major tests: 1) applying an increasingly larger charging/discharging currents to evaluate the power capabilities of the battery; and, 2) applying a constant charging/discharging current over many cycles to evaluate the cycling stability of the battery.

In this work, battery testing was used to evaluate the performance of TiO_2/carbon cloth electrodes fabricated in **Chapter 4**.

4.0 Flexible, Three-Dimensional Ordered Macroporous TiO_2 Electrode with Enhanced Electrode-Electrolyte Interaction in High-Power Li-Ion Batteries

---

Chapter 4 is based on published work by Lui et al. in the scientific journal *Nano Energy*.

Lui, G.; Jiang, G.; Lenos, J.; Lin, E.; Fowler, M.; Yu, A.; Chen, Z., Advanced Biowaste-Based Flexible Photocatalytic Fuel Cell as a Green Wearable Power Generator. *Advanced Materials Technologies* **2017,** *2* (3).

See **Statement of Contributions** for a detailed summary of contributions from each co-author.

The original intent of this work was to synthesize three-dimensional, ordered, macroporous (3DOM) TiO_2 for the application of photocatalysis in photoelectrochemical cells. This was to be accomplished by confirming the improved photocatalytic activity of 3DOM TiO_2 over P25 in the photo-degradation of methylene blue in solution under UV light and visible light, and then implement the material into a photoelectrochemical cell via the deposition of 3DOM on ITO/glass.

This project encountered several issues, including two major roadblocks: 1) the inability to produce superior photocatalytic activity of as-synthesized 3DOM TiO_2 over that of commercial P25; and more importantly, 2) the inability to fabricate both polystyrene (PS) and 3DOM-type films on indium-doped tin oxide (ITO)/glass substrates. **Figure 4-1** compares the reaction rates of commercial P25 and 3DOM TiO_2 in the photodegradation of methylene blue. In these

experiments, 5 mg photocatalyst was dispersed in a 40 mL of 10 mg L^{-1} methylene blue solution and irradiated with a Xe light source. The calculated reaction rate constants of these type materials were found to be 0.0557 ± 0.004 min^{-1} and 0.0595 ± 0.015 min^{-1}. The improvement in photocatalytic activity of 3DOM TiO_2 was found to be insufficient to warrant additional work after accounting for changes in synthesis parameters including heating temperature and program, solvent, and sol-gel composition.

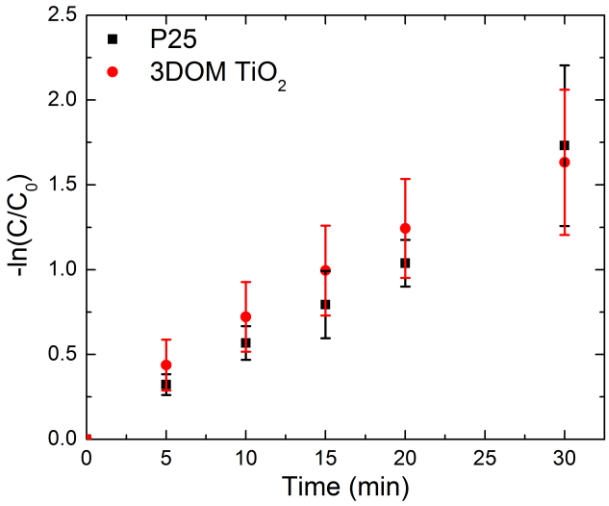

Figure 4-1. Reaction rate comparison between commercial P25 and optimized 3DOM TiO_2.

In addition to the issue of photocatalytic activity, an even more significant issue of applying 3DOM films onto ITO/glass substrates was found. Attempts at replicating various procedures[54,144-146] found in literature proved ineffective for: 1) establishing stable PS films on ITO/glass; and/or 2) establishing stable 3DOM TiO_2 films for photocatalysis. The films were found to easily crack during synthesis and prove unstable during testing.

Based on these results, it was necessary to transfer the application of 3DOM TiO_2 to a different electrochemical system. Based on the absence of free-standing 3DOM materials in Li-ion battery

literature, it was possible to utilize 3DOM TiO_2 as an active material and still draw upon the desired properties of the 3DOM structure such as its long-range order and porosity.

In this chapter, a simple methodology is developed for the in-situ preparation of flexible, 3DOM TiO_2 electrodes with greatly enhanced mass transfer. The 3DOM electrode is fabricated using a polystyrene colloidal crystal templated carbon cloth, and provides significant improvements over conventional nanoparticle electrodes without the use of binder or other additive. When evaluated as an anode in a Li-ion battery, the 3DOM electrode provides outstanding high rate performance. The electrode provides a specific capacity of 174 mAh g^{-1} at a current density of 2 A g^{-1}, which is 2.6 times greater than that achieved with a nanoparticle electrode (68 mAh g^{-1}). The 3DOM electrode also achieves excellent cycling stability, with a capacity retention of 94.8% (181 mAh g^{-1}) over 1000 cycles at 10C (1.7 A g^{-1}) compared to 93.7% (67 mAh g^{-1}) for the nanoparticle electrode. To the best of our knowledge, at the time of publication the performance of our 3DOM electrode is among the highest of binder-free, flexible TiO_2 electrodes. We believe that this methodology is highly useful and is easily transferable to other materials and applications.

4.1 Introduction

Presently, there remains a strong desire to produce flexible energy storage devices that can provide sufficient energy in high-power applications for wearable technologies, automotive vehicles, medical devices, and various flexible consumer products.[147-151] Li-ion batteries (LIBs) are often used for these types of applications because their high energy density.[152,153] However, their poor charge/discharge rates, specifically when compared to other devices such as supercapacitors, prevents them from providing energy in high-power applications.[47,154] It is therefore highly desirable to design a flexible energy storage device that can achieve both high

energy densities and high power densities. Titanium dioxide (TiO_2) is an anode material in LIBs that shows promise in high-power applications due to its highly reversible lithiation process, lack of solid electrolyte interface (SEI) formation, and relatively small volume expansion.[155,156] TiO_2 is also a highly abundant material, relatively non-toxic, and chemically stable.

Nanoparticle electrodes have been used to address the issue of low power densities in LIBs, which is partially caused by the low solid-state diffusion of Li-ions within the electrode material.[157-159] However, achieving high-power LIB performance is still a challenge due to nanoparticle aggregation and low mass transfer within the electrode.[155] In a nanoparticle electrode (**Figure 4-2a**), the dense packing of particles reduces overall surface area and surface area contact with the electrolyte. Any uneven distribution of particles and particle sizes will also reduce the uniformity of contact with the electrolyte. Particle sizes must be sufficiently small without aggregation in order to reduce the Li diffusion path and ensure that complete lithiation is kinetically possible. In sufficiently thick electrodes, it is possible that deeper layers of active material will be completely inaccessible for lithiation (highlighted in orange). Electrons in these traditional electrodes are required to overcome interfacial resistance between particles in order to reach the current collector. These interfacial boundaries are marked in the figure by a yellow 'x'. Lastly, nanoparticle electrodes require binding agents and other additives in order to be practical, which can further impede lithiation kinetics and complicate electrode design.

For these reasons, it is necessary to design more functional electrodes that can improve mass transfer and electrode-electrolyte interaction in a battery. An ideal, high-power electrode should have an interconnected structure which allows for efficient mass transfer, electron transfer, and contact between the electrode and electrolyte.[147,160-162] Therefore, we have synthesized a flexible,

binder-free, three-dimensional ordered macroporous (3DOM) TiO_2 electrode which can provide these characteristics (**Figure 4-2b**). This type of electrode can provide a six-fold advantage compared to nanoparticle electrodes: First, in a 3DOM electrode the ordered porosity of the electrode ensures an even distribution and high surface area contact between the electrode and the electrolyte. This in turn improves mass transfer of ions to the electrode surface and promotes complete lithiation.[161,163] Second, smaller crystallite sizes are easily achieved as they are defined by the colloidal crystal template, and thin pore walls allow for short diffusion paths and complete lithiation at nearly all surface sites.[62] Third, 3DOM structures can allow electron conductivity through its interconnected structure, overcoming interfacial resistances associated with nanoparticle electrodes.[164,165] Fourth, carbon-coated 3DOM structures (**Figure 4-2c**) can be accomplished in-situ, and can further improve performance by providing alternative, more conductive pathways for electrons. Carbon coating can stabilize the active material during charging and discharging, increasing the cycling stability of the electrode.[166,167] Fifth, the 3DOM electrode can be easily fabricated using flexible current collectors such as carbon cloth in order to form a flexible electrode. Lastly, the 3DOM electrode can be fabricated without the use of binder or other additive.

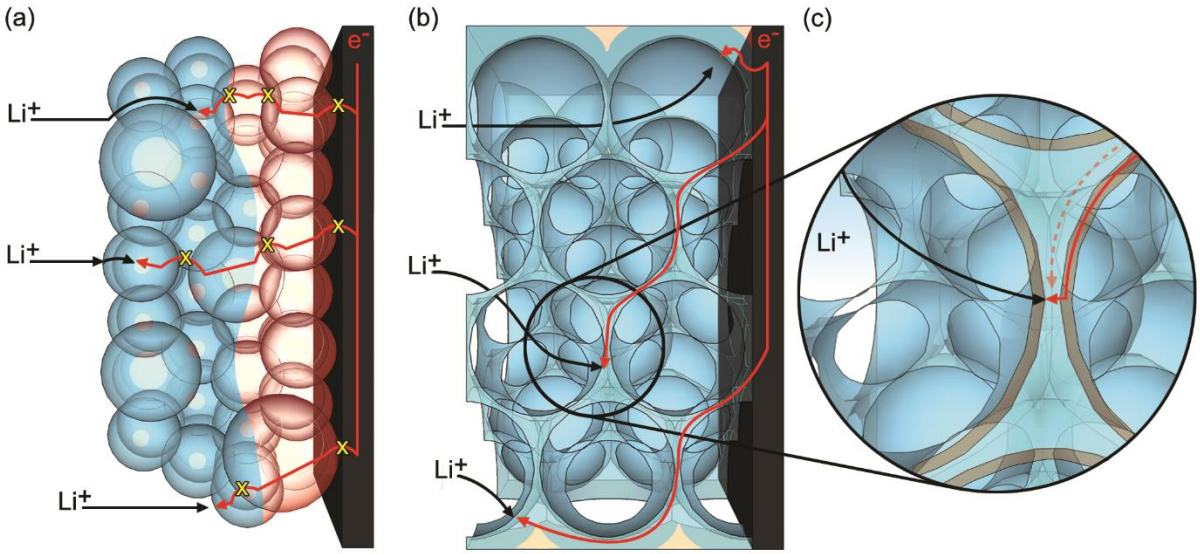

Figure 4-2. Diagram comparing lithiation pathways for (a) nanoparticle and (b) 3DOM electrodes.Active material (TiO_2) is blue, potential inaccessible lithiation sites are highlighted in orange, and carbon coating is brown. Interfacial boundaries in the nanoparticle film are marked with a yellow 'x'.

This flexible, binder-free 3DOM TiO_2 electrode is achieved by depositing a polystyrene (PS) colloidal crystal template on bare carbon cloth. The PS beads are synthesized using emulsion polymerization and the template is deposited on carbon cloth using a simple dip-coating technique. The templated carbon cloth is then infiltrated with a TiO_2 sol gel solution and heat-treated to crystallize TiO_2 and remove the template. When calcined in air, the resulting TiO_2 on carbon cloth has a pseudo-3DOM structure. When heat-treated in Ar, the resulting TiO_2 on carbon cloth has a 3DOM structure covered in carbonized polystyrene.

4.2 Experimental Methods

4.2.1 Materials

Styrene, polyvinylpyrrolidone (PVP), potassium persulfate, ethanol, hydrochloric acid, titanium dioxide and titanium butoxide, and polyvinylidene difluoride were purchased from Sigma Aldrich. Carbon black (Super P) was purchased from MTI. Carbon cloth was purchased from Fuel Cell Earth. All chemicals and materials were used as received.

4.2.2 3DOM TiO_2 Electrode

Monodisperse polystyrene (PS) beads were synthesized using an emulsion polymerization reaction. First, distilled de-ionized (DDI) water was boiled for several minutes to remove O_2. This water was used for the remainder of the synthesis procedure. 2.5 g polyvinylpyrrolidone surfactant was dissolved in 200 mL DDI water and placed in a three-neck flask. 0.2 g potassium persulfate was dissolved in 40 mL DDI water and placed in a separatory funnel. The PVP solution was brought to 70°C using an oil bath under stirring. N_2 gas was used to maintain an inert environment. After 10 minutes, 24 mL styrene monomer was added to the PVP solution and resulting mixture was stirred for 15 minutes. Lastly, the potassium persulfate solution was added to the monomer solution drop-wise (~1 drop s^{-1}) using the separatory funnel. This solution was stirred for 24 h to form the final colloidal PS solution which appears milky white. The concentration of the as-prepared PS solution was adjusted to 30 mg mL^{-1} for further use.

Carbon cloth was punched into 12 mm diameter electrodes and cleaned by sonicating in acetone, ethanol, and isopropanol for 20 minutes each. The carbon cloth electrodes were then dipped in the PS solution and dried at room temperature for several hours to form a PS colloidal crystal

template on the surface of the carbon cloth. This process was repeated until a certain mass loading of PS was achieved. This material was denoted as PS-CC.

3DOM TiO_2 on carbon cloth (3T-CC) was obtained by immersing the PS-CC template in a sol-gel solution consisting of 10 mL ethanol, 0.675 mL hydrochloric acid, and 1.415 mL titanium butoxide. The infiltrated electrode was then calcined at 300°C for 2 h and then 450°C for 2 h in air using a ramp rate of 1°C min^{-1} in order to burn off the PS template and form anatase TiO_2. 3DOM TiO_2-carbon on carbon cloth (3T-C-CC) was obtained by heat-treating the electrode using the same heating program as for 3T-CC but in Ar to carbonize the PS template.

For comparison, a TiO_2 nanoparticle electrode was synthesized using 25 nm anatase TiO_2 particles. The TiO_2 particles were mixed with carbon black, polyvinylidene difluoride in a ratio of 80:10:10. The slurry was then cast onto a 12 mm diameter carbon cloth electrode and dried at 100°C in a vacuum oven.

The flow-chart corresponding to this procedure can be seen in **Figure 4-3**.

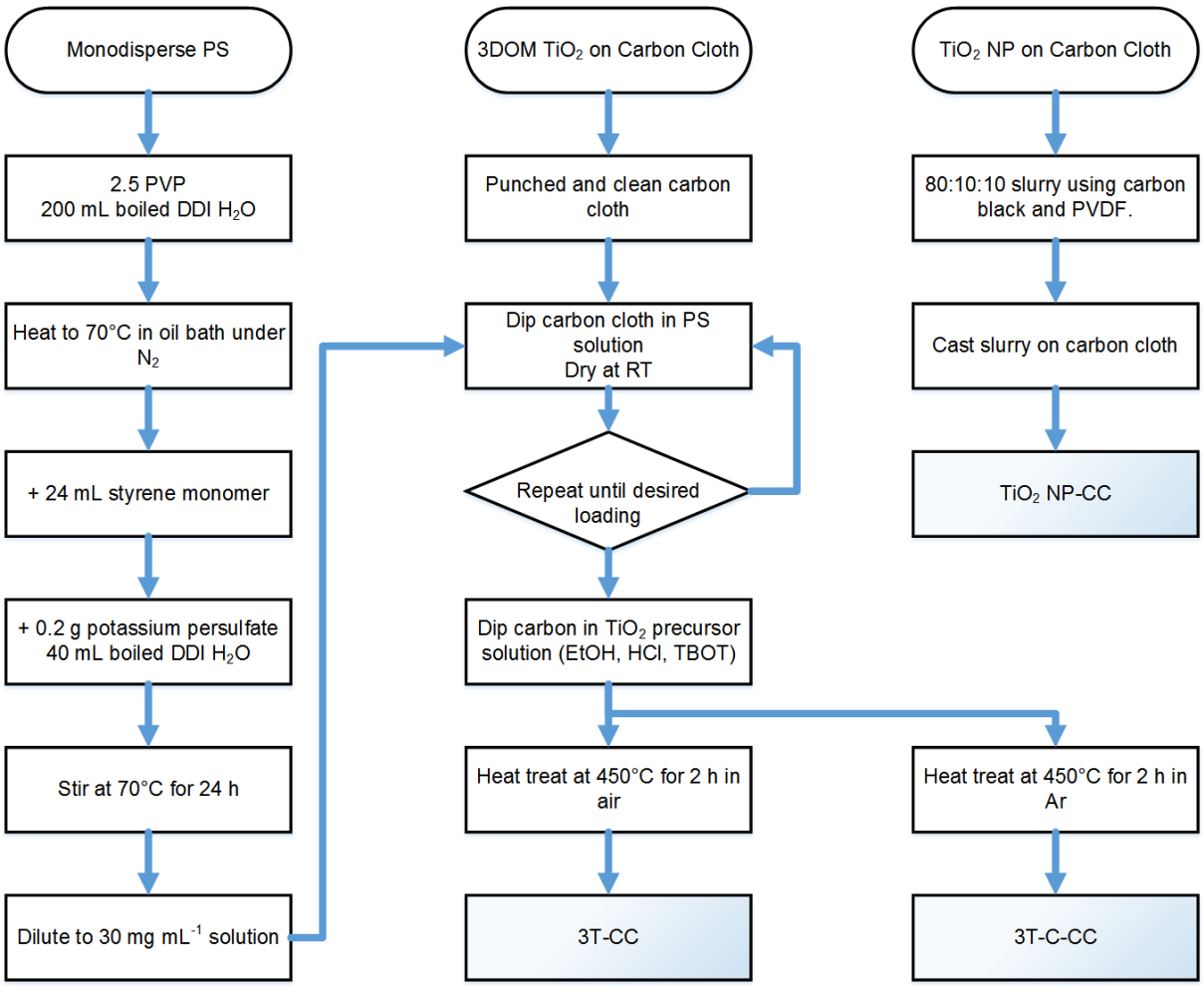

Figure 4-3. Flow-chart outlining the fabrication of 3T-CC, 3T-C-CC, and TiO_2 NP-CC.

4.2.3 Characterization

The morphology and microstructure of the synthesized materials were obtained using field-emission scanning electron microscopy (FESEM, Zeiss ULTRA Plus), transmission electron microscopy (TEM, JEOL 2010F), X-ray diffraction (XRD, Rigaku Miniflex600), and Raman spectroscopy (Bruker SENTERRA).

Electrochemical performance of the electrodes in Li-ion batteries was determined by fabricating a CR2032 coin-type half-cell. A coin cell was fabricated using Li metal as the counter electrode,

a Celgard 2500 separator, and a 7:3 (v/v) ethylene carbonate and dimethyl carbonate electrolyte solution containing 1 M $LiPF_6$. No binder or additive was required for the electrode, and the carbon cloth was used as the current collector. Coin cells were assembled in an Ar-filled glove box with O_2 and H_2O concentrations maintained below 0.5 ppm. Charge-discharge measurements were conducted using a NEWARE BTS-5V10mA battery testing station.

4.3 Results and Discussion

As shown schematically in **Figure 4-4**, after dipping the carbon cloth in the PS solution, the PS beads can self-assemble into a colloidal crystal template along the surface of the carbon cloth fibers (PS-CC). The loading and number of layers of template can be controlled by the number of dip cycles. After infiltrating the PS template with the TiO_2 sol-gel solution and calcining in air, a rough 3DOM TiO_2 film is formed on the carbon cloth fiber (3T-CC). When the templated carbon cloth is heat-treated in Ar, a pristine 3DOM TiO_2 structure covered in carbonized polystyrene is formed on the carbon cloth fibers. This carbonization provides an in-situ, conductive coating for TiO_2.

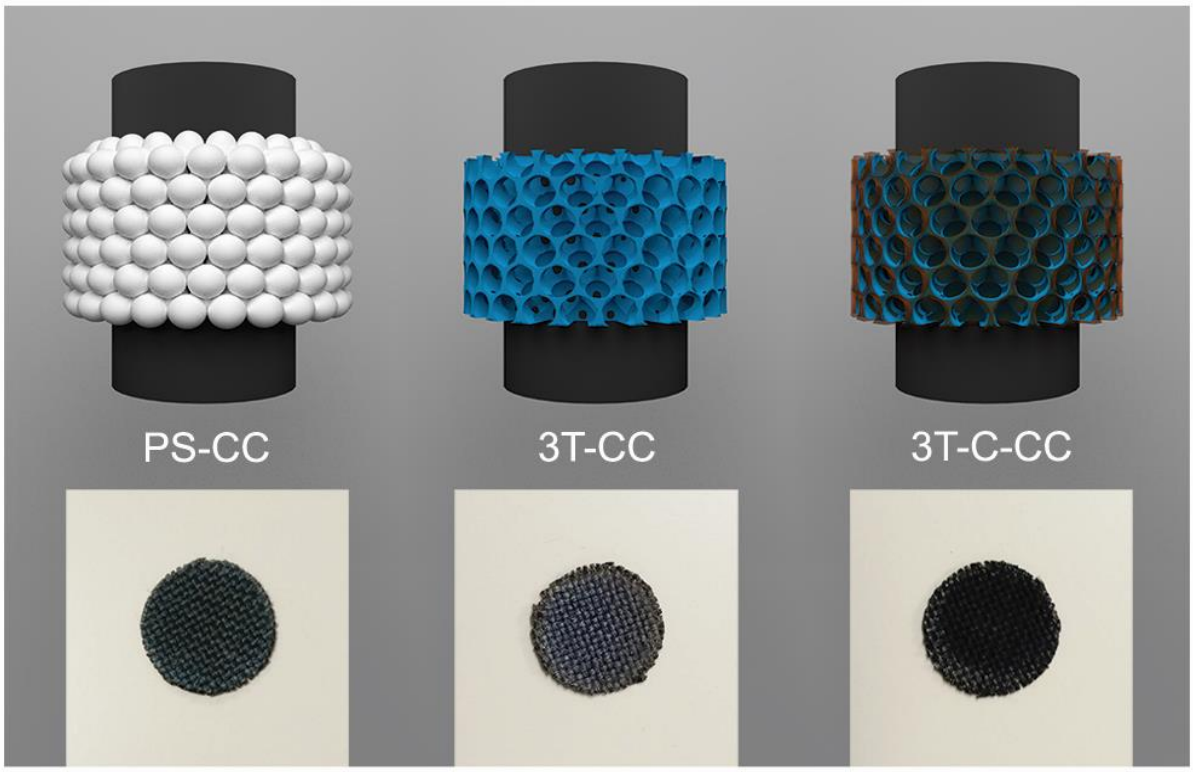

Figure 4-4. Schematic drawing of 3T-C-CC synthesis.(left to right) a carbon cloth dipped in PS solution, forming a PS CCT on the surface (PS-CC); 3DOM TiO_2 formed on carbon cloth after immersion in TiO_2 precursor calcination in air (3T-CC); and carbon-coated 3DOM TiO_2 formed on carbon cloth after immersion in TiO_2 precursor calcination in Ar (3T-C-CC).

The morphologies of the PS-CC, 3T-CC, and 3T-C-CC electrodes were characterized by scanning electron microscopy (SEM). After the dipping cycles, a continuous layer of PS successfully and uniformly grows on the surface of the carbon fiber with a typical FCC structure (**Figure 4-5a** and **4-5d**). The PS spheres are monodisperse and approximately 200 nm in diameter. After calcination in air, the 3T-CC electrode can be obtained with thin pore walls and an average pore size of 180 nm which is consistent with the size of PS template (**Figure 4-5b** and **4-5e**) after a slight reduction in size during heat treatment.[168] A small portion of broken 3DOM TiO_2 can be observed, which may be attributed to the instability of the colloidal crystal

template during heat treatment as well as small imperfections within the template prior to infiltration. By comparison, the 3T-C-CC electrode obtained after heat treatment in Ar is uniformly coated on the carbon fibers (**Figure 4-5c**). The increased wall thickness and decreased pore size (~160 nm) can be found, suggesting successful carbon coating originating from the decomposition and carbonization of the PS (**Figure 4-5f**).

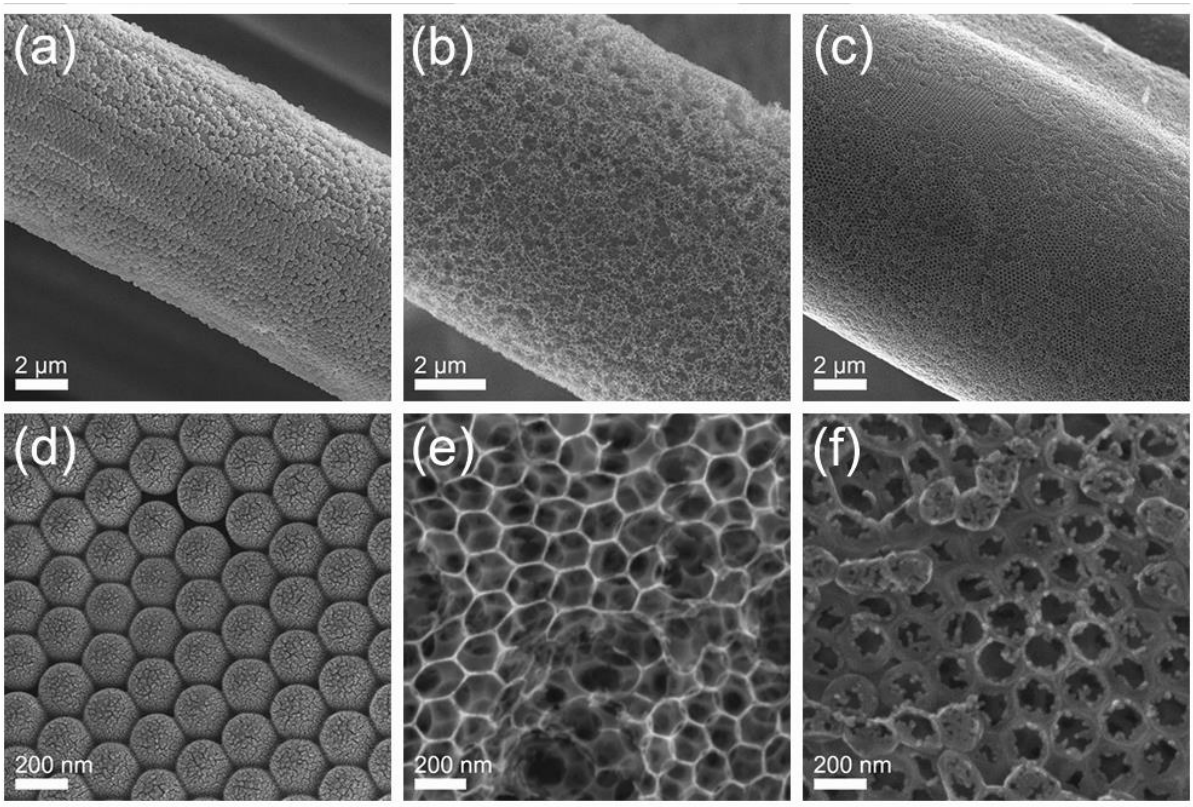

Figure 4-5. Low-magnification SEM images of (b) PS-CC, (c) 3T-C, and (d) 3T-C-CC, and high-magnification SEM images of (e) PS-CC, (f) 3T-C, (g) and 3T-C-CC.

Lastly, **Figure 4-6** shows the stability and flexibility of the as-prepared 3T-C-CC electrode. The carbon cloth maintains its porosity after the deposition of 3DOM TiO_2, allowing light to pass through. The electrodes also retain their form under various forms of mechanical stress, such as bending and twisting, due to the flexibility of the carbon cloth and the strong adhesion of the

3DOM structure to the surface of the carbon cloth. Further testing showed that the electrodes maintained virtually all mass after being subject to severe bending (r = 2 mm) for 500 cycles (**Figure A-1**). The strong mechanical stability of the electrode suggests that it can be used in flexible electronic applications.

Figure 4-6. Optical images showing (from left to right) light transmission, bending, and twisting of the as-prepared electrode.

Figure 4-7a and **4-7b** show TEM images of the 3T-C structure. The pore size of the 3DOM material is consistent with that found in the SEM images, and the selected area diffraction (SAD) pattern suggests that the material is polycrystalline. The HRTEM image in **Figure 4-7b** clearly shows the amorphous structure of carbon. The image also reveals that the TiO_2 making up the pore walls of the 3DOM material consists of nanocrystalline anatase (d_{101} = 0.35 nm) in an amorphous matrix. These anatase crystallites can be seen to be smaller than 5 nm.

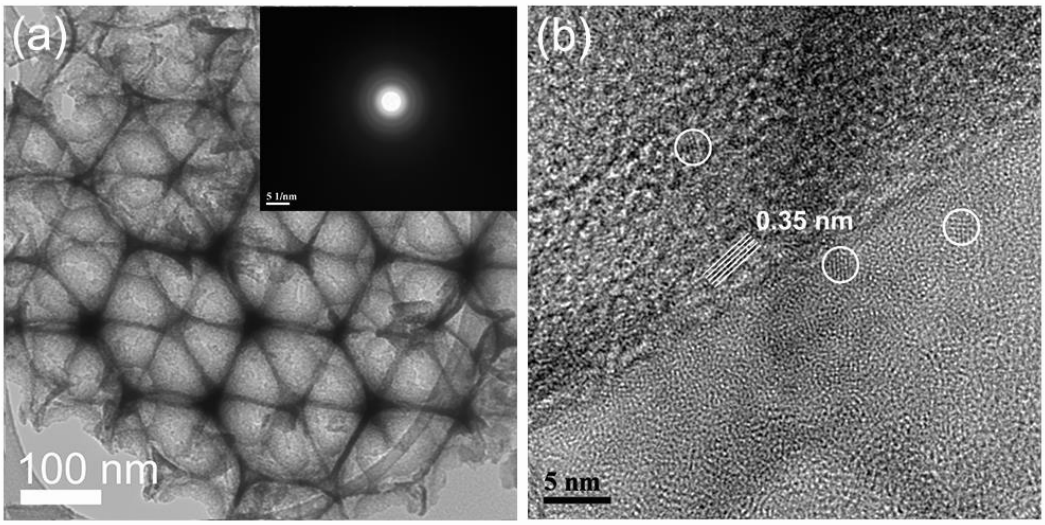

Figure 4-7. (a) TEM image of carbon-coated 3DOM structure (inset: corresponding SAED pattern); (b) HRTEM image of pore wall demonstrating the existence of nanocrystalline anatase in the pore wall of the 3DOM structure.

The presence and distribution of elements in 3T-C were first explored using SEM energy-dispersive X-ray spectroscopy (EDX) mapping (**Figure 4-8**). The sample was prepared on Al foil in order to remove any carbon contamination from carbon tape. The EDX maps confirmed that C, Ti, and O are present within the 3DOM structure. However, it was difficult to determine how carbon interacted with 3DOM TiO_2 and whether TiO_2 was being coated with carbon or mixed with carbon in the composite.

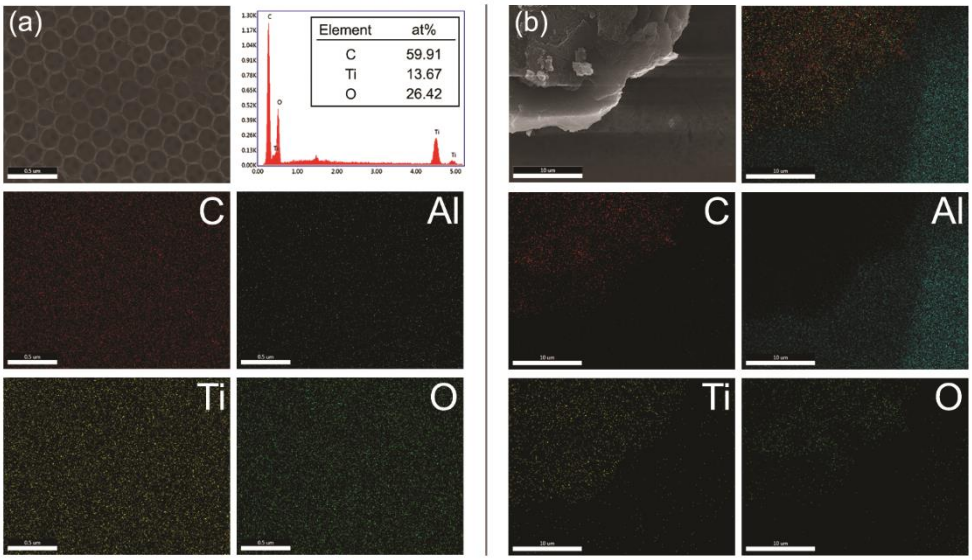

Figure 4-8. SEM EDX map of (a) carbon-coated 3DOM TiO_2 material, and (b) carbon-coated 3DOM TiO_2 on Al foil substrate.The mapping images show results for C, Al, Ti, and O. The lack of C from the Al foil substrate implies that all carbon in fact originates from the 3DOM material.

An EDX line map was also taken across the pore walls of the 3DOM material in order to further explore the composition of the 3DOM pore walls (**Figure 4-7c**). The line map clearly shows that while Ti and O make up the pore walls, C also be found in the pore walls following a similar distribution. This carbon layer can be attributed to the carbonization of polystyrene during the heat treatment process in Ar. Since TiO_2 is not oxidized directly in air before the carbonization step, carbonized polystyrene has the opportunity to infiltrate the TiO_2 precursor and limit crystallite growth. In fact, based on the estimated crystallite size from HRTEM (5 nm), heat treating the material in air to form pure 3DOM TiO_2 gives a higher average crystallite size of 7.6 nm (**Figure 4-10**).

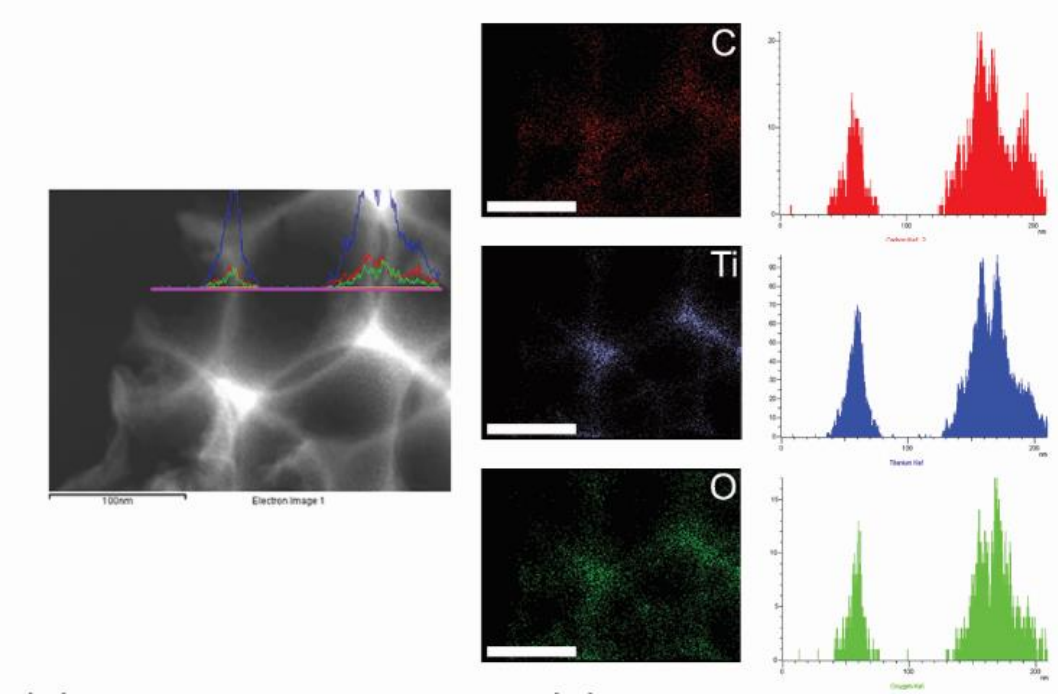

Figure 4-9. EDX map and line scan of pore walls showing distribution of C, Ti, and O. Scale bar = 100 nm.

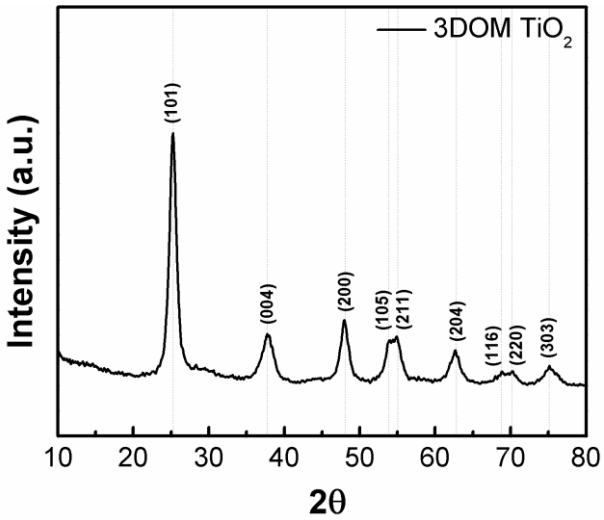

Figure 4-10. XRD spectra of 3DOM TiO_2 showing the characteristic peaks of anatase TiO_2.Using the Scherrer equation, the estimate crystallite size of this material is 7.6 nm.

XRD was conducted using Cu Kα radiation (1.54 Å) and is shown in **Figure 4-11a** below. Both 3T-CC and 3T-C-CC electrodes show similar spectra corresponding to anatase TiO_2 (JCPDS No. 21-1272) with characteristic peaks at 2θ = 25.6°, 38.1°, 48.3°, 54.1°, 55.0°, and 62.8°.[169] The weak intensity of the anatase peaks is due to the relatively low loading of TiO_2 compared to the carbon cloth. The broad peak centered at approximately 43.7° is due to the presence of carbon cloth while the other characteristic carbon peak at 26.2° is merged with the anatase peak at 25.6°.[170] As previously stated, the crystallite size of 3DOM TiO_2 was obtained by synthesizing the structure without carbon cloth. Using the Scherrer equation, the approximate crystallite size of the 3DOM TiO_2 is 7.6 nm based on the characteristic (101) peak (**Figure 4-10**). This is slightly larger than the crystallite size estimated for the carbon-coated 3DOM TiO_2. It has been shown that crystallite size and particle size match closely at particle sizes lower than 40 nm.[171] It has also been shown that complete lithiation is theoretically possible in crystallites at or below 7 nm. Therefore, the small particle size in the 3DOM TiO_2, along with its highly accessible surfaces can allow for good ion diffusion and lithiation within the macro-structure.

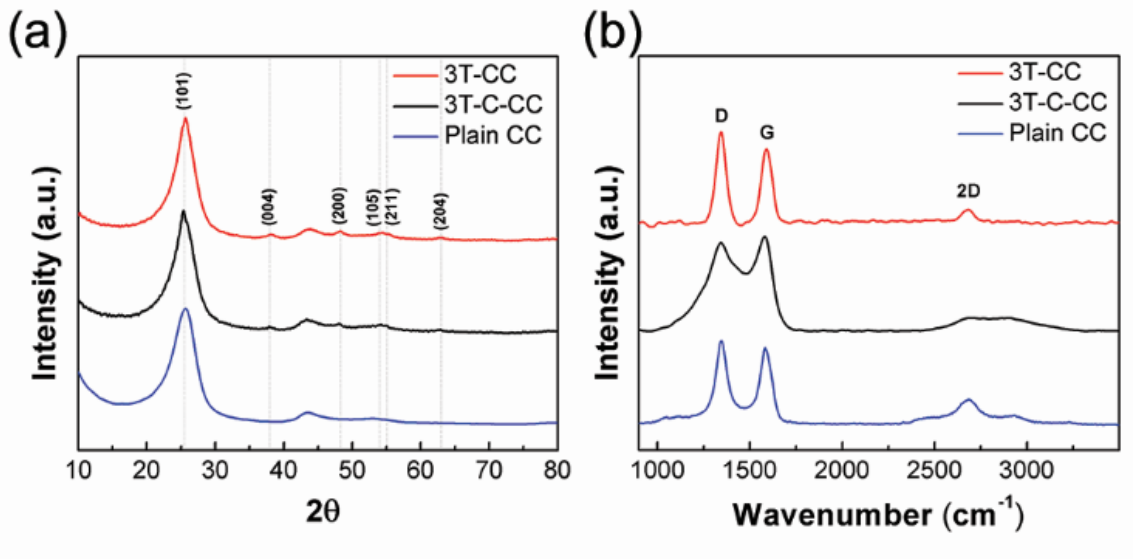

Figure 4-11. (a) XRD and (b) Raman spectra of 3T-CC, 3T-C-CC, and plain carbon cloth.

Raman spectroscopy was also used to characterize the graphitic nature of the carbon found in each electrode (**Figure 4-11a**). The spectrum for 3T-CC corresponds to the carbon cloth itself, and finds agreement in literature.[172] In this spectrum, the characteristic D band (1344 cm^{-1}) and G band (1590 cm^{-1}) can be seen, along with a small 2D peak at approximately 2679 cm^{-1}.[173] The spectrum for 3T-C-CC shows a distinct change in the relative intensities of the D and G bands, as well as a broadening of the 2D band. The difference in the Raman spectra has two main consequences. First, the change of D and G band peaks implies that the graphitic nature of the carbon in the electrode has changed due to the addition of carbonized polystyrene. Second, the decrease in the ratio of the D band to the G band (I_D/I_G) implies that the overall degree of disorder in the graphitic structure has decreased with the addition of carbonized polystyrene.

The true mass of the TiO_2 active material on the carbon cloth substrate was determined using TGA. A sample TGA results show that the mass of the 3T-CC electrode remains constant until approximately 600°C where the carbon cloth begins to burn away (**Figure A-2**). The TGA curve for 3T-C-CC shows an additional mass change region from 350°C to 475°C corresponding to the removal of amorphous carbon from the electrode. In the 3T-C-CC electrode, the amorphous carbon accounts for approximately 3.7% of the total electrode mass. The mass loadings of active material in the 3T-CC and 3T-C-CC electrodes are 6.8% and 6.0%, respectively. This is understandable, as the addition of amorphous carbon in 3T-C-CC will reduce the percent contribution of TiO_2.

The electrochemical behavior of the flexible electrodes was first investigated by cyclic voltammetry using CR2032 coin-type half-cells with Li foil as the counter electrode. **Figure 4-12a** shows the representative cyclic voltammetry (CV) curve of 3T-CC and 3T-C-CC flexible

electrodes cycled between 3.0 and 1.0 V vs. Li/Li+ at a scan rate of 50 mV s^{-1}. The redox peaks at 2.11 V and 1.69 V correspond to the characteristic lithium insertion and extraction of anatase TiO_2. Two addition redox pairs at 1.55 V/1.48 V and 1.66 V/1.54V have been reported to correspond to trace amounts of TiO_2-B.[174] However, because no main peaks corresponding to TiO_2-B[175] could be found in the XRD spectra, it is more likely that the peaks correspond to the S-peaks (surface peaks) which indicate the presence of amorphous titania in an organized crystalline composite.[168,176] Due to the surface nature of S-peak, they tend to have small voltage separation between redox couples. This interpretation is more consistent with the above HRTEM results.

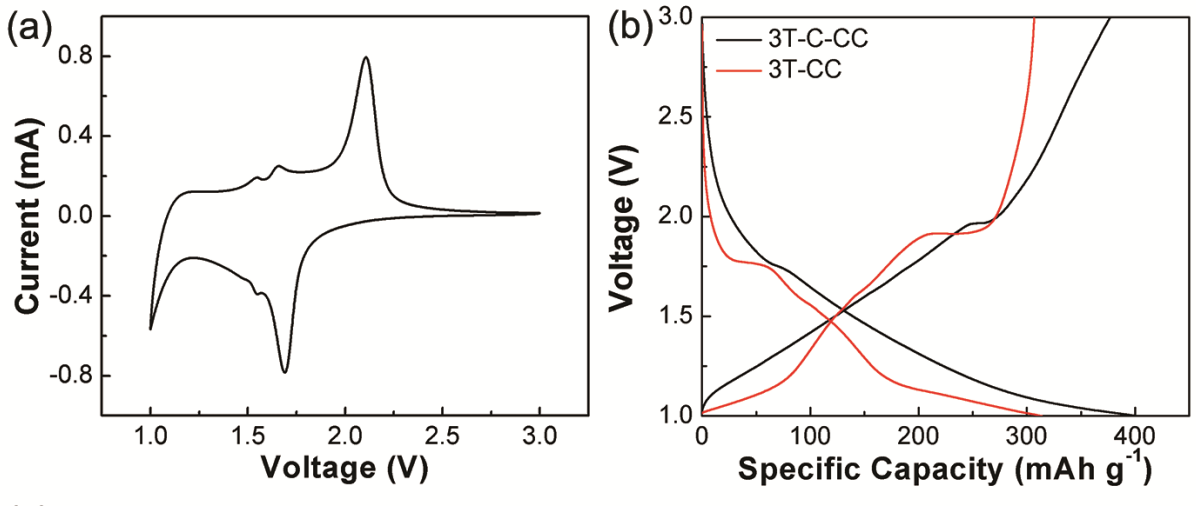

Figure 4-12. (a) Representative CV curve of 3DOM TiO_2 material vs. Li/Li^+; (b) initial charge-discharge curves for 3T-C-CC and 3T-CC electrodes.

The charge/discharge curves for both 3T-CC and 3T-C-CC at 50 mAh g^{-1} are shown in **Figure 4-12b**, and show agreement with the obtained CV curve. The plateaus at approximately 1.75 V and 1.90 V correspond to bulk lithiation and de-lithiation processes in TiO_2. It can been seen that the majority of the capacity in both electrodes is dominated by a sloped region which is attributed

to a surface-controlled lithium storage process.[177,178] This understandably corresponds to the highly porous structure of the 3DOM electrode with a highly accessible surface area.

In order to determine the rate performance of the 3T-CC and 3T-C-CC electrodes, each electrode was fabricated into a half-cell and cycled at various charge/discharge rates (**Figure 4-13**). For comparison, a carbon cloth electrode containing 25 nm anatase particles was fabricated and cycled under the same conditions. Starting at 50 mAh g^{-1}, each electrode is cycled at increasing current densities in order to determine their rate capability. It can be seen that at 50 mA g^{-1}, both 3DOM electrodes have a fairly high initial capacity (401 mAh g^{-1} for 3T-C-CC and 312 mAh g^{-1} for 3T-CC) while the TiO_2 NP electrode has a capacity of 213 mAh g^{-1}. When the current is increased to 2 A g^{-1}, the 3T-CC, 3T-C-CC, and TiO_2 NP electrodes has a stable specific capacities of 115 mAh g^{-1}, 174 mAh g^{-1}, and 68 mAh g^{-1}, respectively. The capacity of the 3T-C-CC electrode finally falls to 69 mAh g^{-1} at a current density of 12.5 A g^{-1}, or ~73.5C (using $C_{anatase}$ = 170 mAh g^{-1}).

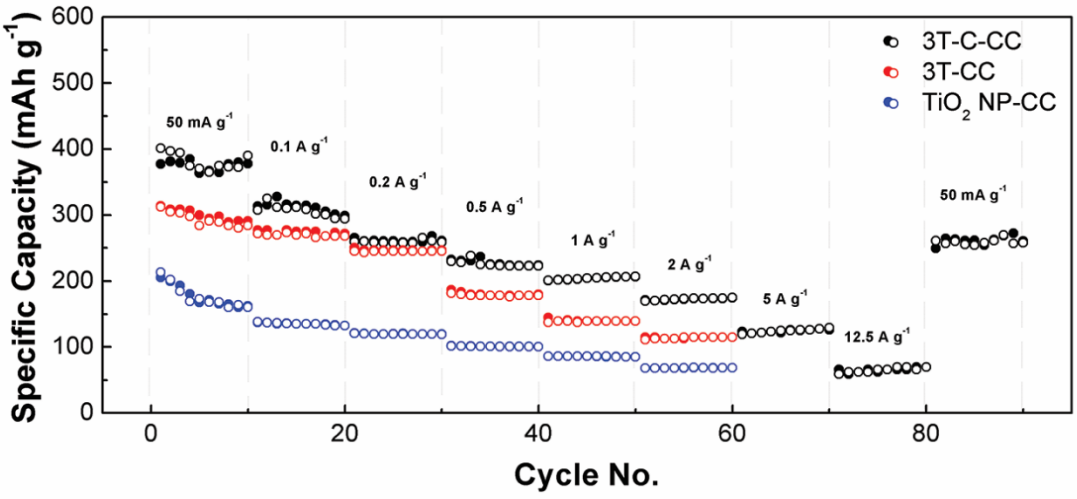

Figure 4-13. Rate performance of 3T-C-CC, 3T-CC, and TiO_2 NP-CC electrodes.

The cycling stability of the three electrodes was determined by cycling the electrode at 10C (1.7 A g^{-1}) for 1000 cycles (**Figure 4-14**). Based on the discharge capacity of the first and last cycles, the half-cell fabricated using the 3T-C-CC electrode has a capacity retention of 94.8% over 1000 cycles with a final capacity of 181 mAh g^{-1}. Over the same number of cycles, the 3T-CC and TiO_2 NP electrodes have a capacity retentions of 79.6% (111 mAh g^{-1}) and 93.7% (67 mAh g^{-1}), respectively. The large difference in stability between 3T-CC and TiO_2 NP-CC is likely due to additives (binder, conductive agent) mixed with the TiO_2 NPs in order to improve its conductivity and stability during cycling. From the cycling results, it is clear that the 3T-C-CC electrode provides the highest cycling stability and highest capacity at 10C. To the best of our knowledge, this half-cell performance is among the highest found in literature for a flexible, binder-free TiO_2-based electrode.[179-182]

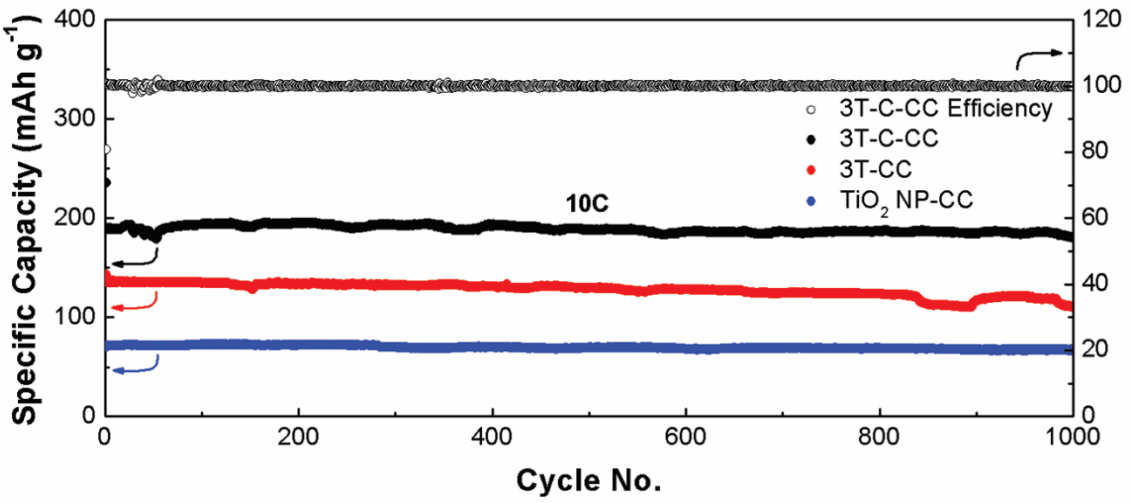

Figure 4-14. Long term cycling of 3T-C-CC, 3T-CC, and TiO_2 NP-CC electrodes at 1.7 A g^{-1} (10C) for 1000 cycles.

4.4 Conclusions

In summary, a facile method for synthesizing a flexible, binder-free 3DOM TiO_2 electrode has been shown for the first time. This configuration can act as a flexible, binder-free anode in Li-ion batteries with strong high-power performance. By heat treating the electrode in Ar, the polystyrene template can be used as a source for carbon coating. The resulting carbon-coated 3DOM TiO_2 electrode has superior high-rate performance, with a capacity of 174 mAh g^{-1} at a current density of 2 A g^{-1}. The electrode also shows highly stable performance (181 mAh g^{-1}) with a capacity retention of 94.8% over 1000 cycles at 10C (1.7 A g^{-1}). This performance is due to the ordered porous structure and thin pore walls of 3DOM TiO_2, which allow for high surface area contact with the electrolyte, and fast lithiation kinetics. This facile method can be easily expanded to other materials and substrates, and can have a vast range of applications in technologies such as supercapacitors, fuel cells, solar cells, and sensors.

5.0 Advanced Biowaste-Based Flexible Photocatalytic Fuel Cell as a Green Wearable Power Generator

---

Chapter 5 is based on published work by Lui et al. in the scientific journal *Advanced Materials Technologies*.

Lui, G.; Jiang, G.; Lenos, J.; Lin, E.; Fowler, M.; Yu, A.; Chen, Z., Advanced Biowaste-Based Flexible Photocatalytic Fuel Cell as a Green Wearable Power Generator. *Advanced Materials Technologies* **2017,** *2* (3).

See **Statement of Contributions** for a detailed summary of contributions from each co-author.

In this chapter, a wearable power generator is designed from a flexible, photocatalytic fuel cell using various biowaste sources (lactic acid, ethanol, methanol, urea, glycerol, and glucose) as fuel. The flexible photocatalytic fuel cell uses light irradiation and the decomposition of 'biowaste' to generate electrical power under both flat and bending (r = 3 cm) conditions. When employed as a sweat band, the flexible photocatalytic fuel cell generates a maximum power 4.0 mW cm^{-2} g^{-1} from human sweat. The wearable flexible photocatalytic fuel cell is able to overcome many of the disadvantages of wearable microbial and enzymatic cells while providing comparable if not superior power density.

5.1 Introduction

Wearable technologies are a quickly expanding market addressing the demand for flexible and wearable electronics, including smart clothing, smart devices, activity trackers, and even medical devices.[148,183-185] The majority of progress in this field has been in the design of flexible battery,[186,187] supercapacitor,[188,189] and photovoltaic[190,191] devices which can either store or convert energy in a wearable configuration. Several additional energy conversion methods have been used to harness energy directly from human body, including body heat,[192,193] mechanical movement,[194,195] and triboelectric charging.[196,197] However, little research has been performed on harnessing biowaste as a source of energy in a wearable power generation device.

A flexible photocatalytic fuel cell is one such concept that would be able to convert organic matter such as biowaste into electrical energy, effectively providing green, wearable power generation. flexible photocatalytic fuel cells consist of a photoelectrochemical cell using a photoelectrode as the anode and an organic fuel source as the electrolyte.[6] The design of the flexible photocatalytic fuel cell in green power generation affords several significant properties. First, photocatalysis is a light-activated advanced oxidation process that is able to photogenerate highly oxidative hydroxyl radicals that non-selectively decomposed organic material.[24] Consequently, virtually all organic matter can be used as fuel in a flexible photocatalytic fuel cell, including resilient biowaste that are not easily converted to CO_2 and H_2O.[198-200] Second, a photoelectrochemical configuration allows these highly favourable redox reactions to simultaneously generate an electrical current.[6] Third, photocatalysts are inert materials that are not consumed during oxidation, do not create secondary forms of pollution, and are naturally self-regenerating.[201,202] Therefore, photocatalysts are generally stable irrespective of their

environment and do not need to be replaced. These properties provide flexible photocatalytic fuel cells with a distinct advantage over renewable power generation technologies such as enzymatic and microbial fuel cells.[203-207] Enzymatic fuel cells (EFCs) are a class of fuel cell that uses enzymes to oxidize fuel instead of electrocatalysts. Because of this, EFCs require specific operating parameters, including temperature, mediators, and buffer solutions in order to function properly. In addition, EFCs require relatively expensive enzymes that are chemically specific and cannot necessarily oxidize any organic material. For these reasons, flexible photocatalytic fuel cells have the potential to provide a more comprehensive and resilient form of power generation.

We have developed for the first time a flexible photocatalytic fuel cell that can provide green, wearable, energy conversion and power generation. The inherent flexibility of a flexible photocatalytic fuel cell allows for ad hoc and non-standard solutions not accessible to the rigid configurations of conventional photocatalytic fuel cell devices, therefore greatly diversifying its potential application in real-world situations. These applications include: i) wearable technologies that generate power from biowaste; ii) wearable or flexible technologies that can be used as sensors; and, iii) flexible configurations for conventional waste water remediation and water reservoirs.

The multi-functional performance of a flexible photocatalytic fuel cell is achieved through the oxidation of an organic fuel at the photoanode (**Figure 5-1a**). When a photon strikes the photocatalyst through the transparent current collector, an electron-hole pair is created. In an n-type semiconductor, the electron moves to the current collector and the external circuit. The hole in turn moves to the electrode surface and initiates an oxidation reaction with an adsorbed

species, generating a free proton, H^+ (Equation 5-1). The proton diffuses to the cathode where it combines with O_2 and incoming electrons to form H_2O in a reduction reaction (Equation 5-2). In the absence of oxygen, H_2 gas can be formed in the reduction reaction instead (Equation 5-3).[126,132] Therefore, photocatalytic fuel cells are functionally related to conventional fuel cells, yet mechanistically distinct.[208,209] Relatively inexpensive photocatalysts are used in place of precious[210-212] and non-precious[213-215] metal electrocatalysts.

$$2R-H + 2h^+ \rightarrow 2R' + 2H^+ \quad (5\text{-}1)$$

$$2H^+ + \frac{1}{2}O_2 + 2e^- \rightarrow H_2O \quad (5\text{-}2)$$

$$2H^+ + 2e^- \rightarrow H_2 \quad (5\text{-}3)$$

In order to demonstrate flexibility, indium tin oxide-coated PET film (ITO/PET) was used as the photoanode current collector, Pt/C on carbon cloth was used as the cathode, and cellulose paper was used as the solid electrolyte membrane. The photoelectrochemical cell was sealed in a transparent plastic housing using a heat sealer. The configuration of the flexible photocatalytic fuel cell is illustrated in **Figure 5-1b**.

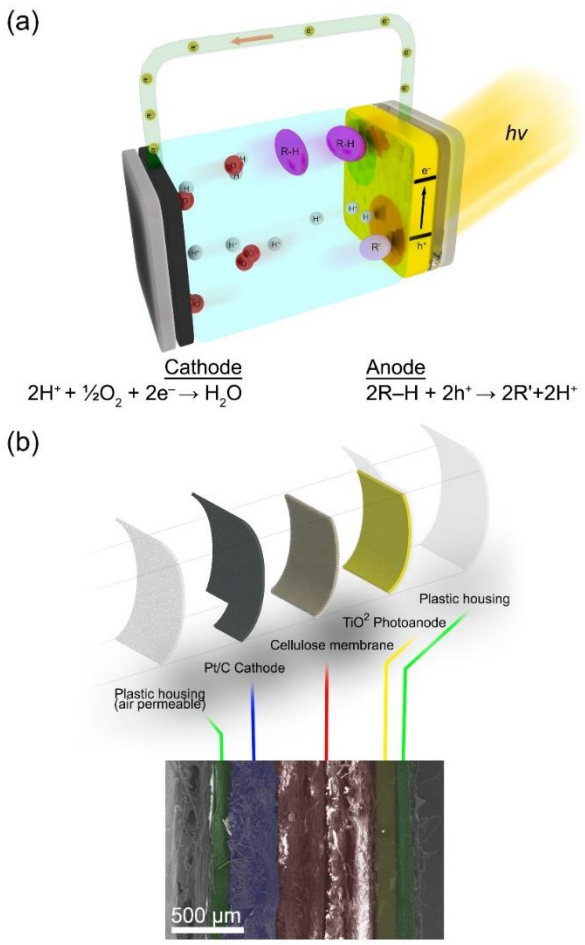

Figure 5-1. (a) Schematic outlining the basic operation of a photocatalytic fuel cell.(b) Configuration and components of the flexible photocatalytic fuel cell.

5.2 Experimental Methods

5.2.1 Materials

All chemicals were purchased from Sigma Aldrich and used as-received. Indium tin oxide coated polyethylene terephthalate (ITO/PET) was also purchased from Sigma Aldrich. Pt/C on carbon cloth was purchased from FuelCellEtc. All chemicals were used as received.

5.2.2 Flexible Photocatalytic Fuel Cell Fabrication and Assembly

The flexible photoanode was fabricated by creating a slurry containing 0.95 mL ethanol, 0.05 mL titanium tetraisopropoxide, and 100 mg P25 (Degussa, 21 nm particles). The slurry was sonicated for 10 min and then cast onto ITO/PET sheet (Sigma Aldrich, 60 Ω cm^{-2}). A doctor blade was used in order to control the thickness of the film. The prepared anode was then heat treated at 150°C for 1 h using a ramp rate of 10°C min^{-1}. The flexible photocatalytic fuel cell was assembled using the prepared photoanode and Pt/C on carbon cloth as the flexible cathode. Cellulose paper was used as the solid electrolyte membrane and separator. The combined electrodes were then pressed between two sheets of plastic sheets and sealed using a heat sealer.

The flow-chart corresponding to this procedure can be seen in **Figure 5-2**.

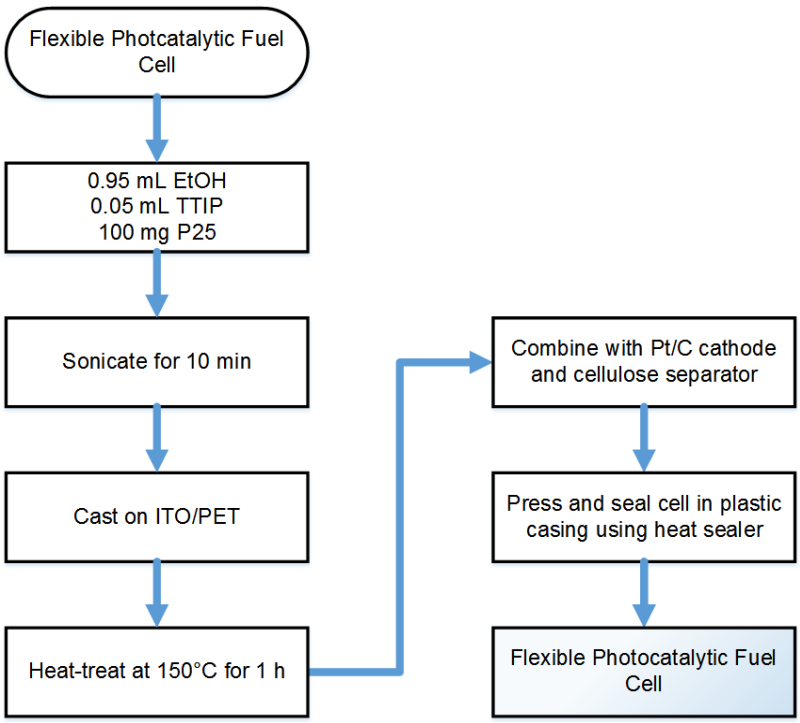

Figure 5-2. Flow-chart outlining the fabrication of a flexible photocatalytic fuel cell.

5.2.3 Characterization

A field-emission scanning electron microscope (FESEM, Zeiss ULTRA Plus) was used to determine the microstructure and cross-sectional composition of the photoanode. X-ray diffraction (XRD, Bruker AXS D8 Advance) was used to confirm the crystal phase of the photoanode material.

Photoelectrochemical characterization was performed using an electrochemical work station (Princeton Applied Research VersaSTAT MC) and a 1 W 365 nm LED (Digikey). Photocurrent measurements were performed without any applied bias or current. Polarization curves were determined using galvanodynamic measurements (100 μA s^{-1}). Nyquist plots were obtained using electrochemical impedance spectroscopy. A frequency ranging from 1 Hz to 1 MHz was applied, using an alternating signal of 100 mV. EIS data was modelled using ZSimpWin data analysis software.

In order to show the potential application in flexible, wearable technologies, the performance of the flexible photocatalytic fuel cell was determined using artificial sweat as a fuel. The flexible photocatalytic fuel cell was fabricated into a sweat band where the absorption of sweat under light irradiation would generate power. The artificial sweat solution is based on median concentrations of major constituents outlined by Harvey et al., specifically: 0.031 M NaCl, 0.014 M lactic acid, 0.01 M urea, and 1.7×10^{-4} M glucose.[216] The power output of the sweatband is measured across a 2.7 kΩ load, and the voltage and current is measured using digital multimeters (Agilent 34411A and 34401A).

In order to show potential application in waste water treatment, the photocatalytic performance of the flexible photocatalytic fuel cell was determined through the photodegradation of

methylene blue (MB) under solar simulated light (ABET Technologies LS 10500, 100 mW cm^{-2}). The flexible photocatalytic fuel cell was placed inside a beaker (r = 3 cm) containing 10 μM MB under stirring. The solution was allowed to stir in the dark for 60 min in order for the flexible photocatalytic fuel cell to reach adsorption-desorption equilibrium. The flexible photocatalytic fuel cell was then irradiated with solar simulated light for 5 hours, with samples taken every hour. A UV-Vis spectrophotometer (Fischer Scientific, GENESYS 10S) was used to measure the absorbance of the solution over time.

5.3. Results and Discussion

The photoanode was prepared using commercial TiO_2 nanoparticles (P25). A slurry was made by mixing P25, ethanol, and titanium tetraisopropoxide and sonicating the mixture for 60 minutes. The slurry was then cast onto an ITO/PET film using a doctor blade to control the loading and thickness of the catalyst film. The average TiO_2 loading on the photoanode was found to be 0.92 mg cm^{-2}.

Scanning electron microscopy (SEM) was used to characterize the topology of TiO_2 photoanode (**Figure 5-3**). The surface is uniform on a macroscopic level, while high magnification images reveal that the film consists of nanoparticles approximately 20 nm in diameter. This is consistent with the size of nanoparticles used to make the electrode. A cross-sectional SEM image was also taken of the photoanode. The photocatalyst layer was found to be ~19.1 μm thick, while the PET layer is roughly 100 μm thick. Energy-dispersive X-ray spectroscopy (EDX) mapping was also used to confirm this configuration (**Figure B-1**). Lastly, X-ray diffraction was used to confirm that the nanocrystalline TiO_2 consisted of both anatase and rutile phases characteristic of P25 (**Figure B-2**).[217]

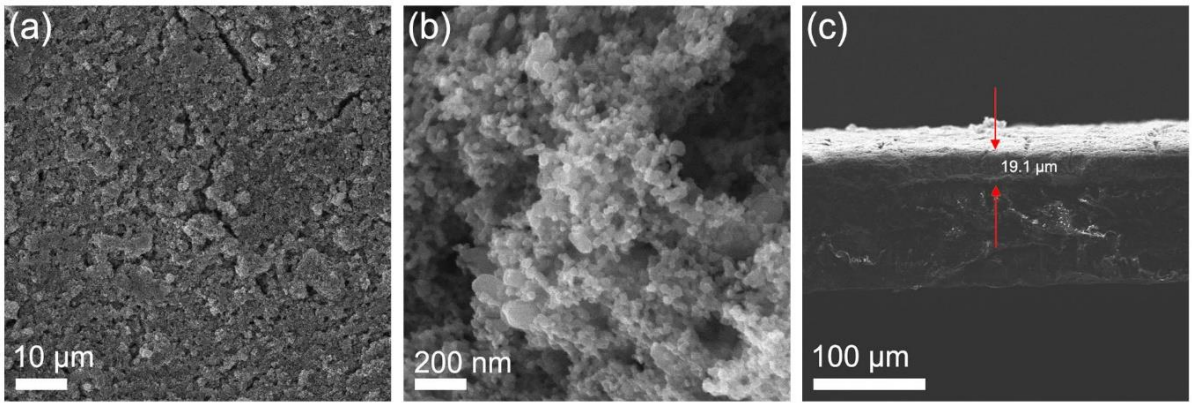

Figure 5-3. SEM images of the photoanode. (a) TiO_2 film at low magnification and (b) high magnification.(c) Cross-sectional SEM image showing TiO_2 layer on ITO/PET substrate.

In order to evaluate the potential ability of the flexible photocatalytic fuel cell to generate power from biowaste, various organic fuels were tested. Electrolyte solutions were created using 1 M solutions of lactic acid, ethanol, methanol, glycerol, urea, and glucose in de-ioinized water. No other components were added to the electrolyte. The photoelectrochemical properties of the flexible photocatalytic fuel cells using various fuels were tested using a 1 W 365 nm LED. The irradiance at the surface of the flexible photocatalytic fuel cell was found to be 217 mW cm^{-2} at a distance of 2.1 cm. The photocurrent response of the flexible photocatalytic fuel cell is shown in **Figure 5-4a and 5-2b** where the light source is turned on and off at intervals of 30 s. The response of the flexible photocatalytic fuel cell to light irradiation is almost instant, while the relaxation varies depending on the fuel used. Specifically, the relaxation of glucose and glycerol fuels exceeds that of the other fuels. This is likely due to the larger size of these molecules with more extensive degradation pathways. This increases the chance for current doubling which can prolong current generation even after the light source has been removed.

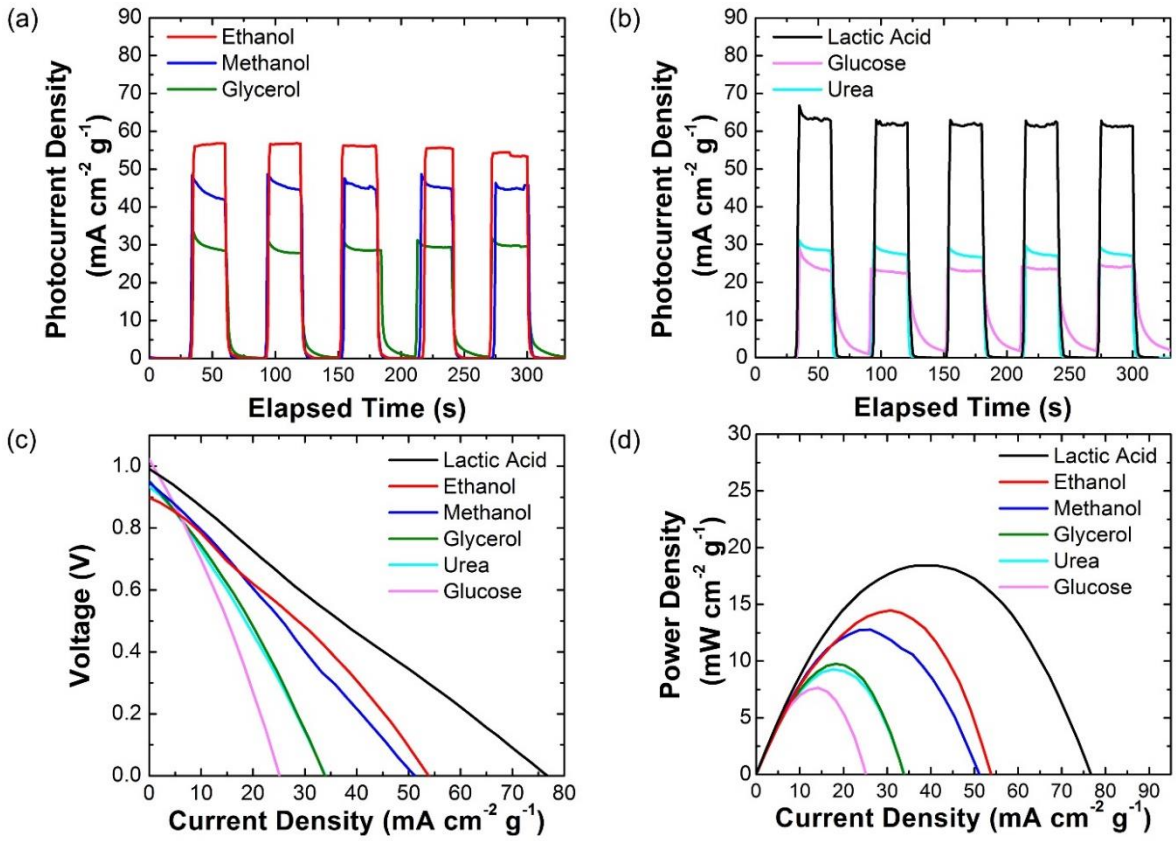

Figure 5-4. Photocurrent responses of (a) alcohols and (b) organic matter found in human sweat; (c) polarization curves, and (d) corresponding power curves of the flexible photocatalytic fuel cell using different fuels.

The photocurrent response of the fuels generally exhibit an anodic or mixed (anodic-cathodic) current under light irradiation. In fact, apart from ethanol, all other fuels exhibit initial mixed current behaviour. This is due to the sudden, initial generation of electron-hole pairs which push holes toward the photocatalyst surface and electrons toward the bulk.

Potential reactions at the anode using the fuel tested in this work are given in **Equations 5-1 to 5-6.** The oxidation of the organic compounds used in this work are heavily studied and can be found in literature. The oxidation of organic compounds typically lead to the formation of alcohols, aldehydes, acids, CO_2 and H_2O. Therefore:

For alcohols:

$$R - CH_2 - OH + 2h^+ \rightarrow R - CH = O + 2H^+ \quad (5\text{-}1)$$

Where R = H (methanol), CH_3 (ethanol), $C_3H_7O_2$ (glycerol).

For glycerol:

$$C_3H_8O_3 + 2h^+ \rightarrow C_3H_6O_3 + 2H^+ \quad (5\text{-}1)$$

For lactate:[218]

$$CH_3CH(OH)COOH + \ 2h^+ \rightarrow CH_3CHO + CO_2 + 2H^+ \quad (5\text{-}3)$$

For urea:[219,220]

$$CO(NH_2)_2 + H_2O + 6h^+ \rightarrow N_2 + CO_2 + 6H^+ \quad (5\text{-}4)$$

For glucose (to D-Gluconic acid or D-Arabinose[222]):

$$C_6H_{12}O_6 + H_2O + 2h^+ \rightarrow C_6H_{12}O_7 + 2H^+ \quad (5\text{-}5)$$

$$C_6H_{12}O_6 + H_2O + 2h^+ \rightarrow C_5H_{10}O_5 + HCOOH + 2H^+ \quad (5\text{-}6)$$

After this initial photogeneration, electrons begin to recombine with the accumulated holes until an equilibrium is reached.[223-226] This equilibrium current depends on the rates of fuel oxidation (anodic) and recombination ('cathodic'). Therefore, the lack of observed mixed current behaviour in the ethanol flexible photocatalytic fuel cell suggests that the relative rate of ethanol oxidation is much greater than the rate recombination.[223] This could be explained by the more reducing potential of the ethoxy radical (-1.18 V) compared to the methoxy radical (-0.98 V). In terms of photocurrent response, lactic acid fuel provides the highest current (61.4 mA cm^{-2} g^{-1}), followed by ethanol (56.7 mA cm^{-2} g^{-1}), methanol (42.0 mA cm^{-2} g^{-1}), glycerol (28.5 mA cm^{-2} g^{-1}), urea (28.4 mA cm^{-2} g^{-1}), and glucose (22.7 mA cm^{-2} g^{-1}). The large current density of lactic

acid is due to its acidity, which greatly increases the overall ionic conductivity of the electrolyte by providing additional H^+ ions. This improvement to the electrolyte is significant since no other components (besides water) are added to the electrolyte solution to improve its conductivity. Understandably, the simple alcohols provide high current densities due to their facile oxidation kinetics, while more complex molecules (such as glucose and glycerol) have lower current densities due to slower kinetics and diffusion.[128,227] The long-term operational stability was demonstrated using 1 M lactic acid and is shown in **Figure 5-5** where no additional fuel was added after initial injection. The flexible photocatalytic fuel cell was operated over a period of one hour with a relatively stable photocurrent density output. This result demonstrates the potential for power generation using a flexible photocatalytic fuel cell, provided that fuel is available for consumption.

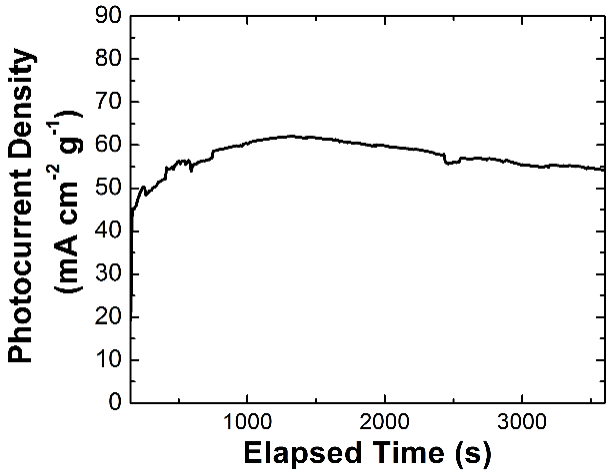

Figure 5-5. Long-term operational stability of a flexible photocatalytic fuel cell over 1 h using 1 M lactic acid as fuel.

Polarization curves of the flexible photocatalytic fuel cells were also obtained (**Figure 5-4c**) and show a similar trend to the photocurrent response curves. The polarization curves show a distinct

lack of activation polarization found in conventional fuel cells and appear to be dominated by concentration polarization. This is a common phenomenon in photocatalytic electrochemical cells is likely due to the excitation of charge carriers in photocatalytic materials.[126,127,130,132,228-230] Because current is induced through the anode material as opposed to the external circuit, it is possible that activation polarization is intrinsically overcome by the photogeneration of charge carriers in a catalyst with a sufficiently large redox potential. All curves exhibit a similar open-circuit voltage (V_{OC}) with values ranging from 0.90 to 1.03 V due to the similarity of their oxidation potentials. The short-circuit current densities (J_{SC}, the current density at 0 V) follow the same trend as the photocurrent densities, with lactic acid exhibiting the highest J_{SC} value (76.8 mA cm^{-2} g^{-1}) followed by ethanol (53.8 mA cm^{-2} g^{-1}), methanol (51 mA cm^{-2} g^{-1}), glycerol (33.9 mA cm^{-2} g^{-1}), urea (33.8 mA cm^{-2} g^{-1}), and glucose (25.0 mA cm^{-2} g^{-1}). Power curves based on the same data (**Figure 5-4d**) show that the maximum power achievable for cells using lactic acid, ethanol, methanol, glycerol, urea, and glucose are 18.4 mW cm^{-2} g^{-1}, 14.5 mW cm^{-2} g^{-1}, 12.8 mW cm^{-2} g^{-1}, 9.7 mW cm^{-2} g^{-1}, 9.3 mW cm^{-2} g^{-1}, and 5.1 mW cm^{-2} g^{-1}, respectively. This data is summarized in **Table 5-1**. Based on the maximum power output of the flexible photocatalytic fuel cell using each biofuel, calculated efficiency can be obtained and compared to similar technologies. Results showed that the theoretical first-law (coloumbic) efficiencies of the biofuels were within the range of 40% to 50%. When compared to competing technologies such as the microbial fuel cell, the flexible photocatalytic fuel cell provides comparable performance.[231] Similarly, when compared to fuel cells at appropriate operating voltages, the flexible photocatalytic fuel cell also provides comparable efficiencies.[232]

Table 5-1: Photoelectrochemical results of flexible photocatalytic fuel cell using various fuels.

Fuel	I_{ph} (mA cm^{-2} g^{-1})	J_{SC} (mA cm^{-2} g^{-1})	V_{OC} (V)	P_{max} (mW cm^{-2} g^{-1})	η (%)
Lactic Acid	61.4	76.8	0.990	18.4	41
Ethanol	56.7	53.8	0.899	14.5	42
Methanol	42.0	51.0	0.955	12.8	39
Glycerol	28.5	33.9	0.948	9.7	50
Urea	28.4	33.8	0.940	9.3	48
Glucose	22.7	25.0	1.033	5.1	43

In order to determine the potential of the photocatalytic fuel cell as a flexible device, the performance of the flexible photocatalytic fuel cell was obtained under bending. A comparison was made between the flat and bending (radius of curvature = 3 cm) performance of a flexible photocatalytic fuel cell using glycerol fuel (**Figure 5-6**). Optical images in **Figure 5-6a** convey the functionality of a glycerol flexible photocatalytic fuel cell by generating an open-circuit voltage of 958 mV under irradiation in a bending configuration. This value is functionally identical to that under flat conditions (**Figure 5-4c**).

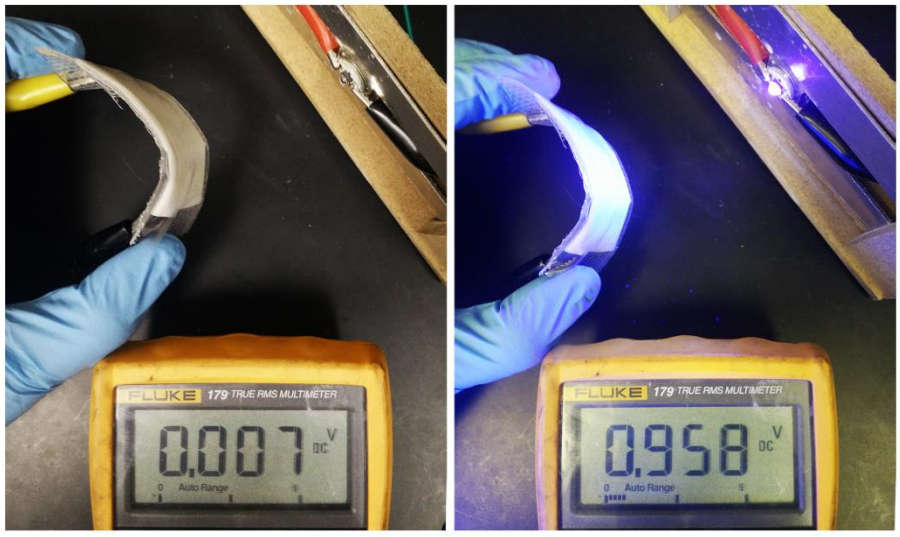

Figure 5-6. Optical images showing open circuit voltage of flexible photocatalytic fuel cell with and without light irradiation.

The photocurrent response (**Figure 5-7a**) of the device under bending (26.2 mA cm^{-2} g^{-1}) is marginally lower than in a flat configuration (28.5 mA cm^{-2} g^{-1}). It can be seen that bending the flexible photocatalytic fuel cell introduces a small amount of noise during irradiation. This noise is due to the introduction of non-uniform contact between the electrodes and the cellulose membrane under bending. These irregularities cause fluctuations in the overall current as points of contact are lost or gained under bending. The polarization curve of the flexible photocatalytic fuel cell under bending is in agreement with the average of the photocurrent response results (**Figure 5-7b**). Under bending, the flexible photocatalytic fuel cell has a short-circuit current density of 25 mA cm^{-2} g^{-1} and a maximum power density of 6.6 mW cm^{-2} g^{-1}.

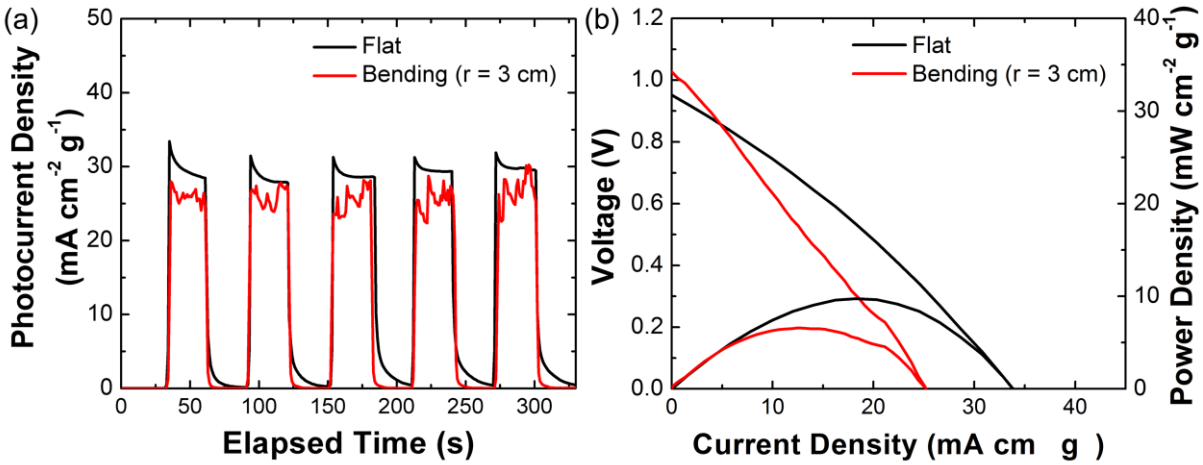

Figure 5-7. (b) Photocurrent response and (c) polarization and power curves of a glycerol-powered flexible photocatalytic fuel cellunder flat and bending (radius of curvature = 3 cm) conditions.

Lastly, electrochemical impedance spectroscopy (EIS) was used to further investigate the electronic properties of the flexible photocatalytic fuel cell under light irradiation and bending (**Figure 5-8**). In the absence of light irradiation, the cells exhibit fairly linear (corresponding to Warburg impedance, Z_W) behaviour with a minimal charge transfer component. For this reason,

the EIS data was modelled using a simple Randles circuit that includes a Warburg diffusion element (**Figure B-3**). It is apparent that under bending the angle of the Warburg diffusion region increases (with respect to the x-axis). This increased angle corresponds to a smaller impedance when projected onto the real axis, and a decrease in the overall ionic resistance of the system.[233] Under both flat and bending conditions, the series resistance (R_S) is 315.3 Ω and 316.4 Ω, respectively.

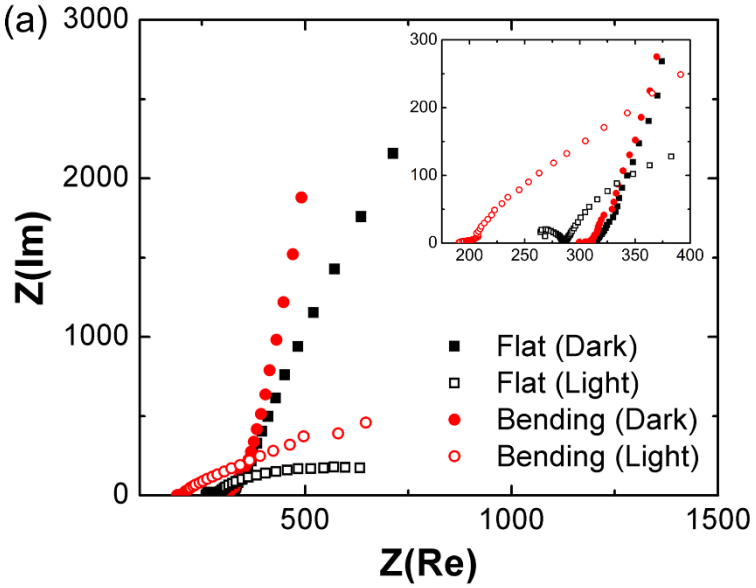

Figure 5-8. EIS plots of glycerol-powered flexible photocatalytic fuel cell under flat and bending (radius of curvature = 3 cm) conditions.Inset: high-frequency region of the EIS curves.

Once the device is exposed to light irradiation, the EIS curves undergo change. First, it appears that charge-transfer elements are introduced to the system (**Figure B-3b**). This is indicated by the introduction of two charge-transfer semi-circles. The first semi-circle (R_{ct1}) can be assigned to the charge-transfer resistance between TiO_2 particles on the photoanode, while the second semi-circle (R_{ct2}) can be assigned to the TiO_2-electrolyte charge-transfer resistance.[234] This is

explained by the fact that light irradiation introduces photo-generated electron-hole pairs which undergo charge-transfer and redox reactions with the fuel present in the electrolyte. Without light irradiation, there is no charge carrier generation and therefore no activated charge-transfer. A drop also occurs in R_S (from 315.3 Ω to 257.2 Ω), indicating an increase in conductivity of the overall system. Under bending, the series resistance decreases even further due to the improved contact between the components at the point of bending. In addition, R_{ct1} and R_{ct2} decrease from 26.5 Ω and 200.9 Ω to 0.175 Ω and 13.5 Ω, respectively. This reduced resistance indicates an overall improvement in charge transfer in the photoanode under bending. All calculated values are tabulated and can be found in **Table S2**. Similar phenomena is observed with the other fuels tested in this study (**Figure S5**). These results demonstrate that various types of organic waste can in fact be used as fuel to generate power in a flexible photocatalytic fuel cell.

The flexible photocatalytic fuel cell was fabricated into a sweatband in order to evaluate its ability to generate power from human sweat. Artificial sweat solution was created using median concentrations of major constituents outlined by Harvey et al., specifically: 0.031 M NaCl, 0.014 M lactic acid, 0.01 M urea, and 1.7×10^{-4} M glucose.[216] Using a 1 W 365 nm LED, the photoelectrochemical performance of a flexible photocatalytic fuel cell in a flat configuration using this artificial sweat as fuel is shown in **Figure 5-9a** and **5-4b**. Despite the low concentrations of organic material (lactic acid, urea, and glucose), the initial photocurrent response of the artificial sweat flexible photocatalytic fuel cell shows comparable values to those found in **Figure 5-4**. The photocurrent appears to decrease immediately after the initial current spike when light irradiation is provided. This is explained by the lower concentrations of fuel and subsequent low mass transfer of reactants to the anode surface. The polarization and power curves of the artificial sweat flexible photocatalytic fuel cell (**Figure 5-9b**) show that the device

has an open circuit voltage of 0.9 V, a short circuit density of 17.3 mA cm^{-2} g^{-1}, and a maximum power density of 4.0 mW cm^{-2} g^{-1}. When compared to current enzymatic biofuel cells using artificial sweat as fuel, the flexible photocatalytic fuel cell can provide higher or comparable power densities.[204-206] This performance is also accomplished without the use of buffer solutions, electrochemical mediators, or expensive and sensitive enzymes. Working from these baseline results, the flexible photocatalytic fuel cell was evaluated as a sweatband by combining four cells in series (**Figure 5-9c**). Using artificial sweat as the fuel, the sweatband was illuminated by the LED at a distance of 6 inches (corresponding to 3 mW cm^{-2} UV light) and the power output was measured across a 2.7 kΩ resistor. As shown in **Figure 5-9d**, under light irradiation the flexible sweatband has a steady output of 0.35 mA at 0.94 V (0.33 mW with a specific power density of 1.6 mW cm^{-2} g^{-1}). These results demonstrate the potential application of flexible photocatalytic fuel cells in generating electrical power from fuels such as human sweat.

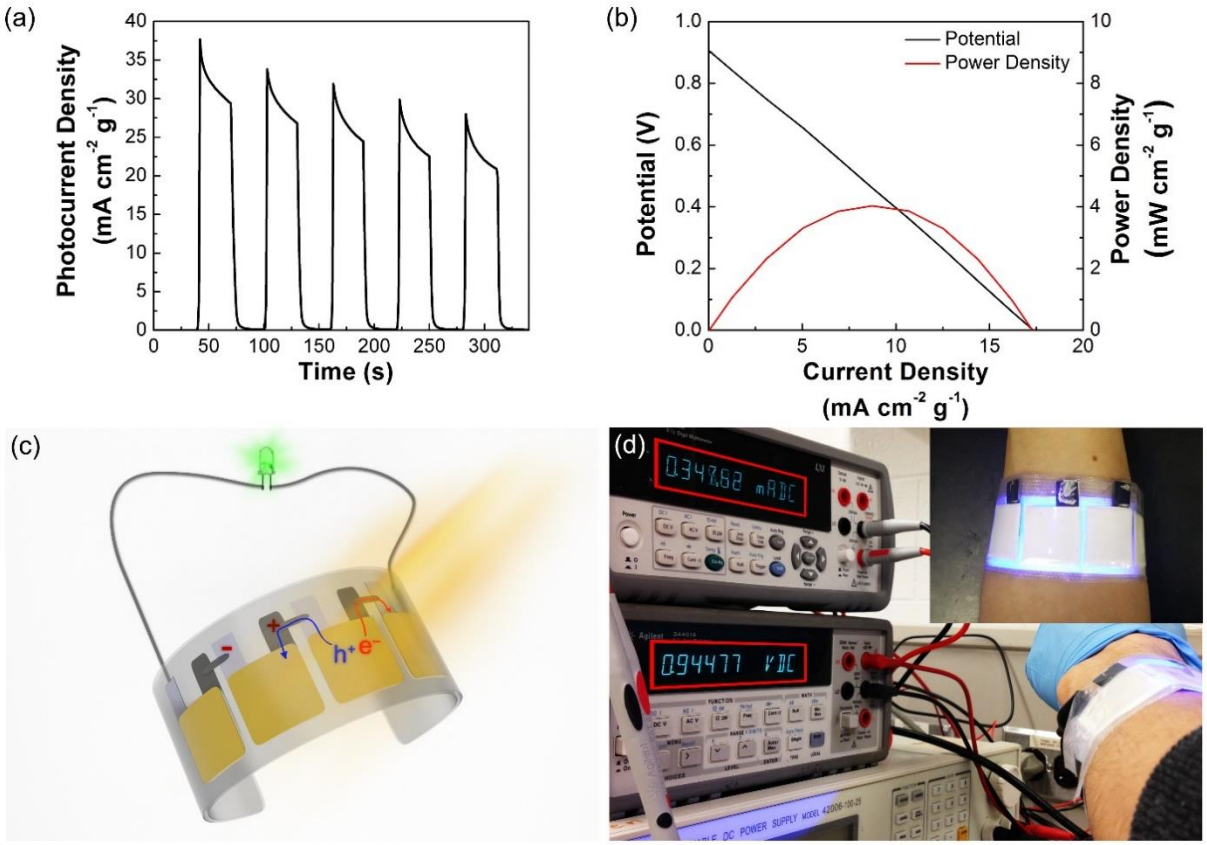

Figure 5-9. (a) Photocurrent response and (b) polarization and power curves of flexible photocatalytic fuel cell using artificial sweat as fuel.(c) Diagram of flexible photocatalytic fuel cell-based sweat band with four flexible photocatalytic fuel cells in series. (d) Optical images of flexible photocatalytic fuel cell-based sweat band in operation, generating 0.94 V and 0.35 mA (0.328 mW) across a 2.7 kΩ resistor. Inset: a top-view of the sweat band.

In order to explore additional potential applications for a flexible photocatalytic fuel cell, the fabricated flexible photocatalytic fuel cell was used as a flexible device in the photodegradation of organic waste. Methylene blue (MB) is a textile effluent that was used as the target organic compound for its wide use in literature and observable change in color during degradation. Methylene blue is often used as an electrochemical mediator in microbial fuel cells with concentrations up to 1 mM.[235,236] An MB concentration of 10 μM was used, and AM 1.5G solar simulated light (100 mW cm^{-2}) was used as the illumination source. **Figure 5-10a** shows a typical

I-V curve for the methylene blue flexible photocatalytic fuel cell. The I-V characteristics are lower when compared to the tested organic compounds due to large, aromatic structure of methylene blue. The flexible photocatalytic fuel cell also provides comparable energy output to microbial cells in the decomposition of other dyes.[237,238] **Figure 5-10b** shows the photocurrent response of the flexible photocatalytic fuel cell during 3 h of illumination. During the first 15 min, the observed increase in photocurrent (1.53 mA cm^{-2} g^{-1}) is due to the activation of the photoanode under anodic photocurrent. The relatively low photocurrent response of MB compared to the other biofuels is due to the greater complexity of the conjugated molecule, making it more difficult to decompose. After this initial increase, the photocurrent steadily decreases as the MB fuel is used up. At 300 min, the light source is turned off and the photocurrent immediately drops to 0 mA cm^{-2} g^{-1}.

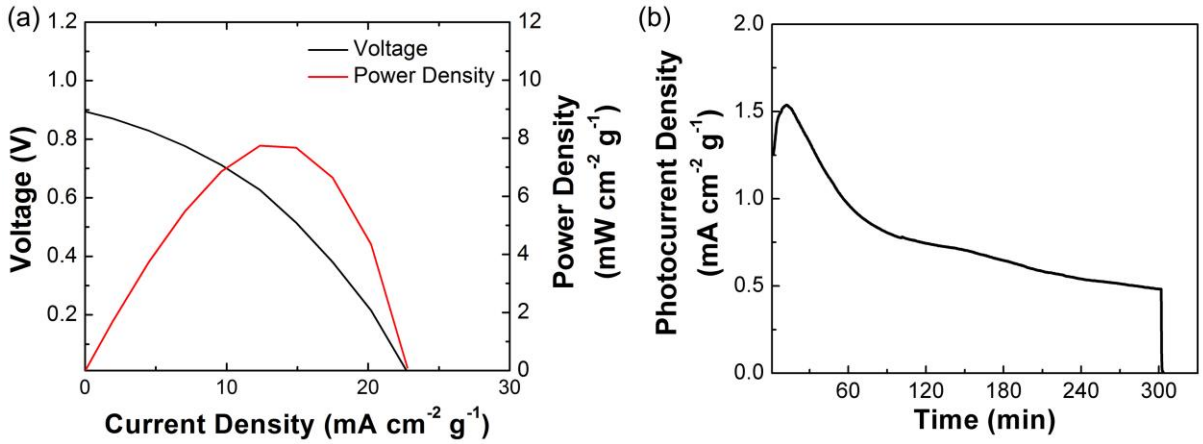

Figure 5-10. (a) I-V of flexible photocatalytic fuel cell using 10 μM methylene blue.(b) Photocurrent response of flexible photocatalytic fuel cell during methylene blue degradation under AM 1.5G solar simulated light.

Figure 5-11a shows the measured absorbance curves of MB throughout the photocatalytic reaction. The characteristic peak of MB (664 nm) is shown to be completely removed by 300 min, indicating the complete removal of MB. The reaction rate of the flexible photocatalytic fuel

cell device can be estimated using a pseudo first-order reaction rate, $kt = -ln(C/C_0)$. The reaction rate of the flexible photocatalytic fuel cell was found to be 0.0139 min^{-1} (**Figure 5-11b**).

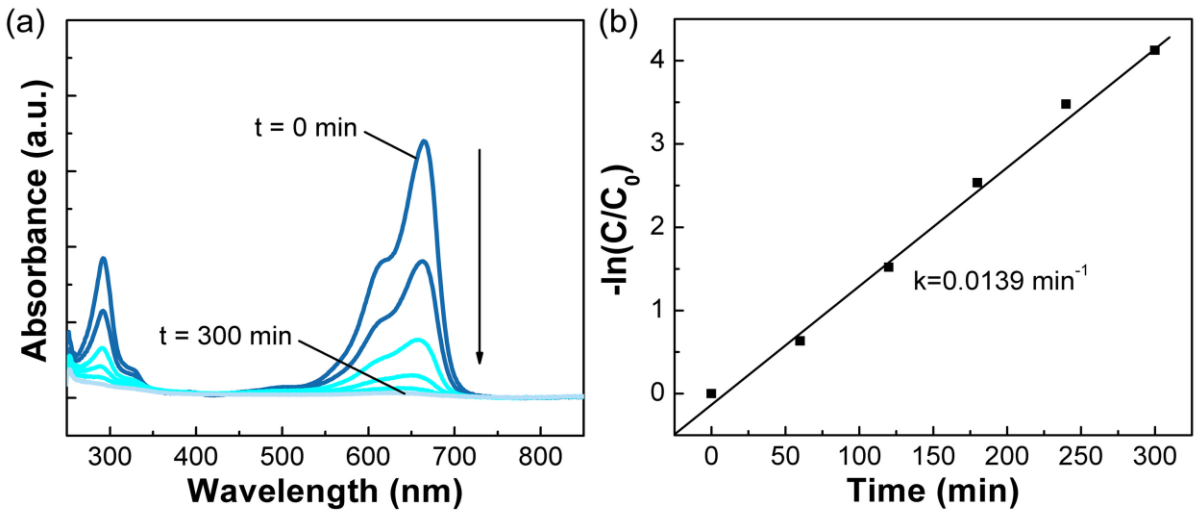

Figure 5-11. (a) Absorbance spectra of methylene blue taken over 300 min of the reaction.(b) Pseudo-first order reaction rate estimation from UV-Vis data.

Figure 5-12 shows optical images of the MB solution before and after light illumination, with and without using a flexible photocatalytic fuel cell. The flexible photocatalytic fuel cell is fixed to the curvature of the beaker during reaction. It is clearly seen that even after 3 h of reaction, the flexible photocatalytic fuel cell can remove virtually all traces of MB while simultaneously providing photocurrent. Without the flexible photocatalytic fuel cell, no current is generated and methylene blue remains in solution after 3 h. It should be noted that even in the absence of photocatalysis, methylene blue can still be removed through photolysis at slower reaction rates (with a measured reaction rate of approximately 0.009 min^{-1}), leading to the small change in the colour of the solution.

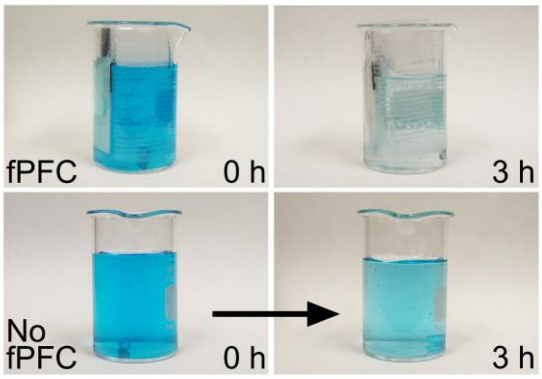

Figure 5-12. Optical images comparing the visible degradation of methylene blue dye with and without the use of the flexible photocatalytic fuel cell.A methylene blue concentration of 10 μM was used for this experiment.

When comparing these results to other technologies and devices found in literature, the flexible photocatalytic fuel cell fairly relatively well (**Table 5-2**). When compared to enzymatic fuel cells used to produce electrical power from human sweat and compounds found in sweat (lactate), the flexible photocatalytic fuel cell provides an acceptable output. When compared to microbial fuel cells that produce electrical power from dye molecules, the flexible photocatalytic fuel cell provides a superior power output.

Table 5-2: Comparison of flexible photocatalytic fuel cell performance with competing technologies in literature.

Technology		Fuel	Pmax (mW cm^{-2})
Enzymatic fuel cell	Falk et al.[204]	Human sweat	0.00026
Enzymatic fuel cell	Jia et al.[206]	14 mM lactate	0.034
Enzymatic fuel cell	Jia et al.[205]	15 mM lactate	0.100
Flexible photocatalytic fuel cell		*Artificial sweat (14 mM lactate)*	*0.032*
Microbial fuel cell	Han et al.[239]	50 μM methylene blue	0.003656
Microbial fuel cell	Fernando et al.[237]	0.6 mM acid orange-7	0.00519
Microbial fuel cell	Li et al.[238]	144 mM congo red	0.04
Flexible photocatalytic fuel cell		*10 μM methylene blue*	*0.062*

Based on these results, the flexible photocatalytic fuel cell maybe be applied to various waste sources as long as there exists a suitable light source in order to activate photocatalysis. Because photocatalysts are not limited to specific electrolyte and ambient conditions, they can potentially be deployed in various, potentially uncontrolled environments such as water reservoirs, tailing ponds, and waste water treatment facilities.

5.4 Conclusions

In summary, a flexible photocatalytic fuel cell was fabricated that demonstrates the feasibility of a light-powered, biowaste-based wearable power generator. This flexible photocatalytic fuel cell was shown to produce power using various biowaste fuels (lactic acid, ethanol, methanol, urea, glycerol, and glucose) and even under bending conditions (r = 3 cm). The photoelectrochemical performance of these cells was determined and analyzed using photocurrent measurements, polarization curves, and electrochemical impedance spectroscopy. These measurements shed light on the operation and intrinsic differences between light/dark and flat/bending regimes of a flexible photocatalytic fuel cell. Potential applications for the flexible photocatalytic fuel cell were explored by using the flexible device as a wearable power generation device using human sweat as a fuel source. The flexible photocatalytic fuel cell was also employed as a flexible device for in the degradation of organic waste in water. Even in flexible configurations, flexible photocatalytic fuel cells are able to outperform or match the performance of microbial and enzymatic biofuel cells in literature. At the same time, the flexible photocatalytic fuel cell can perform non-selective oxidation of organic species and is self-regenerating. These results demonstrate the potential application of flexible photocatalytic fuel cells in various energy production and waste water remediation technologies as a renewable, green technology.

6.0 A High Performance Waste water-Fed Flow-Photocatalytic Fuel Cell

---

Chapter 6 is based on submitted work by Lui et al. to the scientific journal *Journal of Power Sources*.

Lui, G.; Jiang, G.; Fowler, M.; Yu, A.; Chen, Z., A High Performance Waste water-Fed Flow-Photocatalytic Fuel Cell. (submitted to *Journal of Power Sources*).

See **Statement of Contributions** for a detailed summary of contributions from each co-author.

Ever since its properties were discovered in the 1970s, the photocatalyst has been used to perform light-activated, redox mediated decomposition of organic waste. However, it is only more recently that photocatalysts have been implemented in photoelectrochemical cells called photocatalytic fuel cells which can capture the charge carriers used in these redox reactions to produce electrical currents. Photocatalytic fuel cells provide robust solutions to the issue of waste water pollution because they are intrinsically self-regenerating in their operation and non-selective in their organic decomposition. In addition to these advantages, photocatalytic fuel cells can operate continuously in a flow-cell configuration, allowing for uninterrupted power generation from waste water streams. These attributes make photocatalytic fuel cells a strong alternative to existing research that wishes to derive electrical power from waste water treatment, mainly microbial fuel cells, which have limited current densities and are difficulty to maintain for extended periods of time. Titanium dioxide (TiO_2) remains the most well-known semiconductor of choice for photocatalysis because of its chemical stability and large redox

potential, and Ag can be combined with TiO_2 in to improve absorbance within the visible range without sacrificing the large redox potential of TiO_2. The combination of a strong visible-light photocatalyst and an efficient flow-cell design has the potential to make the flow-photocatalytic fuel cell a strong candidate for the next generation of devices that can extract electricity from waste water.

A device that can derive electrical power from the waste water treatment process is highly desirable and would help to address both the issues of environmental conservation and energy production. In this chapter, a novel flow-photocatalytic fuel cell was designed, using a burr-like Ag-TiO_2 coated photoanode, as a promising alternative to microbial fuel cells for extracting electricity during waste water treatment. The device provides continuous power generation of 1.85 W m^{-2} under solar-simulated light, with an average COD removal of 14.8% (532 mg L^{-1}).

6.1 Introduction

The topics of energy and the environment continue to present challenges today for society and the scientific community as a whole. As waste from manufacturing industries continues to grow and as environmental and efficient energy sources become more important, research into alternative methods for addressing these problems is needed. The idea that waste reduction can and should provide simultaneously positive energy and environmental outcomes has lead research efforts towards technologies such as recycling, waste reclamation, and conversion. In terms of working with actual waste water streams, research has shown that microbial fuel cells (MFCs) are able derive electrical power from the decomposition of organic waste.[240,241] Unfortunately, there are several major issues with MFCs that currently prevent them from becoming a large-scale technology. First, MFCs rely on specific bacteria and organic material

for their operation, which introduce complexities into the system such as bacterial cultivation, maintenance of bacteria health, and inefficient charge-transfer.[242,243] In conventional MFCs, generated electrons must travel through the metabolic system of the bacteria as well as through bulk waste water before contacting the current collector. This drastically lowers the charge-transfer efficiency of MFCs and contributes to its low power output. Secondly, MFCs rely predominantly on anaerobic digestion of organic material, which means that waste water effluent must be purged of oxygen before being used in an MFC.[244] Thirdly, because of the anaerobic requirement of the MFC, true continuous operation in a conventional flow configuration is much more difficult; MFCs typically operate in a batch-type system.[245]

For these reasons, a unique flow-photocatalytic fuel cell was designed to provide more flexible and resilient power generation from waste water in a continuous process. A flow-photocatalytic fuel cell is based on a conventional photoelectrochemical system that utilizes sunlight to initiate the decomposition of organic components in waste water, and generate electrical current through the resulting redox reactions (**Figure 6-1**). The flow-photocatalytic fuel cell is one such device that has several advantages over current MFC technologies: (i) photocatalyst cell design allows for the fine-tuning of electronic and optical properties to maximize performance depending on waste water composition; (ii) photocatalysts operate based on non-selective oxidation of organic material and can function under various electrolyte and ambient conditions, including both aerobic and anaerobic conditions; (iii) unlike in MFCs, the photocatalyst electrode undergoes redox reactions at the electrode-electrolyte interface, making charge transfer much more efficient; and, (iv) photocatalytic fuel cells rely on inorganic photocatalysts that are chemically stable and self-regenerating. In its current form, a conventional photocatalytic fuel cell[6,126,129,132] is still not a practical device for power generation from waste water treatment. Therefore, it must

be designed in a flow-cell configuration in order to allow continuous operation. For these reasons, flow-photocatalytic fuel cells are a strong candidate as a better technology for generating electricity from waste water treatment.

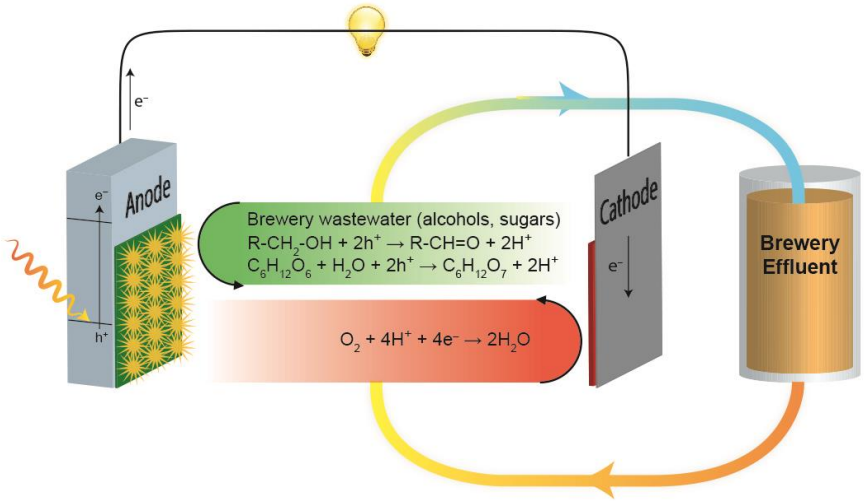

Figure 6-1. Diagram outlining the main processes involved in the operation of a photocatalytic fuel cell with actual process waste water.

The process by which a flow-photocatalytic fuel cell operates is shown in **Figure 6-1**. When a photon strikes the photoanode of the photocatalytic fuel cell with sufficient energy, an electron-hole pair is generated. In an n-type photocatalyst, the hole travels to the electrode-electrolyte interface and undergoes an oxidation reaction with an organic species or water molecule, while the electron travels through the external circuit to the cathode, where it participates in a reduction reaction. The difference in redox potential produces a potential across the device, allowing power to be drawn from the cell. The photocatalytic fuel cell designed in a flow-cell configuration allows more electrolyte, and thus more waste, to be continually fed into the flow-photocatalytic fuel cell and utilized for power generation. A solar-powered flow-photocatalytic fuel cell as a form of power generation from real waste water has yet to be demonstrated in the literature, with

the majority of related work coming from microbial fuel cells (MFCs)[133,246-248] and photocatalytic fuel cells using UV light sources,[130,131] and artificial waste water solutions or model compounds.[128,249,250]

Herein, a brewery waste water-fed flow-photocatalytic fuel cell is demonstrated that uses a burr-like TiO_2 synthesized with Ag nanoparticles (Ag-TiO_2) as the photoanode. Titanium dioxide (TiO_2) is the primary material of choice due to its relative abundance, chemical stability, and photo-oxidizing properties,[24] and plasmonic Ag is used to improve the light absorption and electronic properties of TiO_2 without reducing its redox potential.[13] The Ag-TiO_2 composite is synthesize using a facile solvothermal method, where titanium butoxide is added to glacial acetic acid with varying amounts of silver nitrate. The solution is then heated to 140°C for 12 h in an autoclave and cooled naturally. The resulting powder is washed and heat-treated in air in order to crystallize TiO_2 and form the composite Ag particles. The photoanode is fabricated by forming a slurry of the Ag-TiO_2 composite and drop casting the material on an ITO glass current collector. Finally, the photoanodes are heat-treated in air to improve adhesion before beginning electrochemical testing.

6.2 Experimental Methods

6.2.1 Materials

Titanium butoxide and silver nitrate were both purchased from Sigma Aldrich. Glacial acetic acid was purchased from Fisher Scientific. Pt/C on carbon cloth was purchased from FuelCellEtc. All chemicals were used as received.

6.2.2 Burr-like Ag-TiO_2

Burr-like Ag-TiO_2 was synthesized based on previous work.[251,252] 30 mL glacial acetic acid was purged with N_2 gas for 30 min to remove trace O_2. An appropriate amount of silver nitrate was then dissolved in the solution. 1 mL titanium butoxide was then added to the solution drop-wise under stirring. The solution was allowed to stir for 10 min before being transferred to a 50 mL PTFE-lined autoclave and heated to 140°C for 12 h. The light brown product was washed with de-ionized water and ethanol and dried at 70°C overnight. Anatase Ag-TiO_2 were formed by heat-treating the powder to 700°C for 1 h at 1°C min^{-1} in air. The final product was light blue in colour. TiO_2 was also synthesized without using silver nitrate for comparison.

6.2.3 Characterization

Material characterization was performed using a field-emission scanning electron microscope (FE-SEM, Zeiss ULTRA Plus), X-ray diffractometer (XRD, Rigaku Miniflex 600), and high-resolution transmission electron microscopy (HR-TEM, JEOL 2010F). Optical properties and characterization was conducted using a diffuse reflectance UV-Vis recording spectrophotometer (Shimadzu Corporation UV-2501PC).

Nyquist plots were obtained using electrochemical impedance spectroscopy. A frequency ranging from 1 Hz to 1 MHz was applied, using an alternating signal of 10 mV. Photoelectrochemical measurements were performed using a 1 W 365 nm single-wavelength UV LED (Digikey) as the UV light source and a solar simulator (ABET Technologies 10500) as the 100 mW cm^{-2} (AM1.5 G) solar simulated light source. The distance of the UV LED to the

photoanode surface was adjusted to produce an irradiance of 273 mW cm^{-2} on the electrode surface.

Photoelectrochemical experiments were performed using an electrochemical testing station (Princeton Applied Research VersaSTAT MC). Photoanodes were fabricated by drop-casting a 100 μL ethanol-based slurry on 2.54 cm x 3.81 cm ITO glass current collector. The slurries consisted of 50 mg mL^{-1} active material, 50 μL mL^{-1} titanium butoxide, and the casting area was 2.54 cm x 2.54 cm. The photoanodes were dried in air and heated to 450°C for 1 h at 10°C min^{-1} under Ar gas in order to improve adhesion of the active material to the current collector. In a typical experiment, the prepared photocatalysts were used the photoanode, Pt/C on carbon cloth was used as the cathode, and 1 M H_2SO_4 solution containing 1 M methanol fuel was used as the electrolyte. Approximately 10 mL of brewery effluent was used as the electrolyte for the flow-photocatalytic fuel cell and a peristaltic pump was used to circulate the electrolyte at 0.6 mL min^{-1}. The flow-photocatalytic fuel cell was tested under solar simulated light conditions (AM1.5G, 100 mW cm^{-2}) at 0.275 mA cm^{-2} for 6 h. Chemical oxygen demand (COD) measurements were performed using a Hach DR 1900 Portable Spectrophotometer employing Hach Method 8000.

The flow-chart corresponding to this procedure can be seen in **Figure 6-2**.

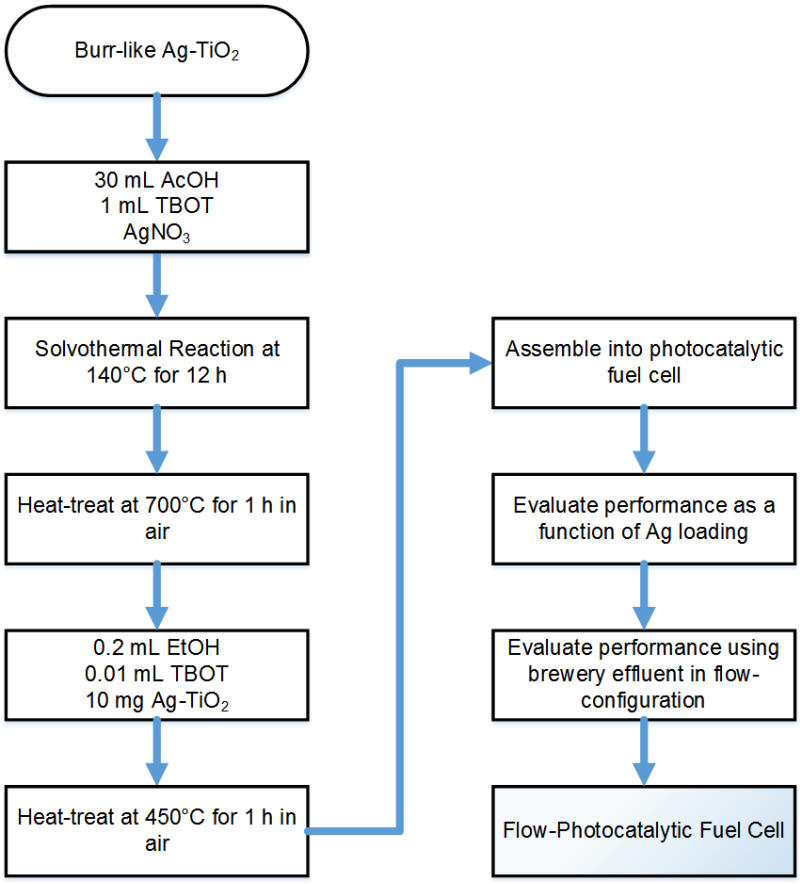

Figure 6-2. Flow-chart outlining the fabrication of Ag-TiO_2 and flow-photocatalytic fuel cell.

6.3 Results and Discussion

The morphological and crystallographic characteristics of Ag-TiO_2 are shown in **Figure 6-4**. After initial solvothermal reaction, the sample is light brown in colour, corresponding to the incorporation of Ag in the amorphous TiO_2 structure (left). Ag likely takes the form of doping, since there is no indication of silver oxides from XRD or SEM. In the absence of Ag precursor, pure TiO_2 is formed after heat treatment (middle). However, when $AgNO_3$ is included in the reaction, the final, heat-treated material is a light blue colour, indicating the formation of nanoparticle Ag on TiO_2 (right).

Figure 6-3. Optical image of (from left to right) Ag-TiO_2 before heat treatment, pure TiO_2 after heat treatment, and Ag-TiO_2 after heat treatment.

The representative SEM images (**Figure 6-4a** and **6-2b**) show that the material consists of relatively uniform, burr-like structures approximately 1 μm – 2 μm in diameter. According to TEM images (**Figure 6-4c**), these burr-like structures consist of smaller nano-sheets approximately 20 nm – 30 nm across, forming a hierarchical TiO_2 morphology. **Figure 6-4d** shows an HRTEM image of an Ag nano-particle on a TiO_2 'branch', consisting of nano-sheets, illustrating the highly crystalline structure of the nano-sheets and the presence of Ag nanoparticles. The lattice spacing on the nano-sheet was found to be 0.35 nm, corresponding to the (101) plane of the anatase phase.[47] The lattice spacing on the nano-particle was found to be 0.204 nm, corresponding to the (200) plane of metallic Ag.[253]

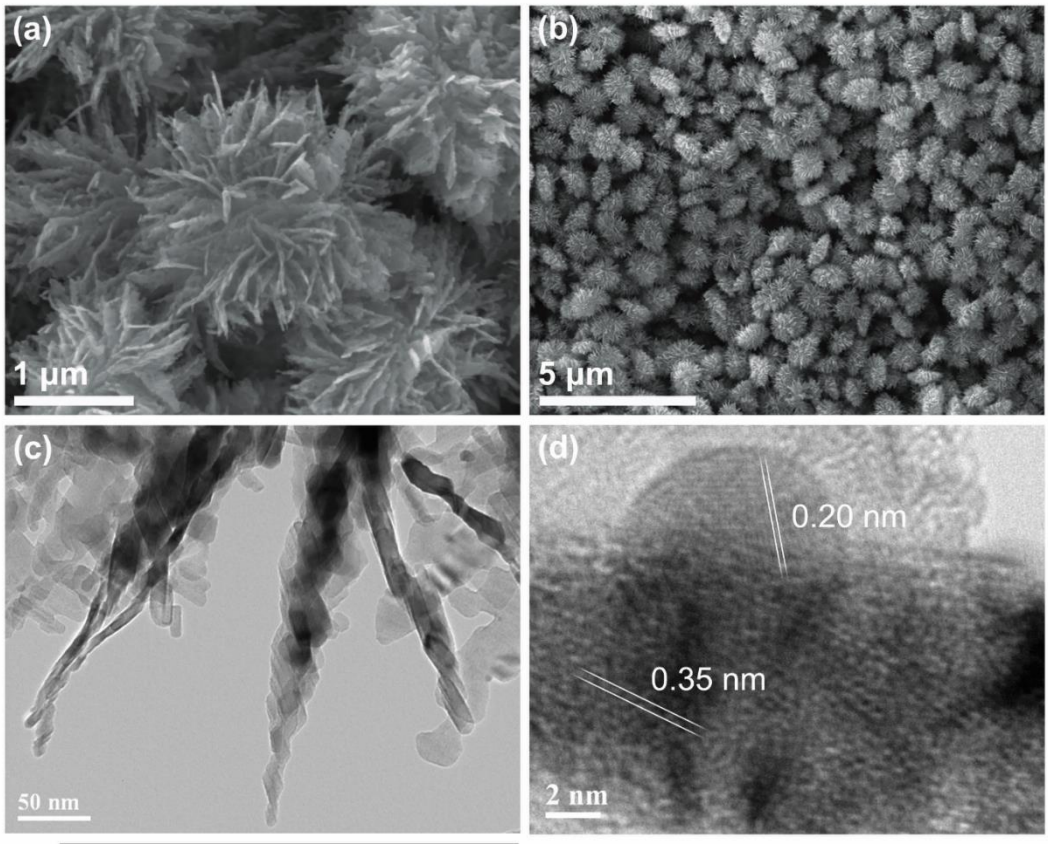

Figure 6-4. Representative SEM images of Ag-TiO_2 at (a) high and (b) low magnification.(c) An TEM image of individual 'branches' of the Ag-TiO_2 consisting of nanosheets, and (d) an HRTEM image of an Ag nanoparticle attached to an individual TiO_2 nanosheet.

These results correspond to the XRD spectra for TiO_2 (**Figure 6-5a**), however the loading of Ag is too small to be present in the XRD spectrum. After heat-treatment, the material converts to the anatase phase of TiO_2. It is pertinent to note that in the absence of Ag, the heat-treated TiO_2 forms a mixed-phase material consisting of both anatase and rutile phases (**Figure 6-4a**). This difference is due to the fact that the presence of the Ag cation can inhibit the conversion of the anatase phase to rutile phase in TiO_2, a common phenomenon found with other cationic dopants.[254] As a low-valence cation, silver can act as an interstitial defect in the TiO_2 lattice, thus interfering with the reconstruction process required for phase transition. The consequences of

this Ag–TiO_2 interaction is also evident in the calculated crystallite sizes of materials with and without Ag present. Using the Scherrer equation, the crystallite size of the pure TiO_2 material is estimated to be 27.9 nm, while the crystallite size of the Ag-TiO_2 composite is 21.4 nm. Using STEM and EDS maps of O, Ti, and Ag (**Figure 6-5b**) the distribution of elements can be clearly seen in the burr morphology. Ag particles can be observed within the TiO_2 structure through Z-contrast, and the EDS map further confirms the presence of Ag throughout the composite.

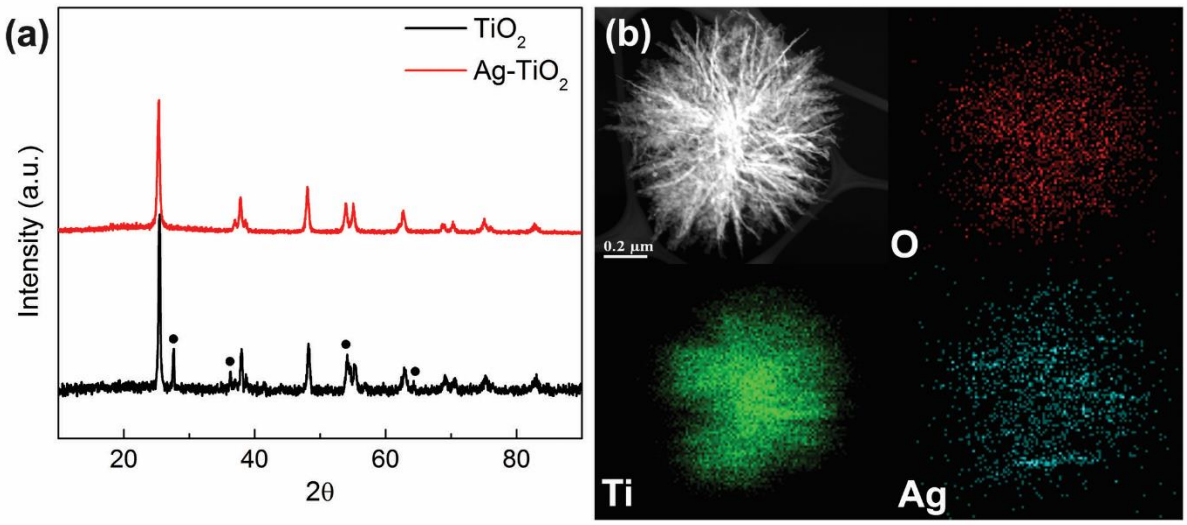

Figure 6-5. (a) STEM image of an Ag-TiO_2 with corresponding EDS map for O, Ti, and Ag.(b) Representative XRD spectra for TiO_2 and Ag-TiO_2 and after heat treatment (• = rutile, other = anatase).

Representative XPS spectra of Ti 2p and Ag 3d are shown in (**Figure 6-6**). The Ti 2p spectrum shows typical $2p_{3/2}$ and $2p_{1/2}$ peaks at 459.48 eV and 465.18 eV, respectively, with a small shift to a higher binding energy compared to TiO_2 synthesized in the absence of Ag (**Figure C-1**) and bulk values.[255] The Ag 3d spectrum shows typical Ag $3d_{5/2}$ and $3d_{3/2}$ peaks at 367.75 eV and 373.75 eV, respectively, with a small shift to a lower binding energy compared to bulk values.[256]

Due to the anomalous behaviour of Ag, both shifts in the Ti and Ag spectra correspond to oxidation, and Ag is likely to take a slightly oxidized form of AgO.

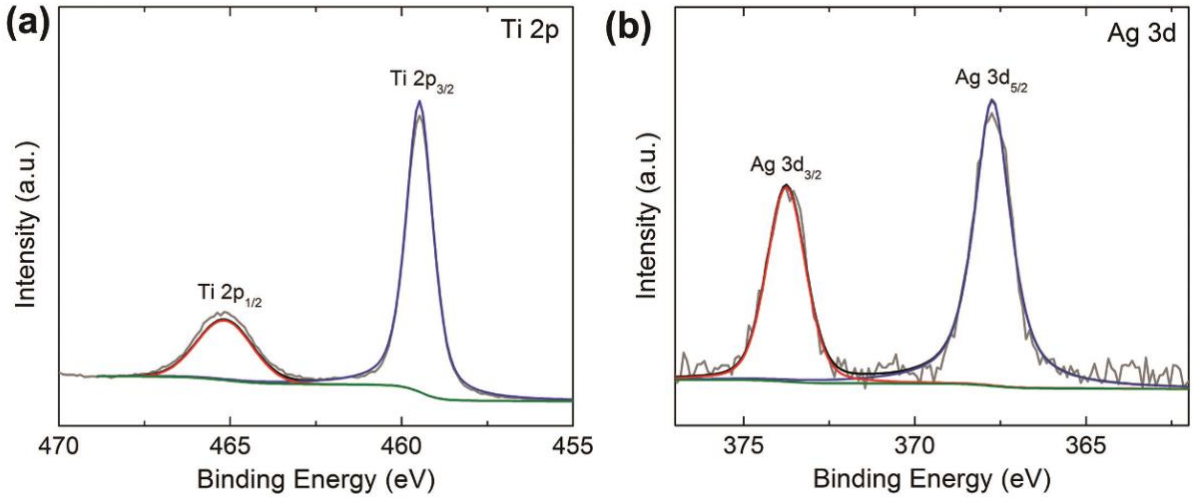

Figure 6-6. High-resolution XPS spectra of (a) Ti 2p and (b) Ag 3d.

In order to evaluate the performance of Ag-TiO_2 as a photocatalyst, the material was integrated into a photocatalytic fuel cell as a photoanode. Pt/C on carbon cloth was used as the cathode current collector and a 1 M H_2SO_4 solution of 1 M methanol was used as the electrolyte. I-V curves were obtained under both UV and solar simulated light (AM 1.5G) irradiation, and P25 was used as a reference electrode for comparison. Under UV (365 nm, 273 mW cm^{-2}) light (**Figure 6-7a**), Ag-TiO_2 has an open-circuit voltage (V_{OC}) of 0.81 V, short-circuit current (I_{SC}) of 6.2 mA cm^{-2}, and a maximum power (P_{max}) of 2.0 mW cm^{-2}. The P25 photoanode has a V_{OC} of 0.88 V, I_{SC} of 2.6 mA cm^{-2}, and a P_{max} of 0.99 mW cm^{-2}. Under solar simulated light (**Figure 6-7b**), Ag-TiO_2 has a V_{OC} of 0.74 V, I_{SC} of 1.9 mA cm^{-2}, and a P_{max} of 0.69 mW cm^{-2}. The P25 photoanode has a V_{OC} of 0.80 V, I_{SC} of 0.48 mA cm^{-2}, and a P_{max} of 0.21 mW cm^{-2}.

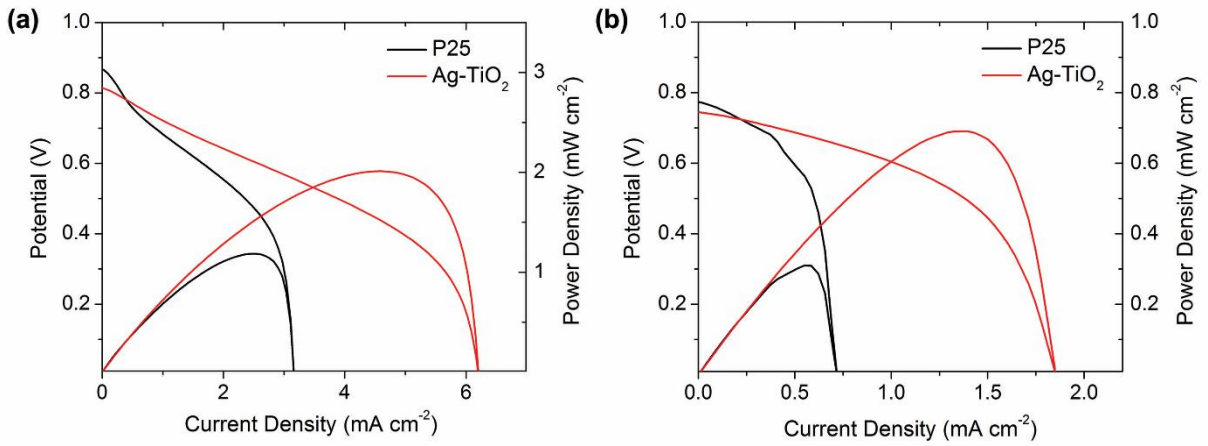

Figure 6-7. I-V curves comparing the performance of Ag-TiO_2 and P25 photoanodes in an alcohol-based photocatalytic fuel cellunder (a) UV (365 nm) light irradiation and (b) solar simulated (100 mW cm^{-2} AM 1.5G) light.

Therefore, the Ag-TiO_2 photoanode provides a marked improvement in photocatalytic fuel cell performance over the reference P25 photoanode. **Figure 6-8a** shows the photocatalytic fuel cell performance of the Ag-TiO_2 photoanode as a function of Ag loading. It was found that an Ag loading of 0.59at% provides the highest P_{max} performance in the photocatalytic fuel cell, while Ag loadings at and above 1.76at% actually decrease the performance of TiO_2 in the photocatalytic fuel cell. The I_{SC} performance as a function of Ag loading confirms this phenomenon and also displays the same trend (**Figure 6-8b**). This phenomenon is likely due to competing effects between the sensitization and internal bias introduced by Ag and photocatalytic activity of TiO_2. As the loading on TiO_2 increases, Ag can decrease the amount of UV reaching TiO_2 and act as recombination centers for electron-hole pairs.[257]

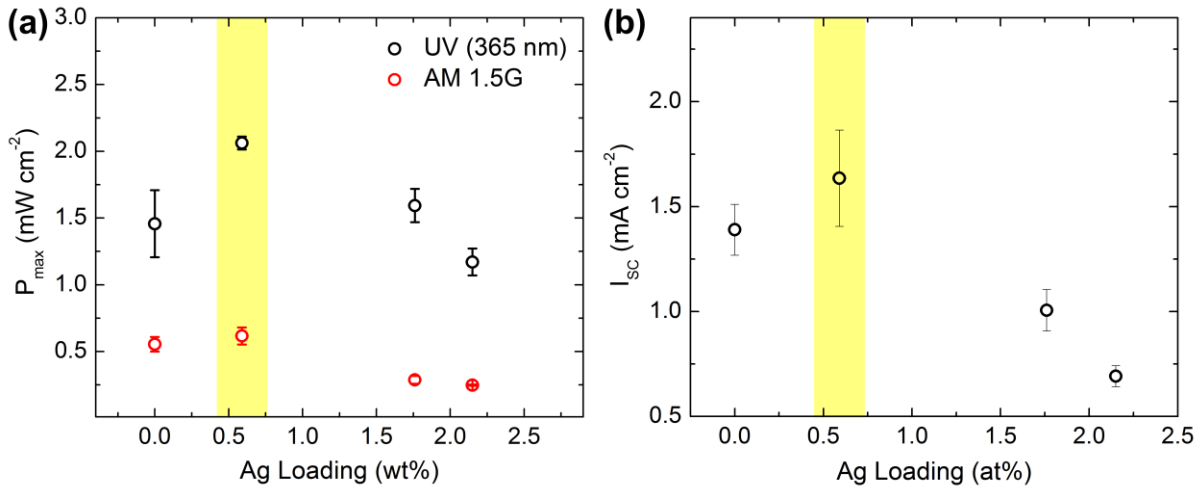

Figure 6-8. (a) Photocatalytic fuel cell performance (P_{max}) as a function of Ag loading, and (b) short-circuit current performance of Ag-TiO_2 photoanodes as a function of Ag loading under solar-simulated light (AM 1.5G) irradiation.

In order to further understand the improved performance of the Ag-TiO_2 (0.59at%) photocatalyst over the commercial photocatalyst, diffuse reflectance spectroscopy was used to look at the optical absorbance and reflectance properties of the catalyst (**Figure 6-9a**).

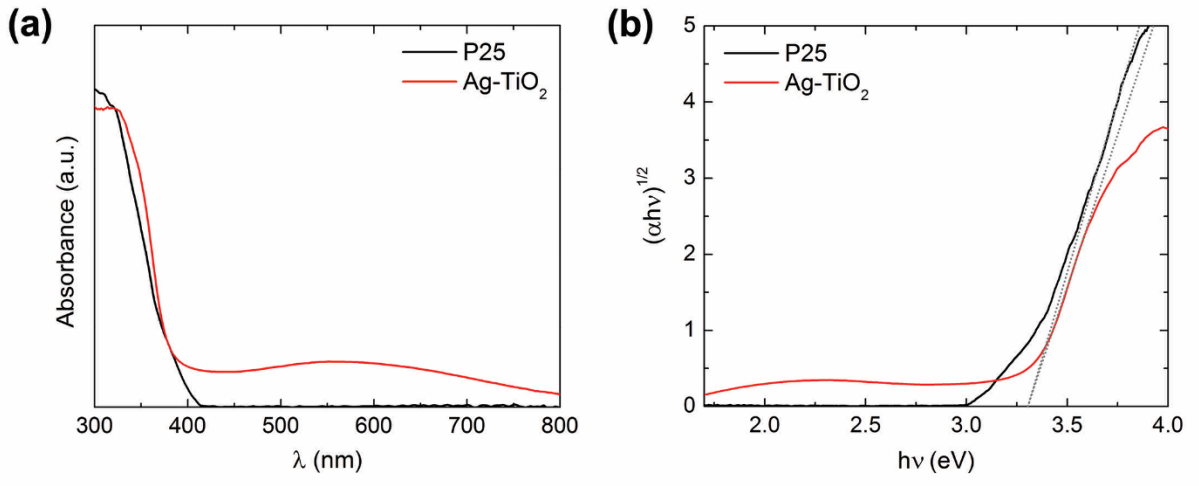

Figure 6-9. (a) DRS absorbance and (b) corresponding Tauc plot comparison of P25 and Ag-TiO_2.

It is clear that TiO_2 only marginally improves absorbance (**Figure C-3a**), while the presence of Ag provides an additional broad absorption peak within the visible region at approximately 560 nm. Similar phenomenon is also seen in the reflectance spectrum (**Figure C-2**) and implies that Ag-TiO_2 has the ability to utilize photons with energies corresponding to the visible light spectrum due to the plasmonic properties of Ag in the composite. Based on XPS and DRS results, Ag contributes a majority Ag plasmonic character, since both Ag_2O and AgO display semiconductors which is not observed in the absorbance plot. A Tauc plot based on this DRS data found that P25 and Ag-TiO_2 have similar band gaps of 3.3 eV (**Figure 6-9b**) with TiO_2 showing a slightly lower band gap (3.14 eV) (**Figure C-3b**). This phenomenon can be explained by two mechanisms: 1) the presence of Ag in Ag-TiO_2 hinders the phase transition of TiO_2 from anatase to rutile. This means that Ag-TiO_2, which is fully anatase, will have a larger band gap than TiO_2, which has a partial rutile phase (**Figure 6-4f**); and, 2) the presence of Ag in Ag-TiO_2 also hinders the growth of TiO_2 crystallites, and it is well known that crystallite size is inversely proportional to the band gap of a semiconductor material.[258,259]

Nyquist plots (**Figure 6-10a and b**) and open-circuit voltage decay (OCVD) (**Figure 6-10d**) comparing Ag-TiO_2 and P25 under both dark and light illumination show that the Ag-TiO_2 photoanodes provide lower series resistance (R_S) (11.9 Ω compared to 13.1 Ω) and a slower V_{OC} decay than P25. Both TiO_2 (**Figure C-3**) and Ag-TiO_2 display higher electron lifetimes over all V_{OC} values, with depressions around 0.6 V corresponding to surface trap states.[260] Additionally, Ag-TiO_2 provides lower charge-transfer resistance in the high V_{OC} region dominated by conduction band charge-transfer.[261]

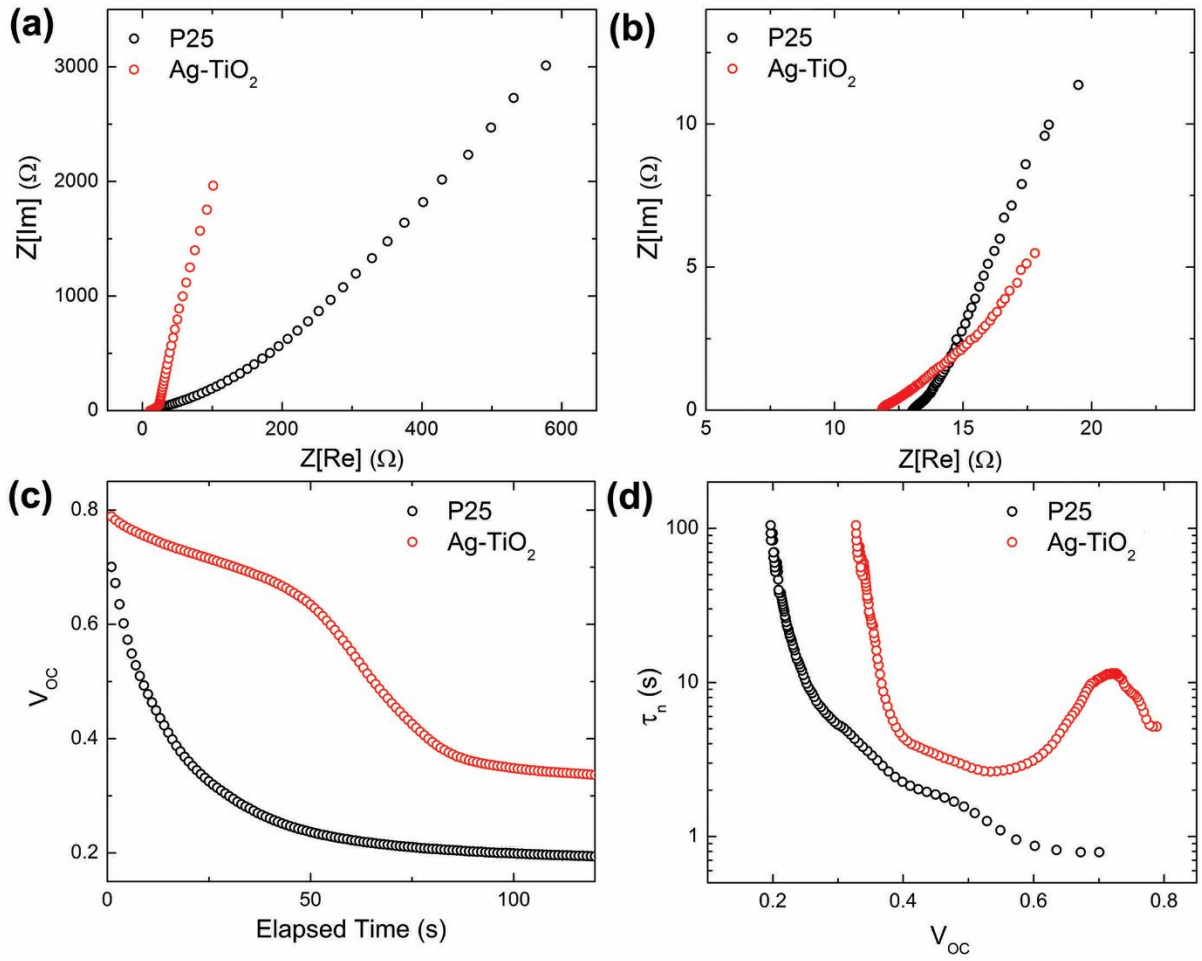

Figure 6-10. Nyquist plots generated from EIS data of Ag-TiO_2 and P25 photoanodes under (a) dark and (b) light conditions.

Based on these results, it can be said that Ag-TiO_2 provides higher photoelectrochemical performance under solar simulated light in spite of a larger band gap, due in part to a plasmonic absorbance peak at ~560 nm. This improvement is supported by performance comparisons between P25 and Ag-TiO_2 materials under both solar-simulated light and visible light (λ>400 nm) only (**Figure 6-11**). Ag-TiO_2 shows a marked improvement under visible light, displaying a 130% and 190% increasing in P_{max} over TiO_2 and P25, respectively.

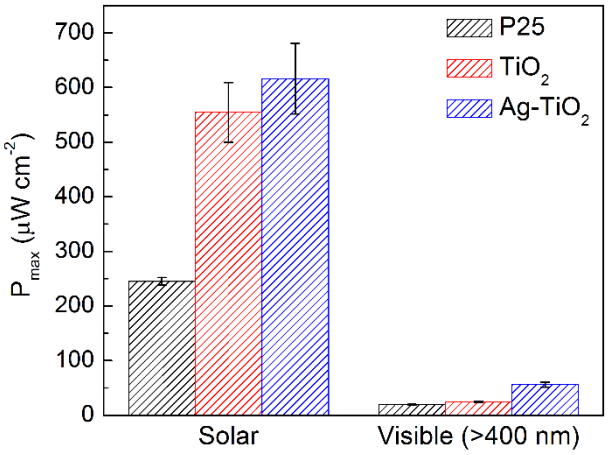

Figure 6-11. P_{max} comparison of P25, TiO_2 and Ag-TiO_2 under both solar simulated light (AM 1.5G, 100 mW cm^{-2}) and under visible light (using a λ>400 nm filter).

Pore and surface area analysis confirmed that this improvement in performance is not due to a difference in surface area (**Figure 6-12**). BET analysis found that P25, TiO_2, and Ag-TiO_2 have surface areas of 46.1 m^2 g^{-1}, 16.4 m^2 g^{-1}, and 12.2 m^2 g^{-1}, respectively. All materials follow an approximate Type II isotherm corresponding to finely divided, non-porous particles. TiO_2 NF has a small hysteresis loops that corresponds to some degree of mesoporosity. It is clear that P25 has a much higher surface area than both TiO_2 and Ag-TiO_2. Yet, despite the significant difference, both the synthesized TiO_2 and Ag-TiO_2 outperform P25 in the photocatalytic fuel cell device.

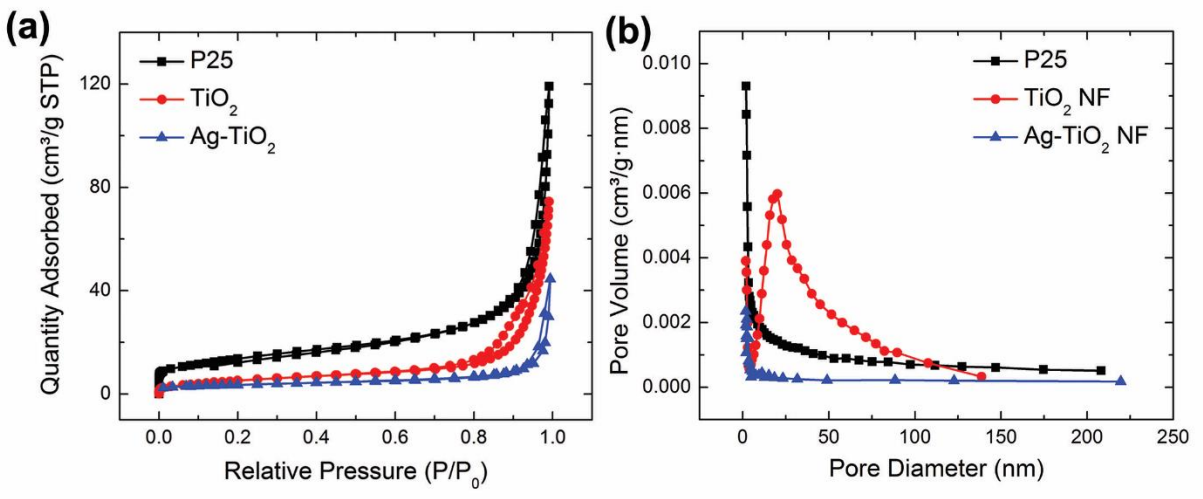

Figure 6-12. Pore and surface analysis showing (a) BET adsorption isotherms and (b) pore size distribution of P25, TiO_2, and Ag-TiO_2.

Based on the results and characterization performed on the Ag-TiO_2 photocatalyst, the following mechanism can be proposed for the photocatalytic activity of the photoanode (**Figure 6-13**): When only TiO_2 is used as the photoanode (in the form of TiO_2 or P25), only ultraviolet light from the solar spectrum can be used for photocatalysis. The lower efficiency of TiO_2 compared to Ag-TiO_2 under UV irradiation is likely due to the higher recombination rate of charge carriers in the absence of the Schottky junction provided by Ag. When Ag is added into the photocatalytic system, a Schottky junction forms between TiO_2 and Ag, creating an internal electric field that encourages the separation of photo-generated electrons and holes. This in turn reduces recombination and improves photocatalytic and photoelectrochemical performance. Based on DRS results and performance data under visible light, Ag acts as a plasmonic co-catalyst that allows for the absorbance of light within the visible light region (with a peak at ~560 nm). In this configuration, excited electrons within Ag can be transferred to the conduction band of TiO_2,

and holes within TiO_2 can be transferred to Ag. Therefore, the oxidation reaction can occur on both TiO_2 (in the valence band) and Ag.

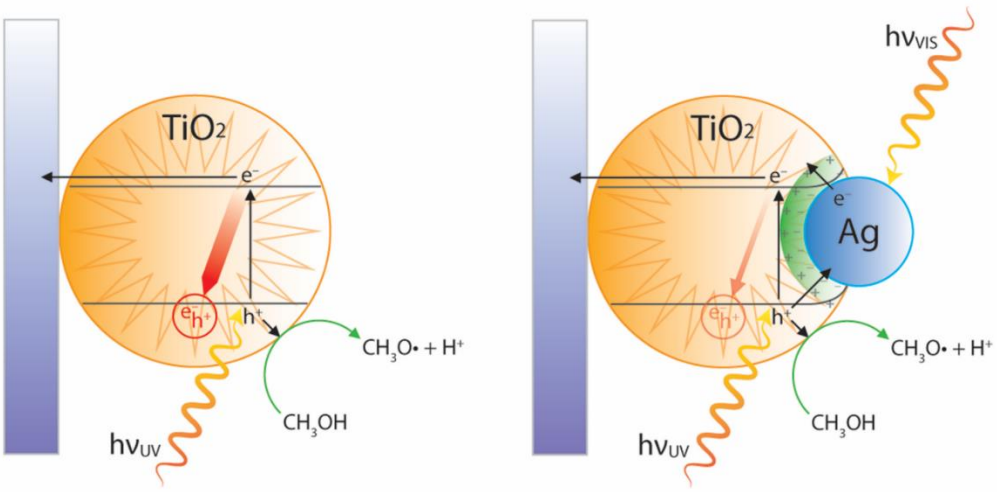

Figure 6-13. Schematic showing probably mechanism for photocatalysis of methanol in the Ag-TiO_2 photocatalytic fuel cell.

In order to determine the real-world viability of this photocatalytic system, the Ag-TiO_2 photoanode was employed in a flow-photocatalytic fuel cell using brewery effluent as the fuel source. Optical images of the cell setup are shown in **Figure 6-14**. Brewery effluent was taken from a local brewery and used as the electrolyte in a flow-photocatalytic fuel cell for continuous operation. The brewery effluent had a typical chemical oxygen demand (COD) value of 3597 ± 62 mg L^{-1} and an approximate pH of 14 due to NaOH treatment. The flow-photocatalytic fuel cell was operated under solar simulated light (AM 1.5G, 100 mW cm^{-2}) at a continuous current of 0.275 mA cm^{-2} (2.75 A m^{-2}) for 6 hours.

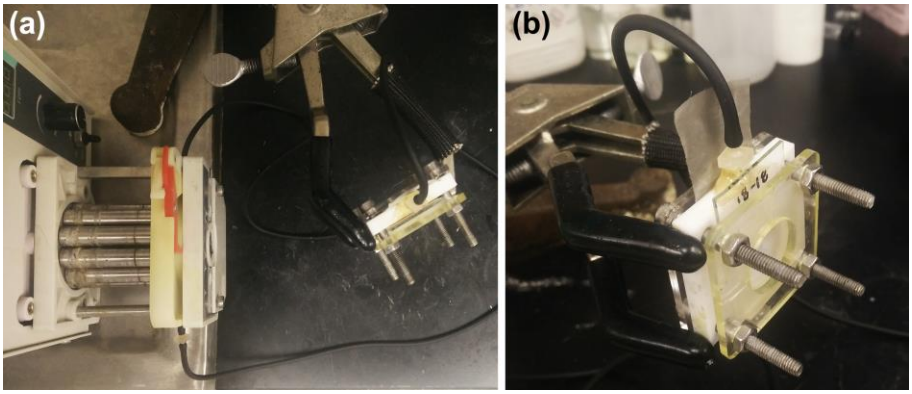

Figure 6-14. Optical images of (a) the flow-photocatalytic fuel cell with peristaltic pumpand (b) a close up of the flow-photocatalytic fuel cell device.

A Nyquist plot for the waste water-fed flow-photocatalytic fuel cell shows the significant change in electronic properties before and after the cell is illuminated (**Figure 6-15**). The series resistance (R_S) of the cell is approximately 46 Ω and the charge transfer resistance (R_{ct}) of the device can be observed to drop from 336 Ω to 23.4 Ω after exposure to solar-simulated light. These results are consistent with previous results in the alcohol photocatalytic fuel cell, and indicate a much more efficient charge transfer during operation.

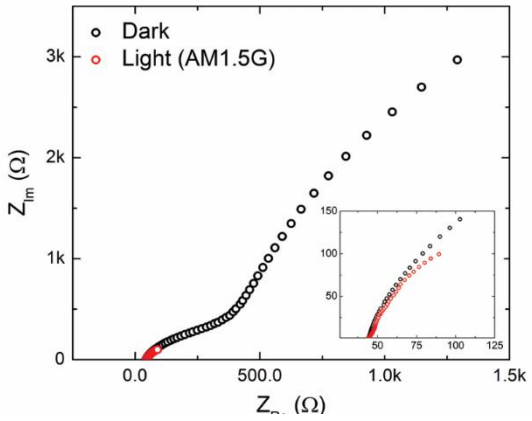

Figure 6-15. Nyquist plot for waste water-fed flow-photocatalytic fuel cell under dark and illuminated conditions.

Figure 6-16a displays the voltage and power density profiles of three experiments at 0.275 mA cm^{-1} (2.75 A m^{-2}) over the course of 6 h. The flow-photocatalytic fuel cell shows relative stability over a 6 h period that is consistent with COD removal with an average initial voltage and power density of 0.888 V and 243 μW cm^{-2} (2.43 W m^{-2}), respectively. By the end of the 6 h of operation, the device achieves an average final voltage and power density of 0.653 V and 185 μW cm^{-2} (1.85 W m^{-2}). **Figure 6-16b** shows the corresponding I-V curves for the three experiments. A P_{max} of 510 ± 1.0 μW cm^{-2} (5.10 W m^{-2}) was achieved using the flow-photocatalytic fuel cell and brewery effluent as fuel. This is among the highest reported voltage and power densities achieved from real waste water using a single-cell configuration with respect to both microbial fuel cells (MFCs) and photocatalytic fuel cells under solar-simulated light (**Table 6-1**). The flow-photocatalytic fuel cell in this work provides an areal power density over 28 times higher than existing photocatalytic fuel cell literature, and over 6 times higher than existing MFC literature.

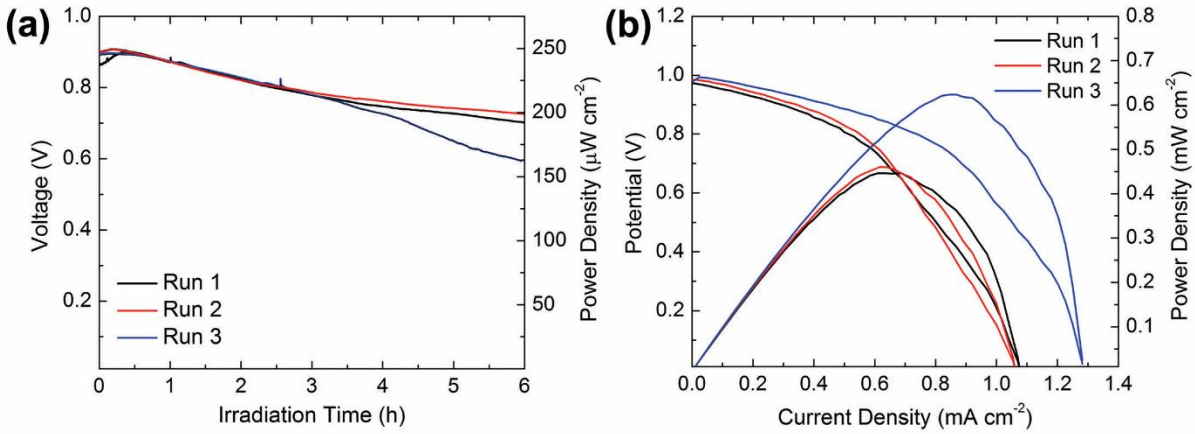

Figure 6-16. (a) Voltage/power density profiles of three experimental runs over a 6 h period.(b) I-V curves corresponding to the three experimental runs.

COD measurements for the three experimental runs are shown in **Figure 6-17**. An average COD removal of 14.8% (532 mg L^{-1}) was achieved over a 6 h period, giving a removal rate of 89 mg L^{-1} h^{-1}. Using a flow rate of 0.6 mL min^{-1}, the flow-photocatalytic fuel cell has a residence time of approximately 47 s. This number compares favourably with MFC technologies, which can only achieve comparable results with residence times on the order of hours to days. With regard to photocatalytic fuel cell literature, this work produces unprecedented photocatalytic fuel cell performance in a flow context using real waste water at relatively high COD concentration.

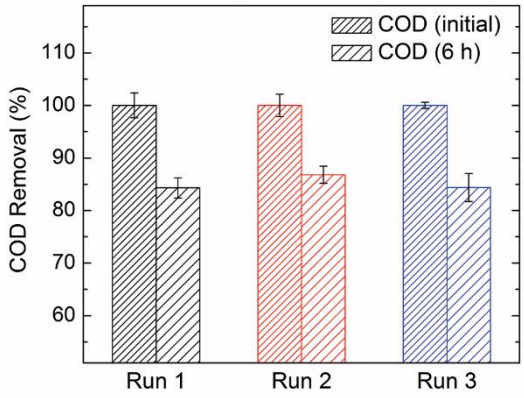

Figure 6-17. COD removal (%) of the three experimental runs over the course of 6 h.

The coulombic efficiency (CE) of the flow-photocatalytic fuel cell can be calculated by dividing the capacity obtained from the cell (Ah) by the total COD removed during device operation, and is given by the following equation (Equation 6-1):

$$CE = \frac{M_{O_2} \int Idt}{nFV\Delta COD} \quad (6\text{-}1)$$

where M is the molar mass of O_2, $\int Idt$ is the total charge capacity obtained from the cell, n is the number of electrons generated from O_2 (n = 4), F is Faraday's constant (96485 s A mol^{-1}), V is

the volume of the electrolyte, and ΔCOD is the change in COD (mg L^{-1}). The average coulombic efficiency of the flow-photocatalytic fuel cell is 9.4% ± 0.9%, and is comparable to MFC literature at similar COD concentration.[133,247,248] Literature shows that COD concentration has a significant effect on coulombic efficiency,[133,247] and to the best of our knowledge this work is the first instance in photocatalytic fuel cell literature of handling such high COD waste water effluent with comparable coulombic efficiencies.

Table 6-1: Tabulated comparison of this work with single-cell photocatalytic fuel cell(abbreviated as PFC here) and MFC devices using real waste water effluent as fuel sources.

Device Type	Waste water	Cell Type	COD (mg L^{-1})	Removal Rate (mg L^{-1} h^{-1})	Operating Voltage (V)	P_{max} (W m^{-2})	Ref.
PFC	***Brewery***	***Flow***	***3597***	*89*	***0.888***	***5.10***	***This Work***
PFC	Textile	Batch	103	8.4	0.60	0.113	130‡
PFC	WWTP Effluent	Batch	20	3.1	0.55†	0.18	131
MFC	Sewage	Flow	9978	1.5	0.762	0.382	245
MFC	Distillery	Flow	6000	284	0.611	0.124	246
MFC	Brewery	Batch	2239	26.4	0.467	0.483	133
MFC	Brewery	Flow	1250	81.6	0.068	0.830	262
MFC	Brewery	Batch	510	4.3	0.567†	0.251	263

* No long-term experiments were performed using this waste water as substrate.
† Operating voltage data was not given, so OCV data is shown instead.
‡ This work performed photocatalytic fuel cell tests under UV light, and is not representative of performance under solar irradiation.

6.4 Conclusions

A flow-photocatalytic fuel cell was designed to provide superior power generation from brewery waste water effluent. The photoanode was fabricated using a burr-like Ag-TiO_2 composite that has improved photocatalytic performance under solar-simulated light due to the improved conductivity of the composite and the visible light activity of plasmonic Ag. This design provides

a stable catalyst for the degradation of organic waste in waste water in a flow-configuration, without the stringent conditions associated with operating a microbial fuel cell. When incorporated into a flow-photocatalytic fuel cell using brewery effluent as the fuel source, the device was able to run at 2.75 A m^{-2} over a 6 h period, generating a minimum voltage and power density of 0.653 V and 1.85 W m^{-2}, respectively. An average COD removal of 14.8% (532 mg L^{-1}) was achieved over a 6 period, and the cell achieves an average coulombic efficiency of 9.4%. This performance is among the highest recorded for single-cell MFCs and photocatalytic fuel cells using real waste water effluent as the fuel source. This work provides further basis for solar-power photocatalytic fuel cells as a practical method for generating electrical power from the remediation of waste water.

7.0 Conclusions & Future Work

In this thesis, various titanium oxide (TiO_2)-based electrochemical systems were fabricated with the objective of fabricating novel multifunctional photoelectrochemical systems. Specifically, TiO_2 nanomaterials were used as a starting point for designing photocatalytic fuel cells that could use light irradiation to draw electrical power from the photodegradation of organic compounds in various sources, including human sweat, textile dye waste, and brewery effluent. Various TiO_2-based materials were employed and synthesized, including commercial P25, three-dimensional ordered macroporous (3DOM) TiO_2, and burr-like Ag-TiO_2. This chapter outlines the conclusions and proposed future work for the research performed in this thesis.

7.1 Conclusions

7.1.1 Flexible, Three-Dimensional Ordered Macroporous TiO_2 Electrode with Enhanced Electrode-Electrolyte Interaction in High-Power Li-Ion Batteries

3DOM TiO_2 was synthesized using polystyrene (PS) colloidal crystal templates (CCTs) as a hard template. Unfortunately, the application of 3DOM TiO_2 on ITO/glass proved very difficult, and its application in powder-based photocatalyst was not competitive with commercial P25 to be a viable photocatalytic material. Instead, the material was applied more effectively as an anode material in a Li-ion battery electrochemical system as a flexible, binder-free carbon cloth anode. This was accomplished by dip-coating a carbon cloth current collector in PS solution and allowing PS beads to self-assemble in to CCT-like structures on individual fibers. The PS-coated carbon cloth was then dipped TiO_2 precursor solution and heat-treated to achieve 3DOM TiO_2 on carbon cloth. The macroporous porosity and highly accessible surface area of the 3DOM

structure were highly transferrable properties that allowed the material to provide high power performance and long cycling life in half-cell testing. This work provided the highest performance among flexible, binder-free TiO_2-based anodes at the time of publishing, and was the first instance of functional 3DOM structures on flexible (non-planar) substrates.

7.1.2 Advanced Biowaste-Based Flexible Photocatalytic Fuel Cell as a Green Wearable Power Generator

A flexible photocatalytic fuel cell was fabricated as a proof-of-concept device that could derive electrical power from the decomposition of organic compounds in human sweat and textile dye waste. The flexible photocatalytic fuel cell was shown to produce electrical power under light irradiation from various fuels including lactic acid, ethanol, methanol, urea, glycerol, and glucose under bendering (r = 3 cm) conditions. Finally, the flexible photocatalytic fuel cell was able to produce appreciable power under light irradiation using artificial human sweat and textile dye solutions. This work provided a novel method for generation electricity from human sweat using a wearable format that is competitive with current technologies. This work also presented an alternative configuration for photocatalysis that allows energy to be produced from photodegradation of compounds such as methylene blue in a flexible format.

7.1.3 A High Performance Waste water-Fed Flow-Photocatalytic Fuel Cell

A flow-photocatalytic fuel cell was fabricated using burr-like Ag-TiO_2 as the photoanode material. The composite was synthesized using a solvothermal reaction with varying amounts of Ag. The synthesized composite containing 0.59at% Ag showed an improve photocatalytic performance over pure TiO_2 and commercial P25 under both UV light (365 nm) and solar

simulated light (AM 1.5G). In this work, brewery effluent was sourced form a local brewery to be used as a fuel source in a flow configuration. The flow-photocatalytic fuel cell showed significant photoelectrochemical performance over a 6 h operation period, providing competitive sustained electrical power output and reduction in effluent COD. The flow-photocatalytic fuel cell in this work provided areal power densities 28 times higher than microbial fuel cells and 6 times higher than photocatalytic fuel cells using actual waste water in a single-cell configuration. This work was also the first instance of power generation from real-waste water photocatalysis in a flow context for sustained periods of time.

7.2 Recommendations & Future Work

7.2.1 Analysis of Rate Limiting Steps

The results found in this work have shown the viability of a photocatalytic fuel cell device in the application of real waste water treatment. Further analysis can be done in order to better understand this photoelectrochemical system and its sensitivity toward different operating parameters such as light irradiance, incident photon to efficiency (IPCE), mass transfer and flow rate, COD characteristics (pH, conductivity, concentration), and O_2 concentration. These analyses can provide a better understanding of how photocatalytic fuel cell devices will operating in real-world or non-ideal conditions and how to better design photocatalytic materials and devices.

7.2.2 Alternative Effluent Sources

Flow-photocatalytic fuel cells have real-world viability in that they have the potential to provide decomposition of waste water streams using just natural sunlight in a continuous process.

Brewery effluent is a desirable source of organic waste due to the existence large amounts of highly oxidizable alcohols and sugars. Although handling brewery effluent is fairly simple from a waste water treatment perspective, it does not necessarily render flow-photocatalytic fuel cell technologies redundant since photocatalytic fuel cells provide an additional functionality in the form of power generation.

However, in order to fully utilize the specific advantages of photocatalytic technologies, it is worthwhile to explore alternative effluent sources where photocatalysis can play a more necessary role in organic degradation. These effluent sources include effluent from textile industries, pharmaceuticals and endocrine disruptors, personal care products, and various other polyaromatic hydrocarbons.[264] Photocatalytic fuel cells can therefore be decentralized to specific industries producing these waste streams or centralized to waste water treatment facilities (as a tertiary treatment step). Photocatalytic fuel cells can also aid industries in reaching suitable discharge concentrations for municipal waste water treatment plants. These methods would maximize the utility of photocatalytic fuel cell technologies by tackling problem compounds in the waste water treatment process and generating electrical power as a secondary function.

7.2.3 Improved Heterostructuring of Plasmonic and Small Band-Gap Semiconductors

TiO_2 remains the strongest candidate for photocatalysis under both UV and solar simulated light. This fact suggests that heterostructuring TiO_2 in order to improve visible-light activity remains the most promising method for improving photocatalytic processes. As shown in **Chapter 6**, plasmonic materials make great composites for photocatalysis because they can improve light absorption in the visible-NIR range through LSPR while essentially leaving the redox potential of TiO_2 unchanged. The LSPR of plasmonic materials like Ag and Au can be greatly modified

and enhanced through tuning morphology.[13] The challenge will be appropriately fine-tuning the shape of Ag and Au while successfully heterostructuring these materials with TiO_2 to improve overall photocatalytic activity under sunlight.

Other materials that are candidates for heterostructuring are small band-gap semiconductors. Preferably, these materials are relatively stable in various electrolyte environments and form a type II heterojunction with TiO_2. More recently, materials such as metal sulfides[265] and carbon nitrides[266] are materials that can not only improve the absorption properties of TiO_2 but also assist in reduction reactions such as hydrogen evolution.

7.2.4 Flexible Photocatalytic Fuel Cells for Suspended Power Generation in Water Reservoirs

Research covered in **Chapter 5** suggests that photocatalytic fuel cells can be suspended over bodies of (contaminated) water sources, either mechanically or through floatation. In addition to generation electrical power, this technology would serve additional purpose of: 1) reducing the amount of water evaporation in a body of water; and 2) helping to remove pollutants from a polluted body of water. This iteration of the photocatalytic fuel cell could be deployed in various industries, including waste water treatment plants and tailing ponds from various industries.

Improvement of the electrode design in this case could greatly enhance the application of the device. Coating of meshs such as stainless steel could provide a simple substrate and current collector. Addition of the photocatalyst through electrodeposition could also improve the overall stability of the device.

7.2.5 Two-Compartment Reactor Systems and H_2 production

In this these only a single-compartment reactor system has been proposed for multifunctional photocatalysis (see **Chapters 5 and 6**). These systems are useful because of their simplicity, especially when considering real-world applications and viability in actual waste water treatment infrastructure. When considering novel photocatalytic fuel cell systems, a two-compartment reactor system can be beneficial for separating electrolyte environments between the anode and cathode and tailoring those electrolytes for specific functions. For example, it is well known that if the anolyte is made alkaline while the catholyte is made acidic, the overall cell experiences a chemical bias that can increase the overall potential between the electrodes. In this manner, conventional photocatalytic fuel cells can reach V_{OC} values greater than 1 V.[6]

Another function of two-compartment reactors systems is tailoring each electrolyte for specific redox reactions. For example, in a photocatalytic fuel cell context the photoanode can remain responsible for photo-oxidation of anolyte containing all relevant organic waste. The cathode can be responsible for H_2 evolution using a proton-rich catholyte without the dangers of poisoning from the anolyte.

7.2.6 Photocathode in a Photoassisted Flow-Battery

Another avenue for exploration for multifunctional photoelectrochemical cells using photocatalysts is the photo-assisted flow battery. Photocatalytic fuel cells have shown that they can generate electrical currents from oxidation reactions. The relatively high Fermi level of TiO_2 also means that these photocatatalysts have the potential to reduce the charging voltage of certain

energy storage systems by artificially increasing the oxidation potential at the cathode under light irradiation.

For example, in a ZnI_2 flow battery,[267] the charging/oxidation reaction at the cathode ($3I^- \leftrightarrow I_3^- + 2e^-, 0.54\ V\ vs. SHE$) can be initiated by photo-generated holes on TiO_2.[268] In this scenario, the photo-generated electrons have a potential of about -0.3 V vs. SHE, providing a theoretical voltage savings of over 0.8 V in the charging reaction. Reducing the charging voltage of the energy storage system can help reduce the overall power required for charging and increase the efficiency of the system. Photoanodes such as those fabricated in **Chapter 6** can be easily transferred over to an energy storage system, such as the ZnI_2 flow battery, and perform photo-oxidation of I_2 during charging while a secondary cathode, such as graphite, can be used for discharge reactions.

8.0 References

(1) *Canada's Emissions Trends*; Environment Canada: 2013; pp 15-16.

(2) Fujishima, A.; Honda, K., Electrochemical Photolysis of Water at a Semiconductor Electrode. *Nature* **1972,** *238* (5358), 37-38.

(3) Fujishima, A.; Rao, T. N.; Tryk, D. A., Titanium dioxide photocatalysis. *J. Photochem. Photobiol., C* **2000,** *1* (1), 1-21.

(4) O'Regan, B.; Graetzel, M., A low-cost, high-efficiency solar cell based on dye-sensitized colloidal TiO2 films. *Nature* **1991,** *353*, 737-740.

(5) Li, X.; Shen, B.; Xu, C., Interaction of titanium and iron oxide with ZSM-5 to tune the catalytic cracking of hydrocarbons. *Applied Catalysis A: General* **2010,** *375* (2), 222-229.

(6) Lianos, P., Production of electricity and hydrogen by photocatalytic degradation of organic wastes in a photoelectrochemical cell: The concept of the Photofuelcell: A review of a re-emerging research field. *J. Hazard. Mater.* **2011,** *185* (2–3), 575-590.

(7) Gueymard, C. A., The sun's total and spectral irradiance for solar energy applications and solar radiation models. *Solar Energy* **2004,** *76* (4), 423-453.

(8) Leary, R.; Westwood, A., Carbonaceous nanomaterials for the enhancement of TiO2 photocatalysis. *Carbon* **2011,** *49* (3), 741-772.

(9) Chen, X.; Li, C.; Gratzel, M.; Kostecki, R.; Mao, S. S., Nanomaterials for renewable energy production and storage. *Chem. Soc. Rev.* **2012,** *41*, 7909-7937.

(10) Liu, G.; Wang, L.; Yang, H. G.; Cheng, H.-M.; Lu, G. Q., Titania-based photocatalysts-crystal growth, doping and heterostructuring. *J. Mater. Chem.* **2010,** *20* (5), 831-843.

(11) Chen, J. I. L.; von Freymann, G.; Choi, S. Y.; Kitaev, V.; Ozin, G. A., Amplified Photochemistry with Slow Photons. *Adv. Mater.* **2006,** *18* (14), 1915-1919.

(12) Stein, A.; Wilson, B. E.; Rudisill, S. G., Design and functionality of colloidal-crystal-templated materials-chemical applications of inverse opals. *Chem. Soc. Rev.* **2013,** *42* (7), 2763-2803.

(13) Zhang, X.; Chen, Y. L.; Liu, R.-S.; Tsai, D. P., Plasmonic photocatalysis. *Reports on Progress in Physics* **2013,** *76* (4), 046401.

(14) Takahashi, K.; Yoshikawa, A.; Sandhu, A., *Wide Bandgap Semiconductors: Fundamental Properties and Modern Photonic and Electronic Devices*. Springer London, Limited: 2007.

(15) Stevanovic, A.; Buttner, M.; Zhang, Z.; Yates, J. T., Photoluminescence of TiO2: Effect of UV Light and Adsorbed Molecules on Surface Band Structure. *J. Am. Chem. Soc.* **2012,** *134* (1), 324-332.

(16) Zhang, Z.; Yates, J. T., Band Bending in Semiconductors: Chemical and Physical Consequences at Surfaces and Interfaces. *Chem. Rev.* **2012,** *112* (10), 5520-5551.

(17) Hwang, Y. J.; Boukai, A.; Yang, P., High Density n-Si/n-TiO2 Core/Shell Nanowire Arrays with Enhanced Photoactivity. *Nano Lett.* **2009,** *9* (1), 410-415.

(18) Greenwood, N. N.; Earnshaw, A., *Chemistry of the Elements*. Oxford: Pergamon Press: 1984; p 1117-1119.

(19) Gratzel, M., Photoelectrochemical cells. *Nature* **2001,** *414* (6861), 338-344.

(20) Maness, P.-C.; Smolinski, S.; Blake, D. M.; Huang, Z.; Wolfrum, E. J.; Jacoby, W. A., Bactericidal Activity of Photocatalytic TiO2 Reaction: toward an Understanding of Its Killing Mechanism. *Appl. Environ. Microbiol.* **1999,** *65* (9), 4094-4098.

(21) Dalton, J. S.; Janes, P. A.; Jones, N. G.; Nicholson, J. A.; Hallam, K. R.; Allen, G. C., Photocatalytic oxidation of NOx gases using TiO2: a surface spectroscopic approach. *Environ. Pollut.* **2002,** *120* (2), 415-422.

(22) Ghosh, S.; Das, A. P., Modified titanium oxide (TiO2) nanocomposites and its array of applications: a review. *Toxicological & Environmental Chemistry* **2015,** *97* (5), 491-514.

(23) Linsebigler, A. L.; Lu, G.; Yates, J. T., Photocatalysis on TiO2 Surfaces: Principles, Mechanisms, and Selected Results. *Chem. Rev.* **1995,** *95* (3), 735-758.

(24) Carp, O.; Huisman, C. L.; Reller, A., Photoinduced reactivity of titanium dioxide. *Prog. Solid State Chem.* **2004,** *32* (1–2), 33 - 177.

(25) Fujishima, A.; Zhang, X.; Tryk, D. A., TiO2 photocatalysis and related surface phenomena. *Surf. Sci. Rep.* **2008,** *63* (12), 515-582.

(26) Park, N. G.; van de Lagemaat, J.; Frank, A. J., Comparison of Dye-Sensitized Rutile- and Anatase-Based TiO2 Solar Cells. *The Journal of Physical Chemistry B* **2000,** *104* (38), 8989-8994.

(27) Riegel, G.; Bolton, J. R., Photocatalytic Efficiency Variability in TiO2 Particles. *The Journal of Physical Chemistry* **1995,** *99* (12), 4215-4224.

(28) Li, G.; Gray, K. A., Preparation of Mixed-Phase Titanium Dioxide Nanocomposites via Solvothermal Processing. *Chem. Mater.* **2007,** *19* (5), 1143-1146.

(29) Scanlon, D. O.; Dunnill, C. W.; Buckeridge, J.; Shevlin, S. A.; Logsdail, A. J.; Woodley, S. M.; Catlow, C. R. A.; Powell, M. J.; Palgrave, R. G.; Parkin, I. P.; Watson, G. W.; Keal, T. W.; Sherwood, P.; Walsh, A.; Sokol, A. A., Band alignment of rutile and anatase TiO2. *Nat. Mater.* **2013,** *12* (9), 798-801.

(30) Luo, H.; Takata, T.; Lee, Y.; Zhao, J.; Domen, K.; Yan, Photocatalytic Activity Enhancing for Titanium Dioxide by Co-doping with Bromine and Chlorine. *Chem. Mater.* **2004,** *16* (5), 846-849.

(31) Shannon, R. D.; Pask, J. A., Kinetics of the Anatase-Rutile Transformation. *J. Am. Ceram. Soc.* **1965,** *48* (8), 391-398.

(32) Tang, H.; Prasad, K.; Sanjinès, R.; Schmid, P. E.; Lévy, F., Electrical and optical properties of TiO2 anatase thin films. *J. Appl. Phys.* **1994,** *75* (4), 2042-2047.

(33) Abayev, I.; Zaban, A.; Fabregat-Santiago, F.; Bisquert, J., Electronic conductivity in nanostructured TiO2 films permeated with electrolyte. *physica status solidi (a)* **2003,** *196* (1), R4-R6.

(34) Anpo, M.; Kamat, P. V., *Environmentally Benign Photocatalysts: Applications of Titanium Oxide-based Materials*. Springer: 2010.

(35) *Carbon Black, Titanium Dioxide, and Talc*; International Agency for Research on Cancer: Lyon, France, 2010.

(36) DuPont. DuPont Ti-Pure titanium dioxide 2007. (accessed 17 March 2014).

(37) Boffetta, P.; Soutar, A.; Cherrie, J. W.; Granath, F.; Andersen, A.; Anttila, A.; Blettner, M.; Gaborieau, V.; Klug, S. J.; Langard, S.; Luce, D.; Merletti, F.; Miller, B.; Mirabelli, D.; Pukkala, E.; Adami, H.; Olov; Weiderpass, E., Mortality Among Workers Employed in the Titanium Dioxide Production Industry in Europe. *Cancer Causes and Control* **2004,** *15* (7), 697-706.

(38) Ong, W.-J.; Tan, L.-L.; Chai, S.-P.; Yong, S.-T.; Mohamed, A. R., Facet-Dependent Photocatalytic Properties of TiO2-Based Composites for Energy Conversion and Environmental Remediation. *Chemsuschem* **2014,** *7* (3), 690-719.

(39) Chen, X.; Mao, S. S., Titanium Dioxide Nanomaterials: Synthesis, Properties, Modifications, and Applications. *Chem. Rev.* **2007,** *107* (7), 2891-2959.

(40) Hench, L. L.; West, J. K., The sol-gel process. *Chem. Rev.* **1990,** *90* (1), 33-72.

(41) Testino, A.; Bellobono, I. R.; Buscaglia, V.; Canevali, C.; D'Arienzo, M.; Polizzi, S.; Scotti, R.; Morazzoni, F., Optimizing the Photocatalytic Properties of Hydrothermal TiO2 by the Control of Phase Composition and Particle Morphology. A Systematic Approach. *J. Am. Chem. Soc.* **2007,** *129* (12), 3564-3575.

(42) Liu, N.; Chen, X.; Zhang, J.; Schwank, J. W., A review on TiO2-based nanotubes synthesized via hydrothermal method: Formation mechanism, structure modification, and photocatalytic applications. *Catal. Today* **2014,** *225* (0), 34-51.

(43) Yang, H. G.; Liu, G.; Qiao, S. Z.; Sun, C. H.; Jin, Y. G.; Smith, S. C.; Zou, J.; Cheng, H. M.; Lu, G. Q., Solvothermal Synthesis and Photoreactivity of Anatase TiO2 Nanosheets with Dominant {001} Facets. *J. Am. Chem. Soc.* **2009,** *131* (11), 4078-4083.

(44) Wang, J.; Tafen, D. N.; Lewis, J. P.; Hong, Z.; Manivannan, A.; Zhi, M.; Li, M.; Wu, N., Origin of Photocatalytic Activity of Nitrogen-Doped TiO2 Nanobelts. *J. Am. Chem. Soc.* **2009,** *131* (34), 12290-12297.

(45) De Marco, L.; Manca, M.; Giannuzzi, R.; Malara, F.; Melcarne, G.; Ciccarella, G.; Zama, I.; Cingolani, R.; Gigli, G., Novel Preparation Method of TiO2-Nanorod-Based Photoelectrodes for Dye-Sensitized Solar Cells with Improved Light-Harvesting Efficiency. *J. Phys. Chem. C* **2010,** *114* (9), 4228-4236.

(46) Wen, B.-M.; Liu, C.-Y.; Liu, Y., Solvothermal synthesis of ultralong single-crystalline TiO2 nanowires. *New J. Chem.* **2005,** *29* (7), 969-971.

(47) Liao, J.-Y.; Higgins, D.; Lui, G.; Chabot, V.; Xiao, X.; Chen, Z., Multifunctional TiO2–C/MnO2 Core–Double-Shell Nanowire Arrays as High-Performance 3D Electrodes for Lithium Ion Batteries. *Nano Lett.* **2013,** *13* (11), 5467-5473.

(48) Zhao, Z.; Jiao, X.; Chen, D., Preparation of TiO2 aerogels by a sol-gel combined solvothermal route. *J. Mater. Chem.* **2009,** *19* (19), 3078-3083.

(49) Stein, A.; Schroden, R. C., Colloidal crystal templating of three-dimensionally ordered macroporous solids: materials for photonics and beyond. *Current Opinion in Solid State and Materials Science* **2001,** *5* (6), 553-564.

(50) Wu, M.; Li, Y.; Deng, Z.; Su, B.-L., Three-Dimensionally Ordered Macroporous Titania with Structural and Photonic Effects for Enhanced Photocatalytic Efficiency. *Chemsuschem* **2011,** *4* (10), 1481-1488.

(51) Chen, J. I. L.; von Freymann, G.; Choi, S. Y.; Kitaev, V.; Ozin, G. A., Slow photons in the fast lane in chemistry. *J. Mater. Chem.* **2008,** *18* (4), 369-373.

(52) Safriani, L.; Cai, B.; Komatsu, K.; Sugihara, O.; Kaino, T., Fabrication of Inverse Opal TiO 2 Waveguide Structure. *Japanese Journal of Applied Physics* **2008,** *47* (2S), 1208.

(53) Li, J.; Han, T.; Wei, N.; Du, J.; Zhao, X., Three-dimensionally ordered macroporous (3DOM) gold-nanoparticle-doped titanium dioxide (GTD) photonic crystals modified electrodes for hydrogen peroxide biosensor. *Biosensors and Bioelectronics* **2009,** *25* (4), 773-777.

(54) Kim, O.-H.; Cho, Y.-H.; Kang, S. H.; Park, H.-Y.; Kim, M.; Lim, J. W.; Chung, D. Y.; Lee, M. J.; Choe, H.; Sung, Y.-E., Ordered macroporous platinum electrode and enhanced mass transfer in fuel cells using inverse opal structure. *Nat Commun* **2013,** *4*.

(55) Wu, M.; Li, Y.; Deng, Z.; Su, B. L., Three-Dimensionally Ordered Macroporous Titania with Structural and Photonic Effects for Enhanced Photocatalytic Efficiency. *Chemsuschem* **2011,** *4* (10), 1481-1488.

(56) Sorensen, E. M.; Barry, S. J.; Jung, H. K.; Rondinelli, J. R.; Vaughey, J. T.; Poeppelmeier, K. R., Three-dimensionally ordered macroporous Li4Ti5O12: Effect of wall structure on electrochemical properties. *Chem. Mater.* **2006,** *18* (2), 482-489.

(57) Quan-Zhou, W.; Qiang, Y.; Ju-Fang, L.; Jing-Heng, D.; Yu-Guang, L., Fully Accessible Ag Nanoparticles within Three-dimensionally Ordered Macroporous SiO2. *Chin. J. Chem.* **2005,** *23* (6), 689-692.

(58) Wang, L.-J.; Fan, H.-L.; Shangguan, J.; Croiset, E.; Chen, Z.; Wang, H.; Mi, J., Design of a Sorbent to Enhance Reactive Adsorption of Hydrogen Sulfide. *ACS Appl. Mater. Interfaces* **2014,** *6* (23), 21167-21177.

(59) Fan, H.-L.; Sun, T.; Zhao, Y.-P.; Shangguan, J.; Lin, J.-Y., Three-Dimensionally Ordered Macroporous Iron Oxide for Removal of H2S at Medium Temperatures. *Environmental Science & Technology* **2013,** *47* (9), 4859-4865.

(60) Chen, X.; Li, Z.; Ye, J.; Zou, Z., Forced Impregnation Approach to Fabrication of Large-Area, Three-Dimensionally Ordered Macroporous Metal Oxides. *Chem. Mater.* **2010,** *22* (12), 3583-3585.

(61) Nagpal, P.; Josephson, D. P.; Denny, N. R.; DeWilde, J.; Norris, D. J.; Stein, A., Fabrication of carbon/refractory metal nanocomposites as thermally stable metallic photonic crystals. *J. Mater. Chem.* **2011,** *21* (29), 10836-10843.

(62) Ergang, N. S.; Lytle, J. C.; Lee, K. T.; Oh, S. M.; Smyrl, W. H.; Stein, A., Photonic Crystal Structures as a Basis for a Three-Dimensionally Interpenetrating Electrochemical-Cell System. *Adv. Mater.* **2006,** *18* (13), 1750-1753.

(63) Choi, W.; Termin, A.; Hoffmann, M. R., The Role of Metal Ion Dopants in Quantum-Sized TiO2: Correlation between Photoreactivity and Charge Carrier Recombination Dynamics. *The Journal of Physical Chemistry* **1994,** *98* (51), 13669-13679.

(64) Colmenares, J. C.; Aramendía, M. A.; Marinas, A.; Marinas, J. M.; Urbano, F. J., Synthesis, characterization and photocatalytic activity of different metal-doped titania systems. *Applied Catalysis A: General* **2006,** *306* (0), 120-127.

(65) Ranjit, K. T.; Viswanathan, B., Photocatalytic reduction of nitrite and nitrate ions over doped TiO2 catalysts. *Journal of Photochemistry and Photobiology A: Chemistry* **1997,** *107* (1–3), 215-220.

(66) Xu, A.-W.; Gao, Y.; Liu, H.-Q., The Preparation, Characterization, and their Photocatalytic Activities of Rare-Earth-Doped TiO2 Nanoparticles. *J. Catal.* **2002,** *207* (2), 151-157.

(67) Choi, Y.; Umebayashi, T.; Yoshikawa, M., Fabrication and characterization of C-doped anatase TiO2 photocatalysts. *J. Mater. Sci.* **2004,** *39* (5), 1837-1839.

(68) Burda, C.; Lou, Y.; Chen, X.; Samia, A. C. S.; Stout, J.; Gole, J. L., Enhanced Nitrogen Doping in TiO2 Nanoparticles. *Nano Lett.* **2003,** *3* (8), 1049-1051.

(69) Ho, W.; Yu, J. C.; Lee, S., Low-temperature hydrothermal synthesis of S-doped TiO2 with visible light photocatalytic activity. *J. Solid State Chem.* **2006,** *179* (4), 1171-1176.

(70) Yu, J. C.; Yu; Ho; Jiang; Zhang, Effects of F- Doping on the Photocatalytic Activity and Microstructures of Nanocrystalline TiO2 Powders. *Chem. Mater.* **2002,** *14* (9), 3808-3816.

(71) Sun, W. T.; Yu, Y.; Pan, H. Y.; Gao, X. F.; Chen, Q.; Peng, L. M., CdS quantum dots sensitized TiO2 nanotube-array photoelectrodes. *J. Am. Chem. Soc.* **2008,** *130* (4), 1124-+.

(72) Bessekhouad, Y.; Robert, D.; Weber, J. V., Photocatalytic activity of Cu2O/TiO2, Bi2O3/TiO2 and ZnMn2O4/TiO2 heterojunctions. *Catal. Today* **2005,** *101* (3–4), 315-321.

(73) Brahimi, R.; Bessekhouad, Y.; Bouguelia, A.; Trari, M., Improvement of eosin visible light degradation using PbS-sensititized TiO2. *Journal of Photochemistry and Photobiology A: Chemistry* **2008,** *194* (2–3), 173-180.

(74) Liu, Y.; Ji, G.; Dastageer, M. A.; Zhu, L.; Wang, J.; Zhang, B.; Chang, X.; Gondal, M. A., Highly-active direct Z-scheme Si/TiO2 photocatalyst for boosted CO2 reduction into value-added methanol. *RSC Adv.* **2014,** *4* (100), 56961-56969.

(75) Yu, J.; Wang, S.; Low, J.; Xiao, W., Enhanced photocatalytic performance of direct Z-scheme g-C3N4-TiO2 photocatalysts for the decomposition of formaldehyde in air. *Phys. Chem. Chem. Phys.* **2013,** *15* (39), 16883-16890.

(76) Fu, J.; Cao, S.; Yu, J., Dual Z-scheme charge transfer in TiO2–Ag–Cu2O composite for enhanced photocatalytic hydrogen generation. *Journal of Materiomics* **2015,** *1* (2), 124-133.

(77) Sayama, K.; Mukasa, K.; Abe, R.; Abe, Y.; Arakawa, H., Stoichiometric water splitting into H2 and O2 using a mixture of two different photocatalysts and an IO3-/I- shuttle redox mediator under visible light irradiation. *Chem Commun* **2001,** (23), 2416-2417.

(78) Nazeeruddin, M. K.; Splivallo, R.; Liska, P.; Comte, P.; Gratzel, M., A swift dye uptake procedure for dye sensitized solar cells. *Chem Commun* **2003,** (12), 1456-1457.

(79) Senevirathna, M. K. I.; Pitigala, P. K. D. D. P.; Tennakone, K., Water photoreduction with Cu2O quantum dots on TiO2 nano-particles. *Journal of Photochemistry and Photobiology A: Chemistry* **2005,** *171* (3), 257-259.

(80) Kongkanand, A.; Tvrdy, K.; Takechi, K.; Kuno, M.; Kamat, P. V., Quantum Dot Solar Cells. Tuning Photoresponse through Size and Shape Control of CdSe−TiO2 Architecture. *J. Am. Chem. Soc.* **2008,** *130* (12), 4007-4015.

(81) Subramanian, V.; Wolf, E.; Kamat, P. V., Semiconductor−Metal Composite Nanostructures. To What Extent Do Metal Nanoparticles Improve the Photocatalytic Activity of TiO2 Films? *The Journal of Physical Chemistry B* **2001,** *105* (46), 11439-11446.

(82) Arabatzis, I. M.; Stergiopoulos, T.; Bernard, M. C.; Labou, D.; Neophytides, S. G.; Falaras, P., Silver-modified titanium dioxide thin films for efficient photodegradation of methyl orange. *Appl. Catal., B* **2003,** *42* (2), 187-201.

(83) Osterloh, F. E., Inorganic Materials as Catalysts for Photochemical Splitting of Water. *Chem. Mater.* **2007,** *20* (1), 35-54.

(84) Hoffmann, M. R.; Martin, S. T.; Choi, W.; Bahnemann, D. W., Environmental Applications of Semiconductor Photocatalysis. *Chem. Rev.* **1995,** *95* (1), 69-96.

(85) Murzin, D. Y.; Salmi, T., *Catalytic Kinetics*. Elsevier Science: 2005.

(86) Davis, A. P.; Huang, C. P., The photocatalytic oxidation of sulfur-containing organic compounds using cadmium sulfide and the effect on CdS photocorrosion. *Water Res.* **1991,** *25* (10), 1273-1278.

(87) Wu, L.; Yu, J. C.; Fu, X., Characterization and photocatalytic mechanism of nanosized CdS coupled TiO2 nanocrystals under visible light irradiation. *J. Mol. Catal. A: Chem.* **2006,** *244* (1–2), 25-32.

(88) Adeli, B.; Taghipour, F., A Review of Synthesis Techniques for Gallium-Zinc Oxynitride Solar-Activated Photocatalyst for Water Splitting. *ECS Journal of Solid State Science and Technology* **2013,** *2* (7), Q118-Q126.

(89) Sutton, A. P., *Electronic Structure of Materials*. Clarendon Press: 1993.

(90) Levinson, J.; Shepherd, F. R.; Scanlon, P. J.; Westwood, W. D.; Este, G.; Rider, M., Conductivity behavior in polycrystalline semiconductor thin film transistors. *J. Appl. Phys.* **1982,** *53* (2), 1193-1202.

(91) Zou, Z.; Ye, J.; Sayama, K.; Arakawa, H., Direct splitting of water under visible light irradiation with an oxide semiconductor photocatalyst. *Nature* **2001,** *414* (6864), 625-627.

(92) Parlett, C. M. A.; Wilson, K.; Lee, A. F., Hierarchical porous materials: catalytic applications. *Chem. Soc. Rev.* **2013,** *(pre-print)*, -.

(93) Zhu, J.; Zäch, M., Nanostructured materials for photocatalytic hydrogen production. *Current Opinion in Colloid \& Interface Science* **2009,** *14* (4), 260 - 269.

(94) Qu, Y.; Duan, X., Progress, challenge and perspective of heterogeneous photocatalysts. *Chem. Soc. Rev.* **2013,** *(pre-print)*, -.

(95) Daneshvar, N.; Salari, D.; Khataee, A. R., Photocatalytic degradation of azo dye acid red 14 in water on ZnO as an alternative catalyst to TiO2. *Journal of Photochemistry and Photobiology A: Chemistry* **2004,** *162* (2–3), 317-322.

(96) Kumar, R.; Kumar, G.; Umar, A., ZnO nano-mushrooms for photocatalytic degradation of methyl orange. *Mater. Lett.* **2013,** *97* (0), 100-103.

(97) Kormann, C.; Bahnemann, D. W.; Hoffmann, M. R., Environmental Photochemistry - Is Iron-Oxide (Hematite) an Active Photocatalyst - a Comparative-Study - Alpha-Fe2o3, Zno, Tio2. *Journal of Photochemistry and Photobiology a-Chemistry* **1989,** *48* (1), 161-169.

(98) Baltrusaitis, J.; Hu, Y.-S.; McFarland, E. W.; Hellman, A., Photoelectrochemical Hydrogen Production on α-Fe2O3 (0001): Insights from Theory and Experiments. *Chemsuschem* **2014,** *7* (1), 162-171.

(99) Sayama, K.; Yoshida, R.; Kusama, H.; Okabe, K.; Abe, Y.; Arakawa, H., Photocatalytic decomposition of water into H2 and O2 by a two-step photoexcitation reaction using a WO3 suspension catalyst and an Fe3+/Fe2+ redox system. *Chem. Phys. Lett.* **1997,** *277* (4), 387-391.

(100) Guo, Y.; Quan, X.; Lu, N.; Zhao, H.; Chen, S., High Photocatalytic Capability of Self-Assembled Nanoporous WO3 with Preferential Orientation of (002) Planes. *Environmental Science & Technology* **2007,** *41* (12), 4422-4427.

(101) Konta, R.; Ishii, T.; Kato, H.; Kudo, A., Photocatalytic Activities of Noble Metal Ion Doped SrTiO3 under Visible Light Irradiation. *The Journal of Physical Chemistry B* **2004,** *108* (26), 8992-8995.

(102) Yu, H.; Wang, J.; Yan, S.; Yu, T.; Zou, Z., Elements doping to expand the light response of SrTiO3. *Journal of Photochemistry and Photobiology A: Chemistry* **2014,** *275* (0), 65-71.

(103) Zhou, L.; Wang, W.; Liu, S.; Zhang, L.; Xu, H.; Zhu, W., A sonochemical route to visible-light-driven high-activity BiVO4 photocatalyst. *J. Mol. Catal. A: Chem.* **2006,** *252* (1–2), 120-124.

(104) Nagabhushana, G. P.; Nagaraju, G.; Chandrappa, G. T., Synthesis of bismuth vanadate: its application in H2 evolution and sunlight-driven photodegradation. *J. Mater. Chem. A* **2013,** *1* (2), 388-394.

(105) Wachs, I. E.; Phivilay, S. P.; Roberts, C. A., Reporting of Reactivity for Heterogeneous Photocatalysis. *ACS Catalysis* **2013,** *3* (11), 2606-2611.

(106) Kudo, A.; Miseki, Y., Heterogeneous photocatalyst materials for water splitting. *Chem. Soc. Rev.* **2009,** *38* (1), 253-278.

(107) Jing, D.; Guo, L., A Novel Method for the Preparation of a Highly Stable and Active CdS Photocatalyst with a Special Surface Nanostructure. *The Journal of Physical Chemistry B* **2006,** *110* (23), 11139-11145.

(108) Hu, Y.; Gao, X.; Yu, L.; Wang, Y.; Ning, J.; Xu, S.; Lou, X. W., Carbon-Coated CdS Petalous Nanostructures with Enhanced Photostability and Photocatalytic Activity. *Angew. Chem., Int. Ed.* **2013,** *52* (21), 5636-5639.

(109) Reber, J. F.; Meier, K., Photochemical production of hydrogen with zinc sulfide suspensions. *The Journal of Physical Chemistry* **1984,** *88* (24), 5903-5913.

(110) Rajabi, H. R.; Khani, O.; Shamsipur, M.; Vatanpour, V., High-performance pure and Fe3+-ion doped ZnS quantum dots as green nanophotocatalysts for the removal of malachite green under UV-light irradiation. *J. Hazard. Mater.* **2013,** *250–251* (0), 370-378.

(111) James, D.; Zubkov, T., Photocatalytic properties of free and oxide-supported MoS2 and WS2 nanoparticles synthesized without surfactants. *Journal of Photochemistry and Photobiology A: Chemistry* **2013,** *262* (0), 45-51.

(112) Yan, S. C.; Li, Z. S.; Zou, Z. G., Photodegradation Performance of g-C3N4 Fabricated by Directly Heating Melamine. *Langmuir* **2009,** *25* (17), 10397-10401.

(113) Bai, X.; Wang, L.; Zong, R.; Zhu, Y., Photocatalytic Activity Enhanced via g-C3N4 Nanoplates to Nanorods. *The Journal of Physical Chemistry C* **2013,** *117* (19), 9952-9961.

(114) Gogate, P. R.; Pandit, A. B., A review of imperative technologies for waste water treatment I: oxidation technologies at ambient conditions. *Advances in Environmental Research* **2004,** *8* (3–4), 501-551.

(115) Pinaud, B. A.; Benck, J. D.; Seitz, L. C.; Forman, A. J.; Chen, Z.; Deutsch, T. G.; James, B. D.; Baum, K. N.; Baum, G. N.; Ardo, S.; Wang, H.; Miller, E.; Jaramillo, T. F., Technical and

economic feasibility of centralized facilities for solar hydrogen production via photocatalysis and photoelectrochemistry. *Energy Environ. Sci.* **2013,** *6* (7), 1983-2002.

(116) Kanakaraju, D.; Glass, B.; Oelgemöller, M., Titanium dioxide photocatalysis for pharmaceutical waste water treatment. *Environ. Chem. Lett.* **2014,** *12* (1), 27-47.

(117) Zhao, W.; Ma, W.; Chen, C.; Zhao, J.; Shuai, Z., Efficient Degradation of Toxic Organic Pollutants with Ni2O3/TiO2-xBx under Visible Irradiation. *J. Am. Chem. Soc.* **2004,** *126* (15), 4782-4783.

(118) Kabra, K.; Chaudhary, R.; Sawhney, R. L., Treatment of Hazardous Organic and Inorganic Compounds through Aqueous-Phase Photocatalysis: A Review. *Ind. Eng. Chem. Res.* **2004,** *43* (24), 7683-7696.

(119) Herrmann, J.-M., Heterogeneous photocatalysis: fundamentals and applications to the removal of various types of aqueous pollutants. *Catal. Today* **1999,** *53* (1), 115-129.

(120) Zollinger, H., *Color Chemistry: Syntheses, Properties, and Applications of Organic Dyes and Pigments*. Wiley: 2003.

(121) Lachheb, H.; Puzenat, E.; Houas, A.; Ksibi, M.; Elaloui, E.; Guillard, C.; Herrmann, J.-M., Photocatalytic degradation of various types of dyes (Alizarin S, Crocein Orange G, Methyl Red, Congo Red, Methylene Blue) in water by UV-irradiated titania. *Appl. Catal., B* **2002,** *39* (1), 75-90.

(122) Houas, A.; Lachheb, H.; Ksibi, M.; Elaloui, E.; Guillard, C.; Herrmann, J.-M., Photocatalytic degradation pathway of methylene blue in water. *Appl. Catal., B* **2001,** *31* (2), 145-157.

(123) Kannan, N.; Sundaram, M. M., Kinetics and mechanism of removal of methylene blue by adsorption on various carbons—a comparative study. *Dyes Pigm.* **2001,** *51* (1), 25-40.

(124) Haile, S. Fuel Cells for Sustainable Energy --- Science meets social responsibility. http://addis.caltech.edu/research/FCs%20for%20sustain%20energy.html 2013. (accessed August 7).

(125) Jacobsson, T. J.; Fjallstrom, V.; Edoff, M.; Edvinsson, T., Sustainable solar hydrogen production: from photoelectrochemical cells to PV-electrolyzers and back again. *Energy Environ. Sci.* **2014,** *7* (7), 2056-2070.

(126) Seger, B.; Lu, G. Q.; Wang, L. Z., Electrical power and hydrogen production from a photo-fuel cell using formic acid and other single-carbon organics. *J. Mater. Chem.* **2012,** *22* (21), 10709-10715.

(127) Li, K.; Xu, Y.; He, Y.; Yang, C.; Wang, Y.; Jia, J., Photocatalytic Fuel Cell (PFC) and Dye Self-Photosensitization Photocatalytic Fuel Cell (DSPFC) with BiOCl/Ti Photoanode under UV and Visible Light Irradiation. *Environmental Science & Technology* **2013,** *47* (7), 3490-3497.

(128) Wang, B.; Zhang, H.; Lu, X.-Y.; Xuan, J.; Leung, M. K. H., Solar photocatalytic fuel cell using CdS–TiO2 photoanode and air-breathing cathode for waste water treatment and simultaneous electricity production. *Chemical Engineering Journal* **2014,** *253*, 174-182.

(129) Antoniadou, M.; Kondarides, D. I.; Labou, D.; Neophytides, S.; Lianos, P., An efficient photoelectrochemical cell functioning in the presence of organic wastes. *Sol. Energy Mater. Sol. Cells* **2010,** *94* (3), 592-597.

(130) Li, K.; Zhang, H.; Tang, T.; Xu, Y.; Ying, D.; Wang, Y.; Jia, J., Optimization and application of TiO2/Ti–Pt photo fuel cell (PFC) to effectively generate electricity and degrade organic pollutants simultaneously. *Water Res.* **2014,** *62*, 1-10.

(131) Zhang, J.; Dong, S.; Zhang, X.; Zhu, S.; Zhou, D.; Crittenden, J. C., Photocatalytic removal organic matter and bacteria simultaneously from real WWTP effluent with power generation concomitantly: Using an ErAlZnO photo-anode. *Sep. Purif. Technol.* **2018,** *191*, 101-107.

(132) Wang, D.; Li, Y.; Li Puma, G.; Wang, C.; Wang, P.; Zhang, W.; Wang, Q., Dye-sensitized photoelectrochemical cell on plasmonic Ag/AgCl @ chiral TiO2 nanofibers for treatment of urban waste water effluents, with simultaneous production of hydrogen and electricity. *Appl. Catal., B* **2015,** *168–169*, 25-32.

(133) Wang, X.; Feng, Y. J.; Lee, H., Electricity production from beer brewery waste water using single chamber microbial fuel cell. *Water Sci. Technol.* **2008,** *57* (7), 1117-1121.

(134) Liu, Y.; Yang, Y., Recent Progress of TiO2-Based Anodes for Li Ion Batteries. *J Nanomater* **2016,** *2016*, 15.

(135) Etacheri, V.; Marom, R.; Elazari, R.; Salitra, G.; Aurbach, D., Challenges in the development of advanced Li-ion batteries: a review. *Energy Environ. Sci.* **2011,** *4* (9), 3243-3262.

(136) Omar, N.; Daowd, M.; Van den Bossche, P.; Hegazy, O.; Smekens, J.; Coosemans, T.; Van Mierlo, J., *Rechargeable Energy Storage Systems for Plug-in Hybrid Electric Vehicles—Assessment of Electrical Characteristics*. 2012; Vol. 5, p 2952-2988.

(137) Yanyan, Z.; Yuxin, T.; Wenlong, L.; Xiaodong, C., Nanostructured TiO2-Based Anode Materials for High-Performance Rechargeable Lithium-Ion Batteries. *ChemNanoMat* **2016,** *2* (8), 764-775.

(138) Pimenta, M. A.; Dresselhaus, G.; Dresselhaus, M. S.; Cancado, L. G.; Jorio, A.; Saito, R., Studying disorder in graphite-based systems by Raman spectroscopy. *Phys. Chem. Chem. Phys.* **2007,** *9* (11), 1276-1290.

(139) Kortüm, G.; Braun, W.; Herzog, G., Principles and Techniques of Diffuse-Reflectance Spectroscopy. *Angewandte Chemie International Edition in English* **1963,** *2* (7), 333-341.

(140) Tauc, J.; Grigorovici, R.; Vancu, A., Optical Properties and Electronic Structure of Amorphous Germanium. *physica status solidi (b)* **1966,** *15* (2), 627-637.

(141) Brunauer, S.; Emmett, P. H.; Teller, E., Adsorption of Gases in Multimolecular Layers. *J. Am. Chem. Soc.* **1938,** *60* (2), 309-319.

(142) Bard, A. J.; Faulkner, L. R., *Electrochemical Methods; Fundamentals and Applications*. Wiley Interscience Publications: 2000.

(143) Clark, B. J.; Frost, T.; Russell, A.; Group, U. S., *UV Spectroscopy: Techniques, Instrumentation and Data Handling*. Springer: 1993.

(144) Hatton, B.; Mishchenko, L.; Davis, S.; Sandhage, K. H.; Aizenberg, J., Assembly of large-area, highly ordered, crack-free inverse opal films. *Proceedings of the National Academy of Sciences* **2010,** *107* (23), 10354-10359.

(145) Cai, Z.; Liu, Y. J.; Teng, J.; Lu, X., Fabrication of Large Domain Crack-Free Colloidal Crystal Heterostructures with Superposition Bandgaps Using Hydrophobic Polystyrene Spheres. *ACS Appl. Mater. Interfaces* **2012,** *4* (10), 5562-5569.

(146) Cai, Z.; Teng, J.; Xiong, Z.; Li, Y.; Li, Q.; Lu, X.; Zhao, X. S., Fabrication of TiO2 Binary Inverse Opals without Overlayers via the Sandwich-Vacuum Infiltration of Precursor. *Langmuir* **2011,** *27* (8), 5157-5164.

(147) Bruce, P. G.; Scrosati, B.; Tarascon, J.-M., Nanomaterials for Rechargeable Lithium Batteries. *Angew. Chem., Int. Ed.* **2008,** *47* (16), 2930-2946.

(148) Nathan, A.; Ahnood, A.; Cole, M. T.; Sungsik, L.; Suzuki, Y.; Hiralal, P.; Bonaccorso, F.; Hasan, T.; Garcia-Gancedo, L.; Dyadyusha, A.; Haque, S.; Andrew, P.; Hofmann, S.; Moultrie, J.; Daping, C.; Flewitt, A. J.; Ferrari, A. C.; Kelly, M. J.; Robertson, J.; Amaratunga, G.; Milne, W. I., Flexible Electronics: The Next Ubiquitous Platform. *Proceedings of the IEEE* **2012,** *100* (Special Centennial Issue), 1486-1517.

(149) Lee, H. M.; Choi, S.-Y.; Jung, A.; Ko, S. H., Highly Conductive Aluminum Textile and Paper for Flexible and Wearable Electronics. *Angew. Chem.* **2013,** *125* (30), 7872-7877.

(150) Yeo, J.; Kim, G.; Hong, S.; Kim, M. S.; Kim, D.; Lee, J.; Lee, H. B.; Kwon, J.; Suh, Y. D.; Kang, H. W.; Sung, H. J.; Choi, J.-H.; Hong, W.-H.; Ko, J. M.; Lee, S.-H.; Choa, S.-H.; Ko, S. H., Flexible supercapacitor fabrication by room temperature rapid laser processing of roll-to-roll printed metal nanoparticle ink for wearable electronics application. *J. Power Sources* **2014,** *246*, 562-568.

(151) Lam Po Tang, S., Recent developments in flexible wearable electronics for monitoring applications. *Transactions of the Institute of Measurement and Control* **2007,** *29* (3-4), 283-300.

(152) Hassan, F. M.; Batmaz, R.; Li, J.; Wang, X.; Xiao, X.; Yu, A.; Chen, Z., Evidence of covalent synergy in silicon-sulfur-graphene yielding highly efficient and long-life lithium-ion batteries. *Nat Commun* **2015,** *6*, 8597.

(153) Feng, K.; Ahn, W.; Lui, G.; Park, H. W.; Kashkooli, A. G.; Jiang, G.; Wang, X.; Xiao, X.; Chen, Z., Implementing an in-situ carbon network in Si/reduced graphene oxide for high performance lithium-ion battery anodes. *Nano Energy* **2016,** *19*, 187-197.

(154) Liao, J.-Y.; Xiao, X.; Higgins, D.; Lee, D.; Hassan, F.; Chen, Z., Hierarchical Li4Ti5O12-TiO2 composite microsphere consisting of nanocrystals for high power Li-ion batteries. *Electrochim. Acta* **2013,** *108*, 104-111.

(155) Zhu, G.-N.; Wang, Y.-G.; Xia, Y.-Y., Ti-based compounds as anode materials for Li-ion batteries. *Energy Environ. Sci.* **2012,** *5* (5), 6652-6667.

(156) Liu, H.; Li, W.; Shen, D.; Zhao, D.; Wang, G., Graphitic Carbon Conformal Coating of Mesoporous TiO2 Hollow Spheres for High-Performance Lithium Ion Battery Anodes. *J. Am. Chem. Soc.* **2015,** *137* (40), 13161-13166.

(157) Rai, A. K.; Anh, L. T.; Gim, J.; Mathew, V.; Kang, J.; Paul, B. J.; Song, J.; Kim, J., Simple synthesis and particle size effects of TiO2 nanoparticle anodes for rechargeable lithium ion batteries. *Electrochim. Acta* **2013,** *90*, 112-118.

(158) Myung, S.-T.; Kikuchi, M.; Yoon, C. S.; Yashiro, H.; Kim, S.-J.; Sun, Y.-K.; Scrosati, B., Black anatase titania enabling ultra high cycling rates for rechargeable lithium batteries. *Energy Environ. Sci.* **2013,** *6* (9), 2609-2614.

(159) Goriparti, S.; Miele, E.; Prato, M.; Scarpellini, A.; Marras, S.; Monaco, S.; Toma, A.; Messina, G. C.; Alabastri, A.; Angelis, F. D.; Manna, L.; Capiglia, C.; Zaccaria, R. P., Direct Synthesis of Carbon-Doped TiO2–Bronze Nanowires as Anode Materials for High Performance Lithium-Ion Batteries. *ACS Appl. Mater. Interfaces* **2015,** *7*, 25139.

(160) Ye, J.; Baumgaertel, A. C.; Wang, Y. M.; Biener, J.; Biener, M. M., Structural Optimization of 3D Porous Electrodes for High-Rate Performance Lithium Ion Batteries. *ACS Nano* **2015,** *9* (2), 2194-2202.

(161) Huang, X.; Chen, J.; Lu, Z.; Yu, H.; Yan, Q.; Hng, H. H., Carbon inverse opal entrapped with electrode active nanoparticles as high-performance anode for lithium-ion batteries. *Sci Rep-Uk* **2013,** *3*, 2317.

(162) Deng, M.-J.; Song, C.-Z.; Ho, P.-J.; Wang, C.-C.; Chen, J.-M.; Lu, K.-T., Three-dimensionally ordered macroporous Cu2O/Ni inverse opal electrodes for electrochemical supercapacitors. *Phys. Chem. Chem. Phys.* **2013,** *15* (20), 7479-7483.

(163) Zhang, H.; Yu, X.; Braun, P. V., Three-dimensional bicontinuous ultrafast-charge and -discharge bulk battery electrodes. *Nat Nano* **2011,** *6* (5), 277-281.

(164) Sorensen, E. M.; Barry, S. J.; Jung, H. K.; Rondinelli, J. R.; Vaughey, J. T.; Poeppelmeier, K. R., Three-dimensionally ordered macroporous Li4Ti5O12: Effect of wall structure on electrochemical properties (vol 18, pg 482, 2006). *Chem. Mater.* **2006,** *18* (6), 1713-1713.

(165) Yang, C.; Zhou, M.; Xu, Q., Three-dimensional ordered macroporous MnO2/carbon nanocomposites as high-performance electrodes for asymmetric supercapacitors. *Phys. Chem. Chem. Phys.* **2013,** *15* (45), 19730-19740.

(166) Dominko, R.; Gaberscek, M.; Bele, M.; Mihailovic, D.; Jamnik, J., Carbon nanocoatings on active materials for Li-ion batteries. *J. Eur. Ceram. Soc.* **2007,** *27* (2–3), 909-913.

(167) Park, S.-J.; Kim, H.; Kim, Y.-J.; Lee, H., Preparation of carbon-coated TiO2 nanostructures for lithium-ion batteries. *Electrochim. Acta* **2011,** *56* (15), 5355-5362.

(168) Kavan, L.; Zukalová, M.; Kalbáč, M.; Graetzel, M., Lithium Insertion into Anatase Inverse Opal. *J. Electrochem. Soc.* **2004,** *151* (8), A1301-A1307.

(169) Xu, Y.; Memarzadeh Lotfabad, E.; Wang, H.; Farbod, B.; Xu, Z.; Kohandehghan, A.; Mitlin, D., Nanocrystalline anatase TiO2: a new anode material for rechargeable sodium ion batteries. *Chem Commun* **2013,** *49* (79), 8973-8975.

(170) Yu, H.; Zhu, C.; Zhang, K.; Chen, Y.; Li, C.; Gao, P.; Yang, P.; Ouyang, Q., Three-dimensional hierarchical MoS2 nanoflake array/carbon cloth as high-performance flexible lithium-ion battery anodes. *J. Mater. Chem. A* **2014,** *2* (13), 4551-4557.

(171) Wagemaker, M.; Borghols, W. J. H.; Mulder, F. M., Large Impact of Particle Size on Insertion Reactions. A Case for Anatase LixTiO2. *J. Am. Chem. Soc.* **2007,** *129* (14), 4323-4327.

(172) Padmanathan, N.; Selladurai, S., Controlled growth of spinel NiCo2O4 nanostructures on carbon cloth as a superior electrode for supercapacitors. *RSC Adv.* **2014,** *4* (16), 8341-8349.

(173) Ferrari, A. C.; Meyer, J. C.; Scardaci, V.; Casiraghi, C.; Lazzeri, M.; Mauri, F.; Piscanec, S.; Jiang, D.; Novoselov, K. S.; Roth, S.; Geim, A. K., Raman Spectrum of Graphene and Graphene Layers. *Phys. Rev. Lett.* **2006,** *97* (18), 187401.

(174) Yang, Y.; Ji, X.; Jing, M.; Hou, H.; Zhu, Y.; Fang, L.; Yang, X.; Chen, Q.; Banks, C. E., Carbon dots supported upon N-doped TiO2 nanorods applied into sodium and lithium ion batteries. *J. Mater. Chem. A* **2015,** *3* (10), 5648-5655.

(175) Wu, L.; Bresser, D.; Buchholz, D.; Passerini, S., Nanocrystalline TiO2(B) as Anode Material for Sodium-Ion Batteries. *J. Electrochem. Soc.* **2015,** *162* (2), A3052-A3058.

(176) Kavan, L.; Rathouský, J.; Grätzel, M.; Shklover, V.; Zukal, A., Surfactant-Templated TiO2 (Anatase): Characteristic Features of Lithium Insertion Electrochemistry in Organized Nanostructures. *The Journal of Physical Chemistry B* **2000,** *104* (50), 12012-12020.

(177) Augustyn, V.; Simon, P.; Dunn, B., Pseudocapacitive oxide materials for high-rate electrochemical energy storage. *Energy Environ. Sci.* **2014,** *7* (5), 1597-1614.

(178) Chen, Z.; Zhang, D.; Wang, X.; Jia, X.; Wei, F.; Li, H.; Lu, Y., High-Performance Energy-Storage Architectures from Carbon Nanotubes and Nanocrystal Building Blocks. *Adv. Mater.* **2012,** *24* (15), 2030-2036.

(179) Cheng, J.; Wang, B.; Xin, H. L.; Kim, C.; Nie, F.; Li, X.; Yang, G.; Huang, H., Conformal coating of TiO2 nanorods on a 3-D CNT scaffold by using a CNT film as a nanoreactor: a free-standing and binder-free Li-ion anode. *J. Mater. Chem. A* **2014,** *2* (8), 2701-2707.

(180) Hu, T.; Sun, X.; Sun, H.; Yu, M.; Lu, F.; Liu, C.; Lian, J., Flexible free-standing graphene–TiO2 hybrid paper for use as lithium ion battery anode materials. *Carbon* **2013,** *51*, 322-326.

(181) Liu, S.; Wang, Z.; Yu, C.; Wu, H. B.; Wang, G.; Dong, Q.; Qiu, J.; Eychmüller, A.; Lou, X. W., A Flexible TiO2(B)-Based Battery Electrode with Superior Power Rate and Ultralong Cycle Life. *Adv. Mater.* **2013,** *25* (25), 3462-3467.

(182) Lee, S.; Ha, J.; Choi, J.; Song, T.; Lee, J. W.; Paik, U., 3D Cross-Linked Nanoweb Architecture of Binder-Free TiO2 Electrodes for Lithium Ion Batteries. *ACS Appl. Mater. Interfaces* **2013,** *5* (22), 11525-11529.

(183) Tao, X. M., *Wearable Electronics and Photonics*. Woodhead Publishing: Cambridge, 2005.

(184) Zeng, W.; Shu, L.; Li, Q.; Chen, S.; Wang, F.; Tao, X.-M., Fiber-Based Wearable Electronics: A Review of Materials, Fabrication, Devices, and Applications. *Adv. Mater.* **2014,** *26* (31), 5310-5336.

(185) Stoppa, M.; Chiolerio, A., Wearable electronics and smart textiles: a critical review. *Sensors* **2014,** *14* (7), 11957-11992.

(186) Pu, X.; Li, L.; Song, H.; Du, C.; Zhao, Z.; Jiang, C.; Cao, G.; Hu, W.; Wang, Z. L., A Self-Charging Power Unit by Integration of a Textile Triboelectric Nanogenerator and a Flexible Lithium-Ion Battery for Wearable Electronics. *Adv. Mater.* **2015,** *27* (15), 2472-2478.

(187) Lee, Y.-H.; Kim, J.-S.; Noh, J.; Lee, I.; Kim, H. J.; Choi, S.; Seo, J.; Jeon, S.; Kim, T.-S.; Lee, J.-Y.; Choi, J. W., Wearable Textile Battery Rechargeable by Solar Energy. *Nano Lett.* **2013,** *13* (11), 5753-5761.

(188) Meng, Y.; Zhao, Y.; Hu, C.; Cheng, H.; Hu, Y.; Zhang, Z.; Shi, G.; Qu, L., All-Graphene Core-Sheath Microfibers for All-Solid-State, Stretchable Fibriform Supercapacitors and Wearable Electronic Textiles. *Adv. Mater.* **2013,** *25* (16), 2326-2331.

(189) Jost, K.; Stenger, D.; Perez, C. R.; McDonough, J. K.; Lian, K.; Gogotsi, Y.; Dion, G., Knitted and screen printed carbon-fiber supercapacitors for applications in wearable electronics. *Energy Environ. Sci.* **2013,** *6* (9), 2698-2705.

(190) Pan, S.; Yang, Z.; Chen, P.; Deng, J.; Li, H.; Peng, H., Wearable Solar Cells by Stacking Textile Electrodes. *Angew. Chem., Int. Ed.* **2014,** *53* (24), 6110-6114.

(191) Kim, B. J.; Kim, D. H.; Lee, Y.-Y.; Shin, H.-W.; Han, G. S.; Hong, J. S.; Mahmood, K.; Ahn, T. K.; Joo, Y.-C.; Hong, K. S.; Park, N.-G.; Lee, S.; Jung, H. S., Highly efficient and bending durable perovskite solar cells: toward a wearable power source. *Energy Environ. Sci.* **2015,** *8* (3), 916-921.

(192) Leonov, V., Thermoelectric Energy Harvesting of Human Body Heat for Wearable Sensors. *IEEE Sensors Journal* **2013,** *13* (6), 2284-2291.

(193) Kim, S. J.; We, J. H.; Cho, B. J., A wearable thermoelectric generator fabricated on a glass fabric. *Energy Environ. Sci.* **2014,** *7* (6), 1959-1965.

(194) Fuh, Y.-K.; Ye, J.-C.; Chen, P.-C.; Ho, H.-C.; Huang, Z.-M., Hybrid Energy Harvester Consisting of Piezoelectric Fibers with Largely Enhanced 20 V for Wearable and Muscle-Driven Applications. *ACS Appl. Mater. Interfaces* **2015,** *7* (31), 16923-16931.

(195) Zhang, M.; Gao, T.; Wang, J.; Liao, J.; Qiu, Y.; Yang, Q.; Xue, H.; Shi, Z.; Zhao, Y.; Xiong, Z.; Chen, L., A hybrid fibers based wearable fabric piezoelectric nanogenerator for energy harvesting application. *Nano Energy* **2015,** *13*, 298-305.

(196) Wang, S.; Lin, L.; Wang, Z. L., Nanoscale Triboelectric-Effect-Enabled Energy Conversion for Sustainably Powering Portable Electronics. *Nano Lett.* **2012,** *12* (12), 6339-6346.

(197) Seung, W.; Gupta, M. K.; Lee, K. Y.; Shin, K.-S.; Lee, J.-H.; Kim, T. Y.; Kim, S.; Lin, J.; Kim, J. H.; Kim, S.-W., Nanopatterned Textile-Based Wearable Triboelectric Nanogenerator. *ACS Nano* **2015,** *9* (4), 3501-3509.

(198) Sonune, A.; Ghate, R., Developments in waste water treatment methods. *Desalination* **2004,** *167*, 55-63.

(199) Marco, A.; Esplugas, S.; Saum, G., How and why combine chemical and biological processes for waste water treatment. *Water Sci. Technol.* **1997,** *35* (4), 321-327.

(200) Henze, M.; Harremoes, P.; la Cour Jansen, J.; Arvin, E., *Waste water treatment: biological and chemical processes*. Springer Science & Business Media: 2001.

(201) Lin, S. H.; Lai, C. L., Kinetic characteristics of textile waste water ozonation in fluidized and fixed activated carbon beds. *Water Res.* **2000,** *34* (3), 763-772.

(202) Litter, M. I., Introduction to Photochemical Advanced Oxidation Processes for Water Treatment. In *Environmental Photochemistry Part II*, Boule, P.; Bahnemann, D. W.; Robertson, P. K. J., Eds. Springer Berlin Heidelberg: Berlin, Heidelberg, 2005; pp 325-366.

(203) Lee, H.; Choi, T. K.; Lee, Y. B.; Cho, H. R.; Ghaffari, R.; Wang, L.; Choi, H. J.; Chung, T. D.; Lu, N.; Hyeon, T.; Choi, S. H.; Kim, D.-H., A graphene-based electrochemical device with thermoresponsive microneedles for diabetes monitoring and therapy. *Nat Nano* **2016,** *advance online publication*.

(204) Falk, M.; Pankratov, D.; Lindh, L.; Arnebrant, T.; Shleev, S., Miniature Direct Electron Transfer Based Enzymatic Fuel Cell Operating in Human Sweat and Saliva. *Fuel Cells* **2014,** *14* (6), 1050-1056.

(205) Jia, W.; Wang, X.; Imani, S.; Bandodkar, A. J.; Ramirez, J.; Mercier, P. P.; Wang, J., Wearable textile biofuel cells for powering electronics. *J. Mater. Chem. A* **2014,** *2* (43), 18184-18189.

(206) Jia, W.; Valdés-Ramírez, G.; Bandodkar, A. J.; Windmiller, J. R.; Wang, J., Epidermal Biofuel Cells: Energy Harvesting from Human Perspiration. *Angew. Chem., Int. Ed.* **2013,** *52* (28), 7233-7236.

(207) Logan, B. E., *Microbial Fuel Cells*. Wiley: 2008.

(208) Chen, Z.; Higgins, D.; Yu, A.; Zhang, L.; Zhang, J., A review on non-precious metal electrocatalysts for PEM fuel cells. *Energy Environ. Sci.* **2011,** *4* (9), 3167-3192.

(209) Higgins, D.; Zamani, P.; Yu, A.; Chen, Z., The application of graphene and its composites in oxygen reduction electrocatalysis: a perspective and review of recent progress. *Energy Environ. Sci.* **2016,** *9* (2), 357-390.

(210) Wu, T.; Zhou, H. M.; Xia, B. Y.; Xiao, P.; Yan, Y.; Xie, M. S.; Wang, X., Facile Synthesis of 3 D Platinum Dendrites with a Clean Surface as Highly Stable Electrocatalysts. *ChemCatChem* **2014,** *6* (6), 1538-1542.

(211) Wang, R.; Higgins, D. C.; Hoque, M. A.; Lee, D.; Hassan, F.; Chen, Z., Controlled Growth of Platinum Nanowire Arrays on Sulfur Doped Graphene as High Performance Electrocatalyst. *Sci Rep-Uk* **2013,** *3*, 2431.

(212) Ryan, S. H.; Drew, H.; Zhongwei, C., Tin-oxide-coated single-walled carbon nanotube bundles supporting platinum electrocatalysts for direct ethanol fuel cells. *Nanotechnology* **2010,** *21* (16), 165705.

(213) Li, W.; Wu, J.; Higgins, D. C.; Choi, J.-Y.; Chen, Z., Determination of Iron Active Sites in Pyrolyzed Iron-Based Catalysts for the Oxygen Reduction Reaction. *ACS Catalysis* **2012,** *2* (12), 2761-2768.

(214) Higgins, D. C.; Choi, J.-Y.; Wu, J.; Lopez, A.; Chen, Z., Titanium nitride-carbon nanotube core-shell composites as effective electrocatalyst supports for low temperature fuel cells. *J. Mater. Chem.* **2012,** *22* (9), 3727-3732.

(215) Jaouen, F.; Proietti, E.; Lefevre, M.; Chenitz, R.; Dodelet, J.-P.; Wu, G.; Chung, H. T.; Johnston, C. M.; Zelenay, P., Recent advances in non-precious metal catalysis for oxygen-reduction reaction in polymer electrolyte fuel cells. *Energy Environ. Sci.* **2011,** *4* (1), 114-130.

(216) Harvey, C. J.; LeBouf, R. F.; Stefaniak, A. B., Formulation and stability of a novel artificial human sweat under conditions of storage and use. *Toxicol. in Vitro* **2010,** *24* (6), 1790-1796.

(217) Zhang, Z.; Wang, C.-C.; Zakaria, R.; Ying, J. Y., Role of Particle Size in Nanocrystalline TiO2-Based Photocatalysts. *The Journal of Physical Chemistry B* **1998,** *102* (52), 10871-10878.

(218) Nakagawa, Y.; Ikejiri, T., Electronic toothbrush and electronic brush. Google Patents: 2006.

(219) Kondo, M. M.; Jardim, W. F., Photodegradation of chloroform and urea using Ag-loaded titanium dioxide as catalyst. *Water Res.* **1991,** *25* (7), 823-827.

(220) Yamazoe, S.; Okumura, T.; Hitomi, Y.; Shishido, T.; Tanaka, T., Mechanism of Photo-Oxidation of NH3 over TiO2: Fourier Transform Infrared Study of the Intermediate Species. *The Journal of Physical Chemistry C* **2007,** *111* (29), 11077-11085.

(221) Bellardita, M.; Garcia-Lopez, E. I.; Marci, G.; Megna, B.; Pomilla, F. R.; Palmisano, L., Photocatalytic conversion of glucose in aqueous suspensions of heteropolyacid-TiO2 composites. *RSC Adv.* **2015,** *5* (73), 59037-59047.

(222) Zhou, B.; Song, J.; Zhou, H.; Wu, T.; Han, B., Using the hydrogen and oxygen in water directly for hydrogenation reactions and glucose oxidation by photocatalysis. *Chemical Science* **2016,** *7* (1), 463-468.

(223) Peter, L. M., Dynamic aspects of semiconductor photoelectrochemistry. *Chem. Rev.* **1990,** *90* (5), 753-769.

(224) Ahn, K.-S.; Yan, Y.; Lee, S.-H.; Deutsch, T.; Turner, J.; Tracy, C. E.; Perkins, C. L.; Al-Jassim, M., Photoelectrochemical Properties of N-Incorporated ZnO Films Deposited by Reactive RF Magnetron Sputtering. *J. Electrochem. Soc.* **2007,** *154* (9), B956-B959.

(225) Chen, H.; Liu, G.; Wang, L., Switched photocurrent direction in Au/TiO2 bilayer thin films. *Sci Rep-Uk* **2015,** *5*, 10852.

(226) Szacilowski, K.; Macyk, W.; Stochel, G., Synthesis, structure and photoelectrochemical properties of the TiO2-Prussian blue nanocomposite. *J. Mater. Chem.* **2006,** *16* (47), 4603-4611.

(227) Li, L.; Xue, S.; Chen, R.; Liao, Q.; Zhu, X.; Wang, Z.; He, X.; Feng, H.; Cheng, X., Performance characteristics of a membraneless solar responsive photocatalytic fuel cell with an

air-breathing cathode under different fuels and electrolytes and air conditions. *Electrochim. Acta* **2015,** *182*, 280-288.

(228) Iyatani, K.; Horiuchi, Y.; Moriyasu, M.; Fukumoto, S.; Cho, S.-H.; Takeuchi, M.; Matsuoka, M.; Anpo, M., Development of separate-type Pt-free photofuel cells based on visible-light responsive TiO2 photoanode. *J. Mater. Chem.* **2012,** *22* (21), 10460-10463.

(229) Seger, B.; Pedersen, T.; Laursen, A. B.; Vesborg, P. C.; Hansen, O.; Chorkendorff, I., Using TiO2 as a conductive protective layer for photocathodic H2 evolution. *J. Am. Chem. Soc.* **2013,** *135* (3), 1057-64.

(230) Wu, Z.; Zhao, G.; Zhang, Y.; Liu, J.; Zhang, Y.-n.; Shi, H., A solar-driven photocatalytic fuel cell with dual photoelectrode for simultaneous waste water treatment and hydrogen production. *J. Mater. Chem. A* **2015,** *3* (7), 3416-3424.

(231) Xie, X.; Ye, M.; Hsu, P.-C.; Liu, N.; Criddle, C. S.; Cui, Y., Microbial battery for efficient energy recovery. *Proceedings of the National Academy of Sciences* **2013,** *110* (40), 15925-15930.

(232) Larminie, J.; Dicks, A., Efficiency and Open Circuit Voltage. In *Fuel Cell Systems Explained*, John Wiley & Sons, Ltd,. 2013; pp 25-43.

(233) Murthy, M.; Electrolysis, E. S. I.; Division, E. E.; Division, E. S. E. T.; Division, E. S. B., *Proton Conducting Membrane Fuel Cells IV: Proceedings of the International Symposium*. Electrochemical Society: 2006.

(234) Kaneko, M.; Suzuki, S.; Ueno, H.; Nemoto, J.; Fujii, Y., Photoelectrochemical decomposition of bio-related compounds at a nanoporous semiconductor film photoanode and their photocurrent–photovoltage characteristics. *Electrochim. Acta* **2010,** *55* (9), 3068-3074.

(235) Hubenova, Y.; Mitov, M., Potential application of Candida melibiosica in biofuel cells. *Bioelectrochemistry* **2010,** *78* (1), 57-61.

(236) Davis, F.; Higson, S. P. J., Biofuel cells—Recent advances and applications. *Biosensors and Bioelectronics* **2007,** *22* (7), 1224-1235.

(237) Fernando, E.; Keshavarz, T.; Kyazze, G., Complete degradation of the azo dye Acid Orange-7 and bioelectricity generation in an integrated microbial fuel cell, aerobic two-stage bioreactor system in continuous flow mode at ambient temperature. *Bioresour. Technol.* **2014,** *156*, 155-162.

(238) Li, Z.; Zhang, X.; Lin, J.; Han, S.; Lei, L., Azo dye treatment with simultaneous electricity production in an anaerobic–aerobic sequential reactor and microbial fuel cell coupled system. *Bioresour. Technol.* **2010,** *101* (12), 4440-4445.

(239) Han, T. H.; Khan, M. M.; Kalathil, S.; Lee, J.; Cho, M. H., Simultaneous Enhancement of Methylene Blue Degradation and Power Generation in a Microbial Fuel Cell by Gold Nanoparticles. *Ind. Eng. Chem. Res.* **2013,** *52* (24), 8174-8181.

(240) Liu, H.; Ramnarayanan, R.; Logan, B. E., Production of Electricity during Waste water Treatment Using a Single Chamber Microbial Fuel Cell. *Environmental Science & Technology* **2004,** *38* (7), 2281-2285.

(241) Min, B.; Kim, J.; Oh, S.; Regan, J. M.; Logan, B. E., Electricity generation from swine waste water using microbial fuel cells. *Water Res.* **2005,** *39* (20), 4961-4968.

(242) Logan, B. E.; Hamelers, B.; Rozendal, R.; Schröder, U.; Keller, J.; Freguia, S.; Aelterman, P.; Verstraete, W.; Rabaey, K., Microbial Fuel Cells: Methodology and Technology. *Environmental Science & Technology* **2006,** *40* (17), 5181-5192.

(243) Li, W.-W.; Yu, H.-Q.; He, Z., Towards sustainable waste water treatment by using microbial fuel cells-centered technologies. *Energy Environ. Sci.* **2014,** *7* (3), 911-924.

(244) Min, B.; Logan, B. E., Continuous Electricity Generation from Domestic Waste water and Organic Substrates in a Flat Plate Microbial Fuel Cell. *Environmental Science & Technology* **2004,** *38* (21), 5809-5814.

(245) Sevda, S.; Dominguez-Benetton, X.; Vanbroekhoven, K.; De Wever, H.; Sreekrishnan, T. R.; Pant, D., High strength waste water treatment accompanied by power generation using air cathode microbial fuel cell. *Applied Energy* **2013,** *105*, 194-206.

(246) Huang, J.; Yang, P.; Guo, Y.; Zhang, K., Electricity generation during waste water treatment: An approach using an AFB-MFC for alcohol distillery waste water. *Desalination* **2011,** *276* (1), 373-378.

(247) Feng, Y.; Wang, X.; Logan, B. E.; Lee, H., Brewery waste water treatment using air-cathode microbial fuel cells. *Appl. Microbiol. Biotechnol.* **2008,** *78* (5), 873-880.

(248) Tamilarasan, K.; Banu, J. R.; Jayashree, C.; Yogalakshmi, K. N.; Gokulakrishnan, K., Effect of organic loading rate on electricity generating potential of upflow anaerobic microbial fuel cell treating surgical cotton industry waste water. *Journal of Environmental Chemical Engineering* **2017,** *5* (1), 1021-1026.

(249) Liu, Y.; Li, J.; Zhou, B.; Chen, H.; Wang, Z.; Cai, W., A TiO2-nanotube-array-based photocatalytic fuel cell using refractory organic compounds as substrates for electricity generation. *Chem Commun* **2011,** *47* (37), 10314-10316.

(250) Chen, Q.; Li, J.; Li, X.; Huang, K.; Zhou, B.; Cai, W.; Shangguan, W., Visible-Light Responsive Photocatalytic Fuel Cell Based on WO3/W Photoanode and Cu2O/Cu Photocathode

for Simultaneous Waste water Treatment and Electricity Generation. *Environmental Science & Technology* **2012,** *46* (20), 11451-11458.

(251) Lui, G.; Liao, J.-Y.; Duan, A.; Zhang, Z.; Fowler, M.; Yu, A., Graphene-wrapped hierarchical TiO2 nanoflower composites with enhanced photocatalytic performance. *J. Mater. Chem. A* **2013,** *1* (39), 12255-12262.

(252) Liao, J. Y.; Lei, B. X.; Kuang, D. B.; Su, C. Y., Tri-functional hierarchical TiO2 spheres consisting of anatase nanorods and nanoparticles for high efficiency dye-sensitized solar cells. *Energy Environ. Sci.* **2011,** *4* (10), 4079-4085.

(253) Capek, I., *Noble Metal Nanoparticles: Preparation, Composite Nanostructures, Biodecoration and Collective Properties*. Springer Japan: 2017.

(254) Hanaor, D. A. H.; Sorrell, C. C., Review of the anatase to rutile phase transformation. *J. Mater. Sci.* **2011,** *46* (4), 855-874.

(255) Zhang, F.; Cheng, Z.; Cui, L.; Duan, T.; Anan, A.; Zhang, C.; Kang, L., Controllable synthesis of Ag@TiO2 heterostructures with enhanced photocatalytic activities under UV and visible excitation. *RSC Adv.* **2016,** *6* (3), 1844-1850.

(256) Su, C.; Liu, L.; Zhang, M.; Zhang, Y.; Shao, C., Fabrication of Ag/TiO2 nanoheterostructures with visible light photocatalytic function via a solvothermal approach. *CrystEngComm* **2012,** *14* (11), 3989-3999.

(257) Lu, N.; Wang, Y.; Ning, S.; Zhao, W.; Qian, M.; Ma, Y.; Wang, J.; Fan, L.; Guan, J.; Yuan, X., Design of plasmonic Ag-TiO2/H3PW12O40 composite film with enhanced sunlight photocatalytic activity towards o-chlorophenol degradation. *Sci Rep-Uk* **2017,** *7* (1), 17298.

(258) Brus, L., Electronic wave functions in semiconductor clusters: experiment and theory. *The Journal of Physical Chemistry* **1986,** *90* (12), 2555-2560.

(259) Xue, X.; Ji, W.; Mao, Z.; Mao, H.; Wang, Y.; Wang, X.; Ruan, W.; Zhao, B.; Lombardi, J. R., Raman Investigation of Nanosized TiO2: Effect of Crystallite Size and Quantum Confinement. *The Journal of Physical Chemistry C* **2012,** *116* (15), 8792-8797.

(260) Zaban, A.; Greenshtein, M.; Bisquert, J., Determination of the Electron Lifetime in Nanocrystalline Dye Solar Cells by Open-Circuit Voltage Decay Measurements. *ChemPhysChem* **2003,** *4* (8), 859-864.

(261) Bisquert, J.; Zaban, A.; Greenshtein, M.; Mora-Seró, I., Determination of Rate Constants for Charge Transfer and the Distribution of Semiconductor and Electrolyte Electronic Energy Levels in Dye-Sensitized Solar Cells by Open-Circuit Photovoltage Decay Method. *J. Am. Chem. Soc.* **2004,** *126* (41), 13550-13559.

(262) Wen, Q.; Wu, Y.; Zhao, L.-x.; Sun, Q.; Kong, F.-y., Electricity generation and brewery waste water treatment from sequential anode-cathode microbial fuel cell. *Journal of Zhejiang University SCIENCE B* **2010,** *11* (2), 87-93.

(263) Yu, J.; Park, Y.; Kim, B.; Lee, T., Power densities and microbial communities of brewery waste water-fed microbial fuel cells according to the initial substrates. *Bioprocess Biosyst. Eng.* **2015,** *38* (1), 85-92.

(264) Mozia, S., Photocatalytic membrane reactors (PMRs) in water and waste water treatment. A review. *Sep. Purif. Technol.* **2010,** *73* (2), 71-91.

(265) Zhang, K.; Guo, L., Metal sulphide semiconductors for photocatalytic hydrogen production. *Catalysis Science & Technology* **2013,** *3* (7), 1672-1690.

(266) Wang, H.; Wang, B.; Bian, Y.; Dai, L., Enhancing Photocatalytic Activity of Graphitic Carbon Nitride by Codoping with P and C for Efficient Hydrogen Generation. *ACS Appl. Mater. Interfaces* **2017,** *9* (26), 21730-21737.

(267) Li, B.; Nie, Z.; Vijayakumar, M.; Li, G.; Liu, J.; Sprenkle, V.; Wang, W., Ambipolar zinc-polyiodide electrolyte for a high-energy density aqueous redox flow battery. *Nat Commun* **2015,** *6*, 6303.

(268) Yu, M.; McCulloch, W. D.; Beauchamp, D. R.; Huang, Z.; Ren, X.; Wu, Y., Aqueous Lithium–Iodine Solar Flow Battery for the Simultaneous Conversion and Storage of Solar Energy. *J. Am. Chem. Soc.* **2015,** *137* (26), 8332-8335.

Appendix A: Supporting Information for Chapter 4

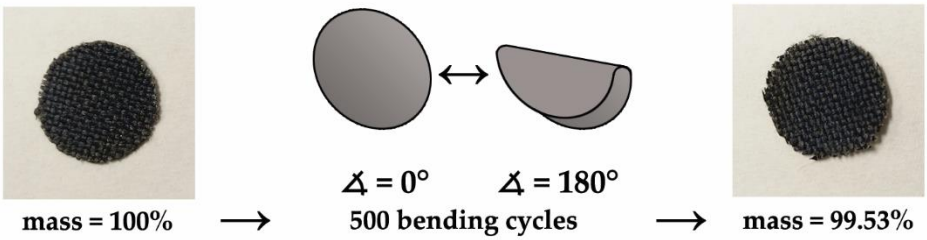

Figure A-1. Optical image and mass change of 3T-C-CC electrode after 500 bending cycles (r = 2 mm).

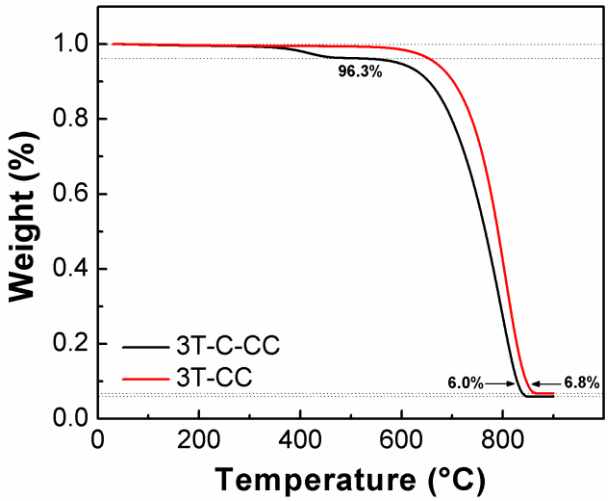

Figure A-2. Representative TGA curves of 3T-CC and 3T-C-CC used to determine the mass loading of TiO_2 in the carbon cloth electrodes.

Appendix B: Supporting Information for Chapter 5

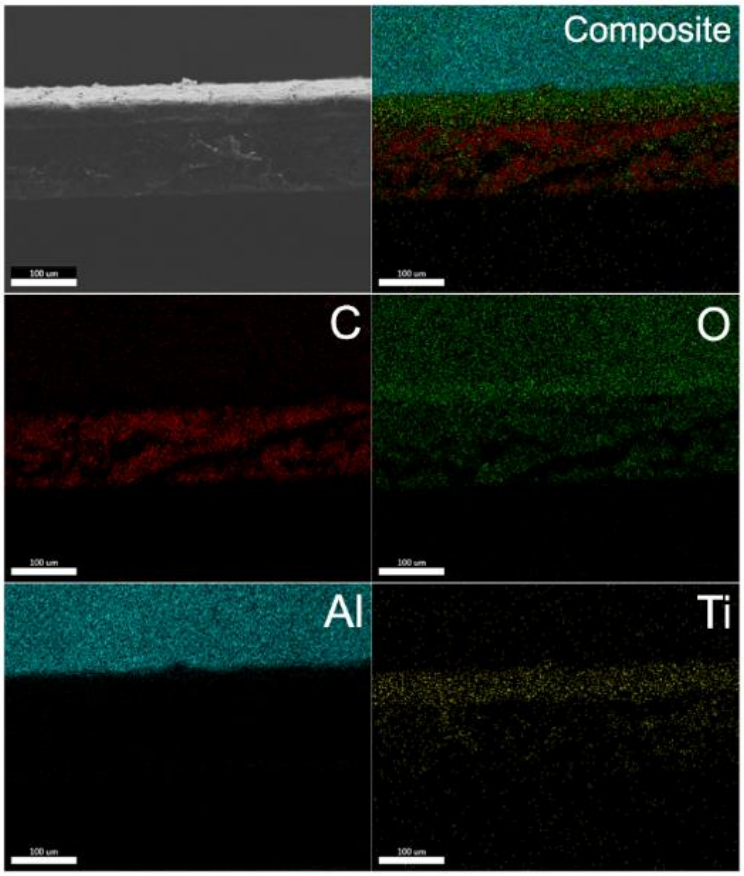

Figure B-1. SEM EDX map of photoanode electrode cross-section, showing results for C, O, Al, and Ti.The unique presence of Ti and C in the TiO_2 and PET layers, respectively, confirm the configuration of the photoanode.

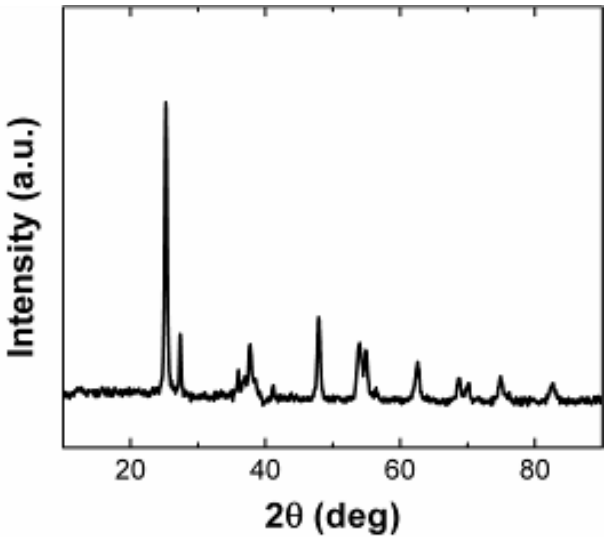

Figure B-2. XRD spectrum of TiO_2 electrode showing the characteristic anatase and rutile peaks of mixed-phase TiO_2.

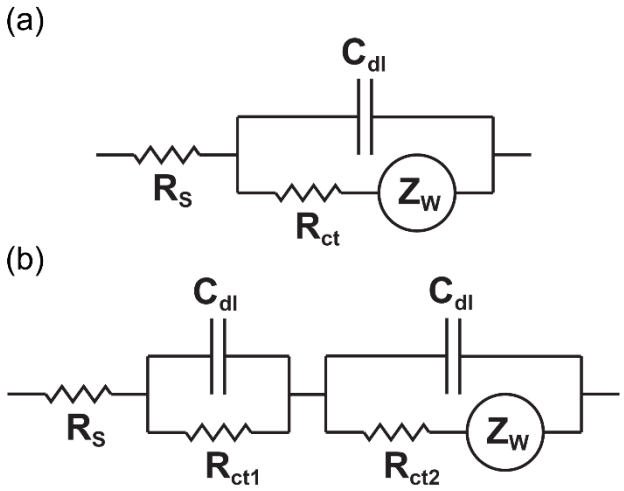

Figure B-3. Equivalent circuits used to model the flexible photocatalytic fuel cell EIS data(a) in the dark, and (b) under light irradiation.

Table B-1. Fitted values of EIS data modelled in ZSimpWin.

	Dark				**Light**					
	R_S	**R_{ct}**	**C_{dl}**	**Z_W**	**R_S**	**R_{ct1}**	**C**	**R_{ct2}**	**C**	**Z_W**
Flat	315.3	0.0164	5.15E-5	6.97E-5	257.2	26.5	1.87E-8	200.9	1.80E-4	2.09E-3
Bending	316.4	0.0487	6.61E-5	5.84E-5	189.5	0.175	2.96E-5	13.5	8.27E-7	6.04E-4

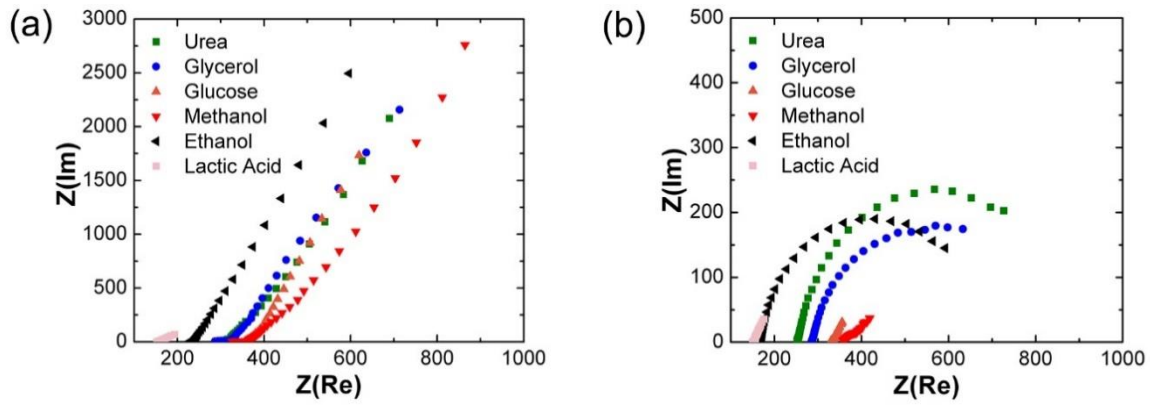

Figure B-4. EIS data flexible photocatalytic fuel cell using various fuels under (a) dark conditions and (b) light irradiation.

Appendix C: Supporting Information for Chapter 6

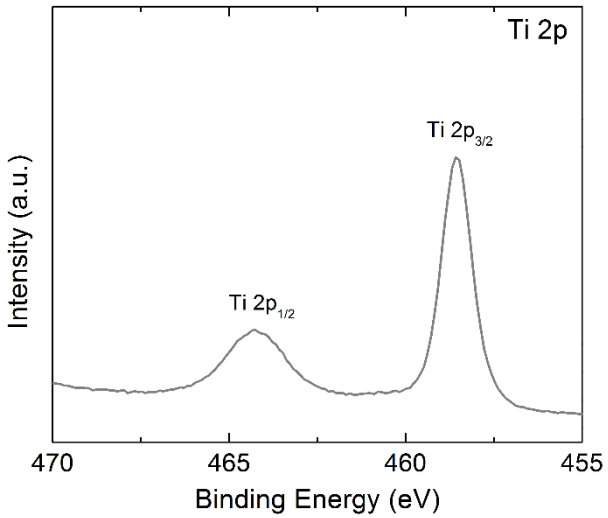

Figure C-1. XPS of pure TiO_2 synthesized without Ag. The Ti 2p spectrum shows typical $2p_{3/2}$ and $2p_{1/2}$ peaks at 458.58 eV and 464.28 eV.

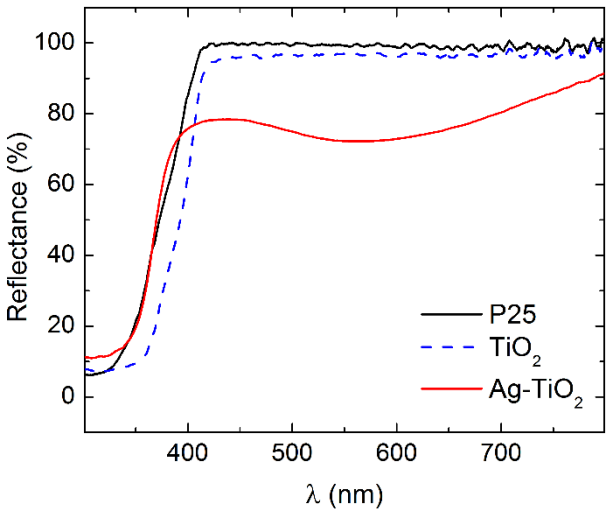

Figure C-2. Diffuse reflectance spectroscopy data for P25, TiO_2, and Ag-TiO_2, comparing reflectance properties.

Table C-1: Representative XPS data giving the composition of Ag-TiO_2.Stoichiometric amounts of Ti and O are consistent with TiO_2 and XRD data.

Name	Peak BE (eV)	FWHM eV	Area CPS eV	at%
Ti 2p	459.48	0.97	100276.46	33.73
O 1s	530.70	1.16	82325.25	65.68
Ag 3d	368.75	1.33	6455.66	0.59

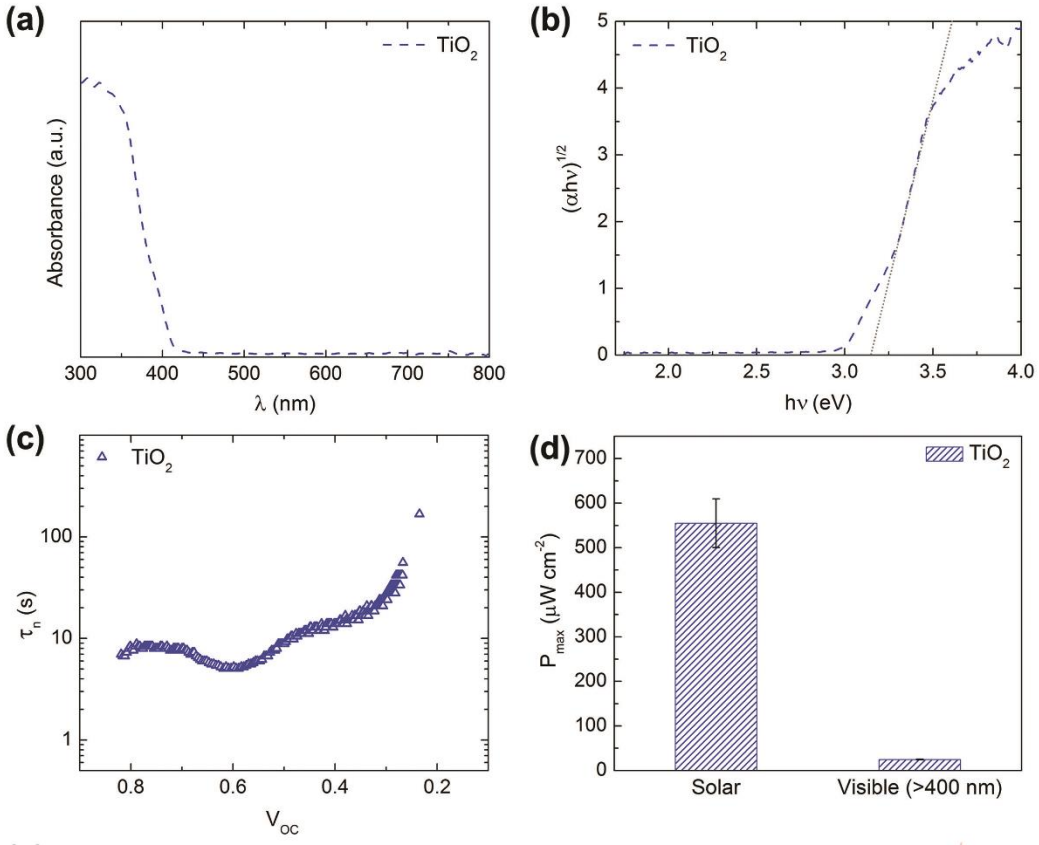

Figure C-3. Diffuse reflectance spectroscopy data for TiO_2, including (a) absorbance and (b) the calculated Tauc plot. (c) electron lifetime measurements for TiO_2, and (d) P_{max} comparison of TiO_2 under solar and visible (<400 nm) light.

Appendix D: Research Contributions

Publications (Refereed Journals)

(1) **Lui, G.**; Jiang, G.; Lenos, J.; Lin, E.; Fowler, M.; Yu, A.; Chen, Z., Advanced Biowaste-Based Flexible Photocatalytic Fuel Cell as a Green Wearable Power Generator. *Advanced Materials Technologies* **2017,** *2* (3).

(2) **Lui, G.**; Li, G.; Wang, X.; Jiang, G.; Lin, E.; Fowler, M.; Yu, A.; Chen, Z., Flexible, three-dimensional ordered macroporous TiO_2 electrode with enhanced electrode–electrolyte interaction in high-power Li-ion batteries. *Nano Energy* **2016,** *24*, 72-77.

(3) **Lui, G.**; Jiang, G.; Duan, A.; Broughton, J.; Zhang, J.; Fowler, M. W.; Yu, A., Synthesis and Characterization of Template-Free VS_4 Nanostructured Materials with Potential Application in Photocatalysis. *Ind. Eng. Chem. Res.* **2015,** *54* (10), 2682-2689.

(4) **Lui, G.**; Liao, J.-Y.; Duan, A.; Zhang, Z.; Fowler, M.; Yu, A., Graphene-wrapped hierarchical TiO_2 nanoflower composites with enhanced photocatalytic performance. *J. Mater. Chem. A* **2013,** *1* (39), 12255-12262.

Prepared & Submitted for Publication

(5) **Lui, G.**; Jiang, G.; Fowler, M.; Yu, A.; Chen, Z., A High Performance Waste water-Fed Flow-Photocatalytic Fuel Cell. (submitted to *Journal of Power Sources*).

Conference Presentations

(6) **Lui, G.**; Jiang, G.; Fowler, M.; Yu, A.; Chen, Z., Ag@TiO_2 NF As a Visible Light Photoanode in Photocatalytic Fuel Cells. Presented at the Electrochemical Society, 232nd Meeting, 2017, National Harbor, MD, United States

(7) **Lui, G.**; Jiang, G.; Lenos, J.; Lin, E.; Fowler, M.; Yu, A.; Chen, Z., Advanced Biowaste-Based Flexible Photocatalytic Fuel Cell as a Green Wearable Power Generator. Presented at Materials Research Society, Fall Meeting, 2016, Boston, MA, United States

(8) **Lui, G.**; Li, G.; Wang, X.; Jiang, G.; Lin, E.; Fowler, M.; Yu, A.; Chen, Z., Flexible, three-dimensional ordered macroporous TiO_2 electrode with enhanced electrode–electrolyte interaction in high-power Li-ion batteries. Presented at Materials Research Society, Fall Meeting, 2016, Boston, MA, United States

(9) **Lui, G.**; Jiang, G.; Duan, A.; Broughton, J.; Zhang, J.; Fowler, M. W.; Yu, A., Synthesis and Characterization of Template-Free VS_4 Nanostructured Materials with Potential Application in Photocatalysis. Presented at CSChE 64th Meeting, 2014, Niagara Falls, Canada

(10) **Lui, G.**; Liao, J.-Y.; Duan, A.; Zhang, Z.; Fowler, M.; Yu, A., Graphene-wrapped hierarchical TiO_2 nanoflower composites with enhanced photocatalytic performance. Presented at The Electrochemical Society, 223rd Meeting, 2013, Toronto, Canada